UNIVERSITY OF SOUTHAMPTON

Faculty of Engineering and Physical Sciences
Optoelectronics Research Centre

Multi-mode Hollow-core Anti-resonant Optical Fibres

by

William Henry Warren Shere

MEng

ORCiD: 0000-0001-5159-7132

A thesis for the degree of
Doctor of Philosophy

February 2023

University of Southampton

Abstract

Faculty of Engineering and Physical Sciences
Optoelectronics Research Centre

Doctor of Philosophy

Multi-mode Hollow-core Anti-resonant Optical Fibres

by William Henry Warren Shere

The demonstration, during the course of this doctoral project, of an effectively single-mode hollow-core anti-resonant optical fibre with loss rivaling that of single-mode silica fibre represents a huge milestone in the development of hollow-core fibre technology that has the potential to transform the field of fibre optics and its many applications. As attention increasingly turns to a focus on deploying hollow-core fibre in real world applications, one largely unexplored topic is that of multi-mode hollow-core anti-resonant optical fibres. Unlike in solid-core fibre where multiple modes can be guided with virtually the same attenuation, multi-mode guidance in hollow-core fibres presents a unique challenge in the form of large differential loss - and in general optical properties - between modes. Nevertheless multi-mode guidance in a hollow core presents opportunities in many application areas, including high-power laser delivery, short-haul telecommunication systems and light-gas interaction systems, whilst offering lower loss, nonlinearity and latency across larger bandwidths than solid-core fibres.

This thesis presents research concerning the nature of multi-mode guidance in anti-resonant optical fibres, their characteristics and their design for practical applications. Numerical simulation is applied extensively to study in detail the origins of the differential modal properties of these fibres, including attenuation and dispersion, leading to a new understanding of the processes involved. This facilitated the development of methods to engineer the differential properties of the anti-resonant fibres in order to achieve multi-mode guidance in fibres with a variety of micro-structure designs. Methods based on structural design and deployment conditions are explored. Design techniques are presented for multi-mode anti-resonant fibres targeting specific requirements in several application areas: short-haul telecommunications, delivery of high-power laser light and finally, fibre based gas sensors.

Contents

Nomenclature

ALIF	Anti-resonant leakage inhibited fibre
ARF	Anti-resonant fibre
ARROW	Anti-resonant reflective optical waveguide
CW	Continuous wave
DGD	Differential group delay
DNANF	Double-nested anti-resonant nodeless fibre
FEM	Finite element method
GI	Graded index
GVD	Group velocity dispersion
HOM	Higher-order mode
IC	Inner cladding
LP	Linearly polarised
NANF	Nested-element anti-resonant nodeless fibre
OC	Outer cladding
OM	Optical multi-mode (standards)
ORC	Optoelectronics Research Centre
PBGF	Photonic-bandgap fibre
PML	Perfectly matched layer
SSL	Surface scattering loss
TE	Transverse electric
TIR	Total internal reflection

TM	Hybrid electric
TM	Transverse magnetic
VCSEL	Vertical cavity surface emitting laser

List of Figures

Declaration of Authorship

I declare that this thesis and the work presented in it is my own and has been generated by me as the result of my own original research.

I confirm that:

1. This work was done wholly or mainly while in candidature for a research degree at this University;
2. Where any part of this thesis has previously been submitted for a degree or any other qualification at this University or any other institution, this has been clearly stated;
3. Where I have consulted the published work of others, this is always clearly attributed;
4. Where I have quoted from the work of others, the source is always given. With the exception of such quotations, this thesis is entirely my own work;
5. I have acknowledged all main sources of help;
6. Where the thesis is based on work done by myself jointly with others, I have made clear exactly what was done by others and what I have contributed myself;
7. Parts of this work have been published as described in the List of Publications at the end of this thesis.

Signed:..... Date:.....

Acknowledgements

There are a number of people I must thank for their unwavering support whilst completing this PhD. I must first say thank you to my supervisors: Francesco Poletti, Eric Numkam-Fokoua and Gregory Jasion. Thank you for your wisdom when I was slipping, your patience when I was slow, your guidance when I was spinning and your kindness when I needed it. I am truly grateful and it shall not be forgotten.

My friends are a group without whom I feel I would have achieved nothing at all. To them all, thank you for your hugs in what have been some very dark days and your laughter in what has been some of the very best of days. You have kept me sane. A special mention to my friend Kaustubh Jalundhwala; you may not have kept me sane but you certainly kept me busy. The past years have been bearable with you beside me. To the greatest times gone by and the greatest yet to come.

A final mention to my parents who are always there for me. Thank you for being a rock, for all the support and for all your advice even if I don't always take it.

Chapter 1

Introduction

Fibre optics has fundamentally altered our technological relationship with light, providing the ability to guide light in flexible optical fibres, and has now become ubiquitous in many technological areas. Laser light can be delivered in flexible fibres over metre distances for medical and surgical applications or high-power machining. Unparalleled precision sensors can be implemented based on fibre inferometry and multi-kilometre long distributed sensors can be created in optical fibre. The widest deployment of optical fibre however, and where their impact has been felt most strongly, is in telecommunications. This is also perhaps the application area where it is easiest to chart the revolutionary rise of fibre optics in modern technology. It also indicates the point, soon to be reached and arguably already present, where current state-of-the-art solid-core silica fibres can rise no further.

The first transatlantic optical fibre communication system, "TAT-8", was deployed in 1988 and connected Lands End, United Kingdom, Penmarch, France and Tuckerton, United States with a capacity of approximately 560 Mbit/s [1]. Today, in 2022, networks consisting of 1000s of kilometres of optical fibre in globe-spanning terrestrial and undersea cables form the backbone of the internet and a single optical fibre can transmit more than 10 Tbit/s over 10000 km [2]. This revolutionary advancement of fibre optic technology was spurred by the observation of Kao and Hockham in 1966 that silica optical fibre could become a viable telecommunications platform if material impurities could be reduced to bring optical losses below 20 dB/km [3]. This threshold was reached and then surpassed, and in a little over a decade solid-core silica fibres with losses of 0.2 dB/km at a wavelength of 1550 nm were demonstrated [4, 5]. However, any significant improvement of solid-core silica fibres is unlikely beyond this point as the optical performance in these fibres is fundamentally limited by the intrinsic properties of the silica material itself. Chief among them are: attenuation, driven by the fundamental Rayleigh scattering limit at short wavelengths below 1.3 µm and intrinsic material absorption beyond 1.6 µm; nonlinearity; and dispersion [6–8]. Current systems are almost within a factor 2x of achieving the

theoretical maximum capacity offered by solid-core fibre [6, 9]. It is believed that a fundamentally different class of optical fibre, not governed by the intrinsic material limitations of solid-core silica, will be required to enable a continued growth of the capabilities and capacity of fibre optic technology.

The advent of hollow-core fibres is arguably the most exciting development in optical fibre technology for the past twenty years. Hollow-core fibres which confine light by anti-resonant guidance exhibit ultra-low nonlinearity, latency and dispersion owing to guiding more than 99.99% of light in air and have the potential for attenuation lower than solid-core fibres over larger bandwidths [10, 11]. The unique guidance properties of hollow-core anti-resonant fibre (ARF) promises a solution to the data capacity demand in decades to come [12] and suggests the potential for enhancement of current applications and development of novel technologies [13–17]. So far, ARF technology has sought to emulate only the dominant solid-core platform which is based on the standard single mode fibre, but opportunities and a huge untapped potential lies in multi-mode hollow-core fibres, an investigation of which is the main topic of this thesis.

1.1 Motivation

The idea of guiding light in hollow-core optical fibres is as old as the field of fibre optics itself [18]. Air guidance is attractive for the ability to avoid the dispersion, nonlinear response, latency and material absorption incurred by propagating light in optical materials. Hollow-core fibres therefore combine the best features of air-guidance with the benefits of optical fibre, namely flexible and reliable guidance. It was not until the advent of fibre with micro-structured cladding, first demonstrated practically in 1999 [19], that the optical loss in hollow-core fibres was reduced to the level of dB/m, the minimum acceptable for most applications. Since the first hollow-core fibres, research progressed at a blistering pace and, in addition to making use of their novel properties in a range of applications [16], just 5 years later a hollow-core fibre was fabricated with losses of just 1.7 dB/km [20]. These early hollow-core fibres were based on photonic-bandgap guidance (PBGF) but more recently anti-resonant fibres were suggested. ARFs were initially thought necessarily to have higher losses, but in 2014 Poletti showed theoretically that by careful design of the micro-structure cladding, losses could be be reduced not just below PBGFs but in principle also to lower values than the minimum loss of solid-core silica fibre [10].

Once again, research progressed at a phenomenal pace. Figure 1.1 shows the reported minimum loss values since 2015 for fabricated single-mode hollow-core fibres based on anti-resonant guidance. In less than a decade ARFs, and in particular the nested-element anti-resonant nodeless fibre (NANF), have gone from a purely

numerical concept to realised fibres with sub-0.5 dB/km losses across the telecommunication wavelengths [21]. Finally, in 2022 the slightly modified double-nested anti-resonant nodeless fibre (DNANF) was fabricated for the first time with measured loss of just 0.174 dB/km, equal to the minimum loss recorded in single-mode solid-core fibre [22, 23]. In parallel with these efforts, single-mode ARFs have been investigated for practical applications which included telecommunication demonstrations [24, 25] and theoretical analysis suggests that existing NANFs are capable of between 2x and 5x the data bandwidth of current long-haul telecommunication solid-core fibres [12]. In high-power laser fibre delivery a NANF has been demonstrated delivering 1 kW continuous power over 1 km, an order of magnitude greater than state of the art in solid-core fibres [26]. Meanwhile, a strong understanding of the fabrication process has been developed [11, 27–29]; 100s of kilometres of single-mode NANF have been fabricated in the lab and commercial NANF cables are currently available [30].

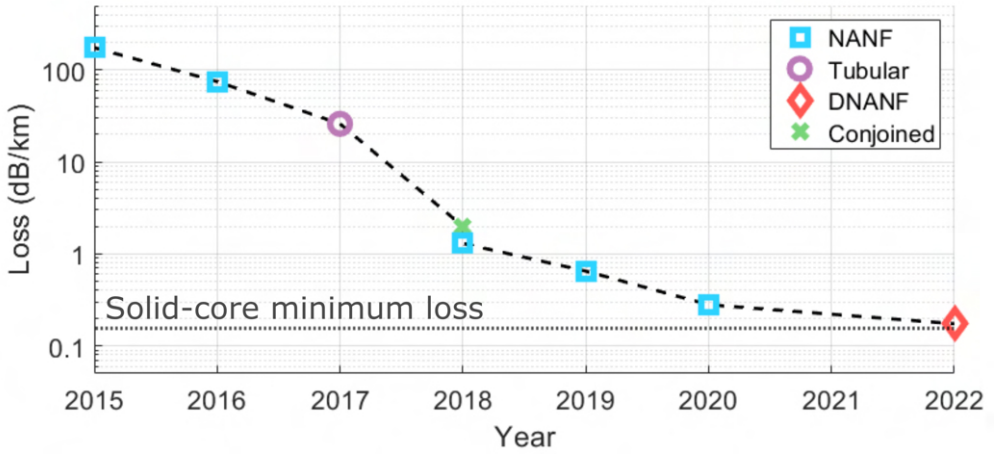

FIGURE 1.1: Reported minimum loss values for fabricated hollow-core anti-resonant fibre between 2015-2022 [21, 22, 31–36] compared to the minimum reported loss in solid-core fibre [23]. Loss is measured at the telecommunications wavelength, 1550 nm, in post-2018 fibres. Minimum loss values for pre-2018 fibre were recorded at shorter and longer wavelengths in the near-infrared and visible.

With phenomenal accomplishments demonstrated in the design and fabrication of single-mode ARFs, attention is increasingly turning to applications that can exploit their potential. In this thesis, a different class of ARFs are investigated, specifically those that guide multiple optical modes.

1.1.1 Why Multi-mode

Research into hollow-core anti-resonant fibre has so far largely focused on achieving low-loss, single-mode guidance. This is representative of the fact that many fibre optic applications strongly benefit from the modal purity of single-mode guidance, including long-haul telecommunications. A great many applications, however, benefit

or even require multi-mode guidance in areas as diverse as short-haul telecommunications, power delivery and gas sensing [37–40]. When using multi-mode lasers as sources, multi-mode fibres are necessary for high coupling efficiency and even single-mode sources benefit from reduced alignment and focusing tolerances with multi-mode fibres. The topic of multi-mode nonlinear optics has attracted significant interest in recent years; enhanced non-linear effects in multi-mode fibres can be exploited for spectral engineering or soliton formation in ARFs by filling the hollow-core with particular gasses that exhibit desirable nonlinear effects [40–45]. In sensing, the most sensitive hollow-core fibre sensors based on light-gas interaction employ inter-modal interferometry in few-mode fibre [46, 47] whilst novel distributed sensors based on inter-modal coupling have been suggested [48].

Despite the myriad of applications, both novel and existing, that are suggested by multi-mode guidance in ARFs, there has been very little research into this topic with only a few examples of fabricated few-mode ARF and very little theoretical investigation reported in literature [48–50]. In this thesis the principles of multi-mode guidance in ARF are investigated, techniques for designing low-loss few- and multi-mode ARFs are devised and the practical considerations for several real-world applications are considered.

1.2 Thesis Outline

A background of the topic is presented in Chapter 2. The chapter begins with a broad introduction to the physics of fibre optics, describing the fundamental equations and properties of optical modes that are of crucial importance for understanding the behaviour of optical fibres. This is followed with a brief history and description of the fundamentals of of hollow-core anti-resonant fibre and their unique guidance properties. An introduction to the finite element method, the numerical technique used to simulate ARF in this thesis, is given next.

Chapter 3 is concerned with investigating the sources of differential leakage losses between the modes of multi-mode ARF. By considering the transverse power flow in tubular ARF structures based on a single ring of non-touching capillaries, the geometric cladding features that are associated with leakage loss are identified. An analysis of loss is conducted based on considering the strength of coupling to cladding modes guided within these geometric features. This is used to identify the existence of phase-mismatch windows, a useful concept for designing multi-mode ARF. A model for leakage loss, based on coupling to cladding modes, is shown to give good agreement to numerically simulated fibres. A comparison with NANFs suggest that this model would be applicable to these structures also.

Chapter 4 investigates the challenge of designing low-loss, few-moded ARF with a fixed core size that would be compatible with current short-haul multi-mode telecommunication standards. The limit of NANFs for multi-mode guidance with such a core is identified including when the fibres are deployed under bend. Using the concept of phase mismatch windows, described in Chapter 3, a technique is devised for designing the cladding for NANFs to maximise multi-mode guidance. It is discussed how this technique applies to double-nested nodeless anti-resonant nodeless fibres (DNANFs). Further geometries with additional adjacent nested elements are considered and the anti-resonant leakage inhibited fibre (ALIF) is identified as a promising candidate for short-haul telecommunications. A method for approximating the cladding modes of this structure, crucial for designing ARF, is described. Using this method an ALIF is designed that guided 7 mode-groups with lower loss than the solid-core multi-mode short-haul standard. This fibre design is investigated further for the purposes of short-haul telecommunications and differential modal delay is identified as a limiting factor in this application.

Chapter 5 focuses on three potential application spaces for few- and multi-mode ARFs. Following on from Chapter 4 the dispersion of multi-mode ARF is studied with a particular focus on differential modal delay, which would limit the achievable data rate in a single wavelength channel and significantly impact MDM-based links. Two potential methods of reducing inter-modal dispersion are investigated. Enforcing a constant bend is shown to be capable of significant reductions in inter-modal dispersion, however, the additional losses incurred and practicality of an enforced bend made it an unfeasible technique. Built-in twisting of the fibre is also investigated but is found ineffective for reducing inter-modal dispersion. Next, the applicability of ARFs for delivering high-power, multi-mode lasers is considered. The required modality of an ARF for efficient coupling to lasers of a given beam quality is determined. A technique is presented for designing NANFs to capture light from lasers with power in excess of 10 kW. Two such fibres are designed and their optical loss, damage threshold and dispersion is discussed for the given application. Finally, a novel approach to improving the sensitivity of fibre gas sensors based on spontaneous Raman scattering is discussed. Theoretical analysis suggests that by employing few-mode ARFs signal power can be more than doubled.

Finally, Chapter 6 summarises the conclusions from the work described in this thesis and suggests direction for further investigations on the topics covered within.

Chapter 2

Background

This chapter describes the fundamental principles of optical fibres, hollow-core technology and the modelling techniques employed in this work.

2.1 Optical fibre physics

An optical fibre is a type of electromagnetic waveguide capable of confining and guiding light. Optical fibres are flexible, made from glass or plastic with a circular cross section, a diameter less than a millimetre and are used in lengths anywhere from tens of centimetres to hundreds of kilometres. The waveguide may be given a polymer coating for protection. There is a wide variety of optical fibre designs but analysis of the simplest case, step-index fibre, can provide a great deal of insight into fibre in general.

2.1.1 Electromagnetic waveguides

The behaviour of a light as an electromagnetic wave can be understood by considering Maxwell's equations [51]. These are a set of coupled equations that describe the behaviour and interactions of electric and magnetic fields and underpin much of the technology of the modern world. Written in differential form these are:

$$\nabla \cdot \mathbf{D} = \rho \tag{2.1}$$

$$\nabla \cdot \mathbf{B} = 0 \tag{2.2}$$

$$\nabla \times \mathbf{E} = -\frac{\partial \mathbf{B}}{\partial t} \tag{2.3}$$

$$\nabla \times \mathbf{H} = \mathbf{J} + \frac{\partial \mathbf{D}}{\partial t} \tag{2.4}$$

with electric displacement field $\mathbf{D}$, electrical charge density ρ, magnetic flux density $\mathbf{B}$, electric field $\mathbf{E}$, magnetic field $\mathbf{H}$ and electrical current density $\mathbf{J}$. In this thesis **bold** typeface is used to distinguish vector values. For the dielectric materials discussed in this thesis there is no charge or current, hence $\rho = 0$ and $\mathbf{J} = 0$. The constitutive relations between flux density and field strength for electric and magnetic fields are:

$$\mathbf{D} = \epsilon \mathbf{E} = \epsilon_0 \epsilon_r \mathbf{E} \quad \text{and} \quad \mathbf{B} = \mu \mathbf{H} = \mu_0 \mu_r \mathbf{H} \tag{2.5}$$

where ϵ_0 is the electric permittivity of free space, μ_0 the magnetic permeability of free space and ϵ_r and μ_r are the relative permittivity and permeability. ϵ_0 and μ_0 are fundamental constants which Maxwell showed are related to the speed of light in a vacuum by $c_0 = \frac{1}{\sqrt{\epsilon_0 \mu_0}}$. The relative permittivity and permeability meanwhile characterise the optical properties of a medium, for example the wave impedance, $Z = \sqrt{\frac{\mu_0 \mu_r}{\epsilon_0 \epsilon_r}}$, and refractive index, $n = \sqrt{\epsilon_r \mu_r}$. The optical properties of a material are generally dependent on the optical frequency. Whilst omitted for simplicity in Eq. (2.5) this dependency implies that those equations are defined in the frequency domain. Transforming these relations into the time domain would result in a convolution integral.

In this thesis, of interest are materials which are isotropic, for which ϵ_r and μ_r are scalar quantities, and non-magnetic for which $\mu_r = 1$. The refractive index of such a material can be defined as: $n(\lambda) = \sqrt{\epsilon_r}$, where the dependence on the optical wavelength, λ, is made explicit. The approximate refractive index of pure, fused silica and air at wavelength $\lambda = 1550\,\text{nm}$ is 1.4440 and 1.0003 respectively [52]. At this wavelength both materials are transparent and n is purely real. In this regime a powerful model for the wavelength dependence of refractive index is the Sellmeier equation: $n^2(\lambda) = 1 + \sum_i B_i \lambda^2 / (\lambda^2 - C_i^2)$ [53]. Each term in the summation describes the empirically determined strength, B_i, of an absorption resonance at wavelength C_i. For characterising the refractive index of optical glasses a three term expression is common. The refractive index of fused silica glass is well described by [54]:

$$n(\lambda) = \sqrt{1 + \frac{0.6961663\lambda^2}{\lambda^2 - 0.0684043^2} + \frac{0.4079426\lambda^2}{\lambda^2 - 0.1162414^2} + \frac{0.8974794\lambda^2}{\lambda^2 - 9.896161^2}} \tag{2.6}$$

in the visible and near-infrared. Equation (2.6) is used to determine the refractive index of silica in numerical simulations throughout Chapters 3-5.

The wave equation, for electromagnetic waves in a charge and current free medium, is derived by taking the curl of Eq. (2.3) and Eq. (2.4), then substituting the constitutive relations Eq. (2.5) and simplifying:

$$\left(\nabla^2 - \mu\epsilon\frac{\partial^2}{\partial t^2}\right)\mathbf{E}(x,y,z,t) = 0 \quad \text{and} \quad \left(\nabla^2 - \mu\epsilon\frac{\partial^2}{\partial t^2}\right)\mathbf{H}(x,y,z,t) = 0 \tag{2.7}$$

where the electric and magnetic fields are generally 4-dimensional vector fields. Intuitively the solutions to Eq. (2.7) for a monochromatic field oscillate in time at the optical frequency, $f = c_0/\lambda$ and it is both convenient and common to extract this component of the solution. When expressed using a complex exponential, the time-harmonic term is $\exp(-i\omega t)$ where i is the complex unit satisfying $i = \sqrt{-1}$ and $\omega = 2\pi f$ is the angular frequency. In this format the electric and magnetic fields can be expressed in the time-invariant phasor format and Eq. (2.7) reduces to the Helmholtz equation:

$$\left(\nabla^2 + k_0^2 n^2\right)\mathbf{E}(x,y,z) = 0 \quad \text{and} \quad \left(\nabla^2 + k_0^2 n^2\right)\mathbf{H}(x,y,z) = 0 \tag{2.8}$$

where $k_0 = \omega/c_0$ is the freespace wavenumber. Solving Eq. (2.8) for a waveguide will describe how light propagates in that waveguide. In the following section the analytical solution for a simple optical fibre is discussed. For a structure that is longitudinally invariant the problem is reduced to that of a 2-dimensional cross-section of the waveguide, $n(x,y)$. Analytical solutions are of great interest for the insight which they can provide, however, in general Eq. (2.8) is not possible to solve analytically. The numerical approaches used in this thesis are described in Section 2.3.

2.1.2 Step-index optical fibre

Step-index fibre is used extensively for long distance telecommunication and as such is the most common and widely deployed. A conventional step index fibre is also the simplest to analyse and understand. The cross section of a step-index fibre is shown in Fig. 2.1. It consists of a high refractive index core of radius R and index n_{core} surrounded by a lower refractive index cladding and index $n_{cladding}$. By convention x and y are the transverse directions and z is the longitudinal direction in which light propagates. The core radius of the popular SMF-28 fibre is 8.2 µm and the outer diameter is 125 µm. At 1550 nm step-index fibres have losses as low as 0.15 dB/km [23].

Some insight into the optical behaviour of step-index fibre can be gained by applying a ray optics approach. Snell's law describes how light in the core hitting the cladding boundary at a slight, grazing angle will be totally internally refracted and remain confined to the core. Hence the method of guidance in this fibre is total internal

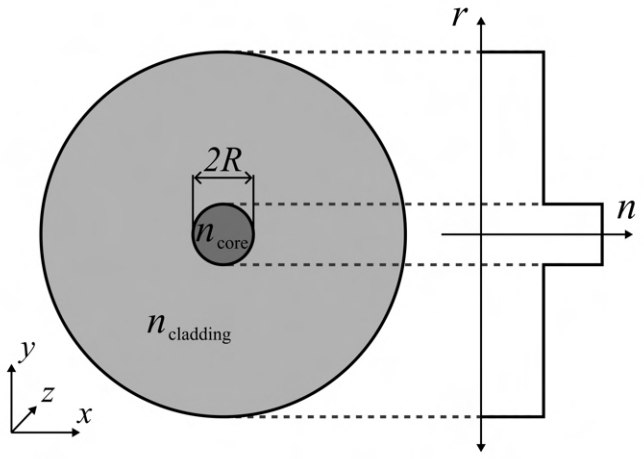

FIGURE 2.1: Cross section of a step-index optical fibre overlaid with the refractive index profile.

reflection (TIR). For a deeper understanding of the the fibre's behaviour however, a wave optics approach must be employed.

For simplicity the cladding can be considered infinite since solutions of interest are exponentially decaying in the cladding and in practice a higher index coating ensures that there is negligible reflection at the cladding/coating interface. Taking advantage of the circular symmetry of the fibre Eq. (2.8) can be written in polar coordinates $\{\rho, \theta, z\}$:

$$\left(\frac{\partial^2}{\partial\rho^2} + \frac{1}{\rho}\frac{\partial}{\partial\rho} + \frac{1}{\rho^2}\frac{\partial^2}{\partial\theta^2} + \frac{\partial^2}{\partial z^2} + n^2k_0^2\right)\mathbf{E} = 0 \tag{2.9}$$

and similarly for the magnetic field, $\mathbf{H}$. The electric and magnetic fields are both vector fields and in total there are 6 scalar components, but only two of these components are independent. Here the longitudinal electric field, E_z, will be determined and an identical technique can be applied to the longitudinal magnetic field, H_z. The solution to Eq. (2.9) can be written in separable form $E_z = F(\rho)\Theta(\theta)Z(z)$ and thereby solved by separation of variables. This results in three ordinary differential equations:

$$\left(\frac{\mathrm{d}^2}{\mathrm{d}z^2} + \beta^2\right)Z(z) = 0 \tag{2.10}$$

$$\left(\frac{\mathrm{d}^2}{\mathrm{d}\theta^2} + l^2\right)\Theta(\theta) = 0 \tag{2.11}$$

$$\left(\frac{\mathrm{d}^2}{\mathrm{d}\rho^2} + \frac{1}{\rho}\frac{\mathrm{d}}{\mathrm{d}\rho} + n^2k_0^2 - \beta^2 - \frac{l^2}{\rho^2}\right)F(\rho) = 0 \tag{2.12}$$

having introduced the propagation constant, β, and the azimuthal order, l. The physical significance of these quantities becomes apparent if we substitute the general solutions for Eq. (2.10), $Z(z) = \exp(-i\beta z)$, and Eq. (2.11), $\Theta(\theta) = \exp(-il\theta)$ into our separable definition for E_z. For clarity the previously omitted time dependence has been included:

$$E_z(\rho, \theta, z, t) = F_l(\rho) \exp(-il\theta) \exp(-i\omega t) \exp(-i\beta z) \tag{2.13}$$

From Eq. (2.13) it is clear that l must take only integer values as E_z must be 2π periodic in θ. The azimuthal index, l, defines the number of cycles of phase in one round trip in the azimuthal direction. Note l is included as a subscript of F since from Eq. (2.12) the radial field dependence clearly also depends on the azimuthal order. The phase constant β describes how the phase varies in the propagation direction, z, for a given wavelength. Often more convenient, however, is the effective index, $n_{eff} = \frac{\beta}{k_0} = \beta\frac{\lambda}{2\pi}$. It is the effective refractive index for light propagating in the waveguide according to a particular solution.

Equation (2.12) is a well known differential equation, the solutions to which are the Bessel functions. For a guided solution the field must be finite in the core and exponentially decaying in the cladding. The solution must therefore take the form of a Bessel function of the first kind, J, in the core and in the cladding a modified Bessel function of the second kind, K.

$$E_z(r, \theta, z) = \begin{cases} C_1 J_l(\kappa_1 \rho) \exp(-il\theta) \exp(-i\omega t) \exp(-i\beta z) & \text{for} \quad \rho \leq R \\ C_2 K_l(\kappa_2 \rho) \exp(-il\theta) \exp(-i\omega t) \exp(-i\beta z) & \text{for} \quad \rho > R \end{cases} \tag{2.14}$$

where $\kappa_1 = \sqrt{k_0^2 n_{core}^2 - \beta^2}$ and $\kappa_2 = \sqrt{\beta^2 - k_0^2 n_{clad}^2}$ are the transverse phase constants in the core and cladding regions and C_1 and C_2 are constants to be determined from the boundary conditions. A similar equation can be determined for H_z with two additional constants. Using Maxwell's equations the transverse field components can be derived in terms of E_z, H_z. The 4 constants can be determined by utilising the fact that the tangential field components, E_z, E_θ, H_z, H_θ, must be continuous at the core-cladding interface, $\rho = R$, which leads to the characteristic equation:

$$\left(\frac{J_l'(\kappa_1 R)}{\kappa_1 J_l(\kappa_1 R)} + \frac{K_l'(\kappa_2 R)}{\kappa_2 K_l(\kappa_2 R)}\right)\left(\frac{n_{core}^2 J_l'(\kappa_1 R)}{\kappa_1 J_l(\kappa_1 R)} + \frac{n_{clad}^2 K_l'(\kappa_2 R)}{\kappa_2 K_l(\kappa_2 R)}\right) = \left[\frac{l\beta}{k_0 R}\left(\frac{1}{\kappa_1^2} + \frac{1}{\kappa_2^2}\right)\right]^2 \tag{2.15}$$

where $J'(x)$ and $K'(x)$ are the first derivative of the Bessel functions $J(x)$ and $K(x)$. Equation (2.15) will generally have multiple solutions for each value of l which are labelled with $p = 1, 2, 3...$ in order of decreasing propagation constant: ($\mathbf{E}_{lp}$, β_{lp}). These solutions, which are called the guided modes, form a set which describe the ways light can possibly propagate in the fibre. Depending on the wavelength and geometry of the fibre there will be a different number of modes guided in the fibre. There also exist solutions of Eq. (2.12) that do not exponentially decay in the cladding. These solutions are described as radiative modes. Light in radiative modes does not propagate longitudinally and rather radiates out of the fibre. The combination of guided and radiative modes form a complete set in step-index fibres.

2.1.3 Optical modes and multi-mode guidance

A formal definition of an optical mode can be given as a field that maintains the same transverse distribution and polarisation at all locations along the waveguide. The properties of an optical mode describe how light will behave in that mode.

By observing a few special cases of the electric field profiles of the guided modes for a step-index fibre, a common nomenclature can be determined which is applicable to circularly symmetric optical fibres. For azimuthal index, $l = 0$, the solutions are either transverse electric, TE, or transverse magnetic, TM. The electric field lines of TE_{0p} modes consist of concentric circles whilst the field lines of TM_{0p} modes are in the radial direction. For $l \neq 0$, modes are hybrids with $l > 0$ named HE_{lp} and $l < 0$ named EH_{-lp}. For each HE and EH mode there also exist two orientations of the electric field as shown in Fig. 2.2 which, for a perfectly circularly symmetrical optical fibre will be degenerate, that is their propagation constants, β, will be identical.

The fundamental mode of a fibre is the mode which has the highest propagation constant. In a single-mode fibre this will be the only guided mode. The fundamental mode is not the TE_{01} or TM_{01} mode for which $l = 0$ but the HE_{11} for which $l = 1$. In the HE_{11} and indeed for all HE_{1p} modes the axial field component compared to the transverse components is very small and often taken as negligible whilst the transverse field lines are all orientated in a single direction, which is to say that the mode is linearly polarised (LP). In this case the two degenerate orientations of the electric field are generally described as the x and y polarisations. This system can be extended to the higher order modes to form a different orthogonal basis. A set of four orthogonal, linearly-polarised modes can be formed as linear combinations of the two HE_{21} and the TE_{01} and TM_{01} modes; likewise for the two HE_{31} and two EH_{11} modes and in general for the four modes of $EH_{x,p}$ and $HE_{x+2,p}$ for any $x \geq 1$ as shown in Fig. 2.2. The aforementioned sets of modes are only strictly degenerate under the weakly guiding approximation, $n_{core} \approx n_{clad}$, and to describe modes as linearly polarised is also only an approximation. Despite this the LP basis is often more

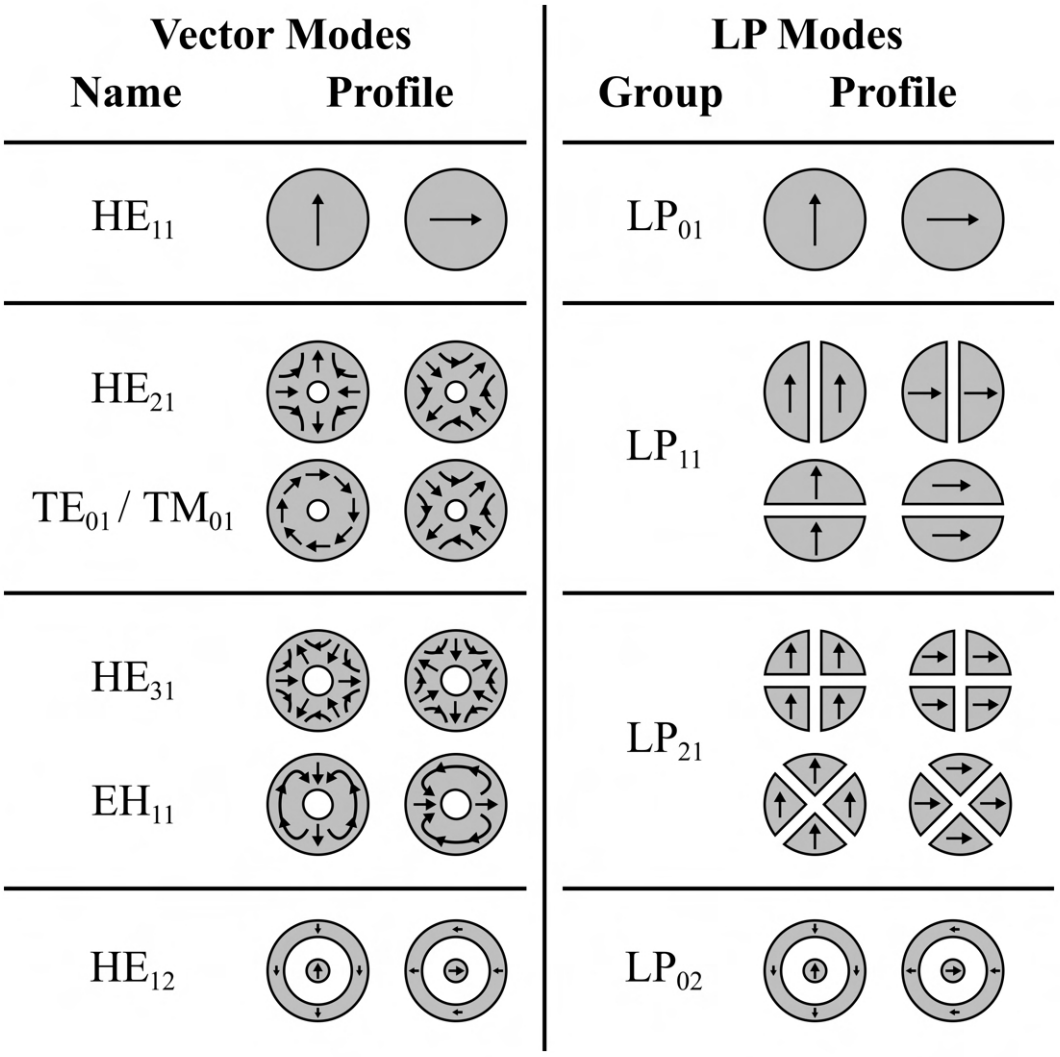

FIGURE 2.2: Transverse profiles of the first few core modes of a circular fibre. Vector modes are shown alongside their LP modes. Shaded regions indicate the transverse intensity profile and arrows indicate the electric field vector. *Adapted from [55] and [18]*

convenient and furthermore allows vector modes to be simply divided into groups which have similar propagation constants, dispersion etc.. Figure 2.2 shows illustrative plots of LP and vector modes and demonstrates the mode groups to which they belong.

2.1.3.1 Modal coupling

When a fibre end-face is illuminated by an electric field, in general 100 % of the incident power will not be transferred into a single optical mode, but rather multiple modes will be excited and carry some fraction of the power. Since light in different modes behaves differently, and indeed may not be guided at all, determination of the coupling into the fibre is of great importance.

The discrete guided modes and continuum of radiative modes in an waveguide form a complete and orthogonal set. The orthogonality condition for the normalized, guided modes can be expressed as:

$$\iint \vec{\mathbf{z}} \cdot \left(\mathbf{E}_k \times \mathbf{H}_q^* + \mathbf{E}_q^* \times \mathbf{H}_k \right) \mathrm{d}A = \delta_{k,q} \tag{2.16}$$

where $\mathbf{E}_k$ and $\mathbf{H}_k$ are the electric and magnetic field profiles of the k^{th}mode, $\vec{\mathbf{z}}$ is the unit vector in the longitudinal direction, * denotes the complex conjugate and $\delta_{k,q}$ is the Kronecker delta function which evaluates to 1 if $k = q$ and 0 otherwise. Since the modes form a complete set any incident field, $\mathbf{E}^{(\mathrm{i})}$ and $\mathbf{H}^{(\mathrm{i})}$, can be described as a linear summation of the fibre modes:

$$\mathbf{E}^{(\mathrm{i})} = \sum_k c_k \mathbf{E}_k \quad \text{and} \quad \mathbf{H}^{(\mathrm{i})} = \sum_k c_k \mathbf{H}_k \tag{2.17}$$

By combining Eqs. (2.16) and (2.17) the field transmission coefficient, c_k, for a mode k can be determined as:

$$c_k = \iint \vec{\mathbf{z}} \cdot \left(\mathbf{E}_q \times \mathbf{H}_k^* + \mathbf{E}_k^* \times \mathbf{H}_q \right) \mathrm{d}A \tag{2.18}$$

The power transmission coefficient into mode k is then $|c_k|^2$ and if the incident field is also normalized according to Eq. (2.16) then $|c_k|^2$ is also the input coupling efficiency into mode k. Coupling efficiency into multi-mode fibres is considered in Section 5.2.1.

In Section 2.2 hollow-core fibres are described which guide light by a different guidance mechanism and results in a different class of leaky modes that are inherently lossy. These fibres are the subject of this thesis and will later be discussed in detail, however, a brief mention should be made of how the coupling theory discussed here applies to hollow-core fibres. Equation (2.16) is only approximate for leaky modes. There are stricter orthogonality conditions which can be applied to leaky modes but they are a purely mathematical construct and do not provide any physically intuitive insight [56]. Despite being only approximately valid, Eq. (2.16) is adequate for performing modal decomposition where the optical loss is small as is the case for the fibres discussed in this thesis [57].

2.1.3.2 Group velocity and dispersion

The phase constant is the phase velocity of a mode, the rate at which a phase front changes with respect to position. In fibre optic applications it is usually more useful to consider the rate at which optical power propagates along the fibre, the group velocity:

$$v_g(\lambda) = \left(\frac{\partial \beta}{\partial \omega}\right)^{-1} = c_0\left(n_{eff} - \lambda\frac{\partial n_{eff}}{\partial \lambda}\right)^{-1} \tag{2.19}$$

which is the rate at which an amplitude envelope propagates. Hence, the group velocity could, for example, be used to calculate the time of flight for a pulse to propagate down the length of a fibre or in a distributed sensing application to determine the spatial position from which light is being backscattered. A waveguide is a dispersive medium and there are several factors that could lead to temporal spreading of a pulse.

Group velocity is generally a function of wavelength and so two different optical frequencies will experience a different delay. This chromatic dispersion is quantified by the group velocity dispersion (GVD):

$$D_\lambda(\lambda) = \frac{\partial}{\partial \lambda}\left(\frac{1}{v_g}\right) = -\frac{\lambda}{c_0}\frac{\partial^2 n_{eff}}{\partial \lambda^2} \tag{2.20}$$

which is defined as the differential delay per unit wavelength difference, per unit propagation distance. The GVD can be positive or negative, referred to as anomalous and normal respectively, and will generally be zero for specific wavelengths. For a silica step-index fibre this is near 1300 nm, however, since the zero dispersion wavelength can impose severe non-linear effects there are a wide variety of modifications to shift it to longer or shorter wavelengths [58]. Non-dispersion-shifted SMF-28 fibre has a GVD of around 20 ps/nm km at 1550 nm.

A modulated, or pulsed, light source occupies an optical bandwidth. For an unchirped, temporally-Gaussian pulse with full width half maximum pulse duration, τ_0, and central wavelength, λ_0, the wavelength bandwidth is:

$$\Delta\lambda_0 = \frac{\lambda^2}{c_0}\frac{4\ln(2)}{\tau_0} \tag{2.21}$$

where $\ln(x)$ is the natural logarithm. For example a 100 fs Gaussian pulse centred at 1550 nm has a bandwidth of 35 nm and will experience pulse broadening in a waveguide. Shorter pulses, which in telecommunications can be equated to faster single-channel data rates, occupy larger bandwidths and therefore generally suffer increased chromatic dispersion. One measure of the severity of chromatic dispersion is the dispersion length which is defined as the distance of propagation over which the pulse duration increases by a factor of $\sqrt{2}$. For an initially unchirped Gaussian pulse the dispersion length is:

$$L_{GVD} = \frac{2\pi c_0}{\lambda_0^2}\frac{\tau_0^2}{|D_\lambda|} \tag{2.22}$$

Clearly, a shorter pulse duration or higher GVD will reduce the length over which that pulse can be transmitted before it suffers from severe temporal broadening.

Another dispersion mechanism in few- or multi-moded fibres is inter-modal dispersion. Non-degenerate modes have different dispersion relations and therefore different group velocity. When pulsed light is propagating in multiple modes the different group velocity introduces a delay between them and therefore the overall pulse duration is increased. Inter-modal dispersion can be quantified using the differential group delay (DGD) which is defined as the differential delay between the slowest and fastest modes per unit length of propagation. DGD can be very limiting for high data rates in multi-mode fibres and is a significant topic of research in Chapter 5.

One design of solid-core, multi-mode fibre with reduced DGD is the graded index (GI) fibre. The refractive index profile in this design changes gradually from the centre to the edge of the cladding. This allows a greater degree of control of the modes compared to a step-index fibre. The use of a parabolic refractive index profile minimises the DGD and thereby the penalty on data-rate.

2.1.3.3 Power flow and loss

The Poynting vector, $\mathbf{S}_{instantaneous} = \mathbf{E} \times \mathbf{H}$, describes the 3-dimensional, instantaneous flow of power within a mode in a waveguide. When dealing with sinusoidally varying fields, however, it is more common to work with the time averaged version also referred to as the Poynting vector

$$\mathbf{S} = \frac{1}{2} \mathrm{Re}(\mathbf{E} \times \mathbf{H}^*) \tag{2.23}$$

Unless otherwise stated, mode profiles in this thesis refer to a plot of the axial component of S_z. In Chapter 3 the Poynting vector is used to understand the geometric sources of loss in fibres of interest.

When solving for the modes of a step-index fibre, since an infinite cladding and a completely transparent medium was assumed, the modes were lossless: possessing a purely real propagation constant. More generally the propagation constant and hence effective index are complex numbers with the imaginary component describing the attenuation of the field amplitude along the length of the fibre. For guided modes, such as those in a TIR fibre, optical losses arise from material concerns such as absorption and Rayleigh scattering. The fibres discussed in this thesis have different guidance mechanisms which result in leaky modes for which some optical power leaks from the fibre. This is termed confinement, or leakage, loss. Bending a fibre is a

geometric deformation which will also generally lead to an increase in confinement loss. Sources of loss in optical modes are discussed further in Section 2.2.1.2.

2.2 Hollow-core Fibre

Hollow-core refers to fibres with an air core and in which almost the entirety of the light is transmitted in air. The incentive toward hollow-core is that chromatic dispersion, scattering losses, material absorption and non-linearity can all be drastically reduced. Unlike TIR fibres, hollow-core fibres have a low to high refractive index change between the core and cladding. They must therefore employ different, inherently lossy, guidance mechanisms to their solid core counterparts which until recently have limited their appeal in application. Phenomenal progress into hollow-core fibre research in recent decades, however, has demonstrated remarkably low loss. As a very limited example, Fig. 2.3 shows the loss spectrum of three single-mode hollow-core fibres. Not only is the loss limit of solid-core reached at the very important C and L telecommunication bands [22], but it is also fundamentally beaten at shorter wavelengths [59] that nevertheless have significant uses. Applications at wavelengths across all these bands are discussed in this thesis. These designs and more are discussed in detail in Section 2.2.3. This section begins with a short historical overview followed by a description of the theory underlying these remarkable achievements.

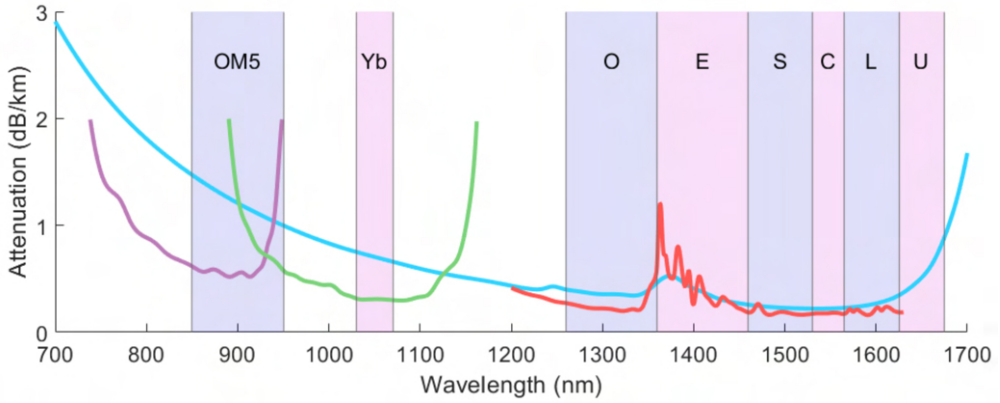

FIGURE 2.3: The loss spectrum of three fabricated hollow-core ARFs (red, green and purple) compared to that of Corning SMF-28 solid-core fibre (blue). Highlighted are several wavelength ranges of interest for this work: (OM5) the optical multi-mode 5 specification used in short haul telecommunications, (Yb) the operating wavelength of 1 µm Yb^{3+} based lasers, (O,E,S,C,L,U) the wavelengths used in long-haul telecommunication. The fibres shown are: (purple and green) 2^{nd}window NANFs [59] and (red) a first window DNANF [22]. First and second window refers to the concept of anti-resonant windows, described in Section 2.2.1.

Investigations of hollow-core fibres goes back to the advent of fibre optics as a field. In the early 1960s the invention of the laser led to great interest in using light for data

transmission and at the time glass had yet to be made transparent enough to transmit over great distance. Marcatili and Schmeltzer found the loss of hollow, cylindrical, dielectric waveguides could be made arbitrarily low by increasing the size of the core. At a wavelength of 1 µm with a core radius 1000 times larger at 1 mm attenuation of 1.85 dB/km was predicted. Bending loss however, was found to be prohibitively high even for infinitesimal bends. In the previous example the attenuation was doubled for a bend of radius 10 km [18]. It was concluded that such sensitivity to bending would make hollow-core fibres unsuitable for long haul telecommunications. Then in 1966 Kao and Hockham published their seminal paper, enabling the manufacture of high transparency silica TIR fibres. Solid-core fibre became the indisputable, dominant technology for the next 5 decades.

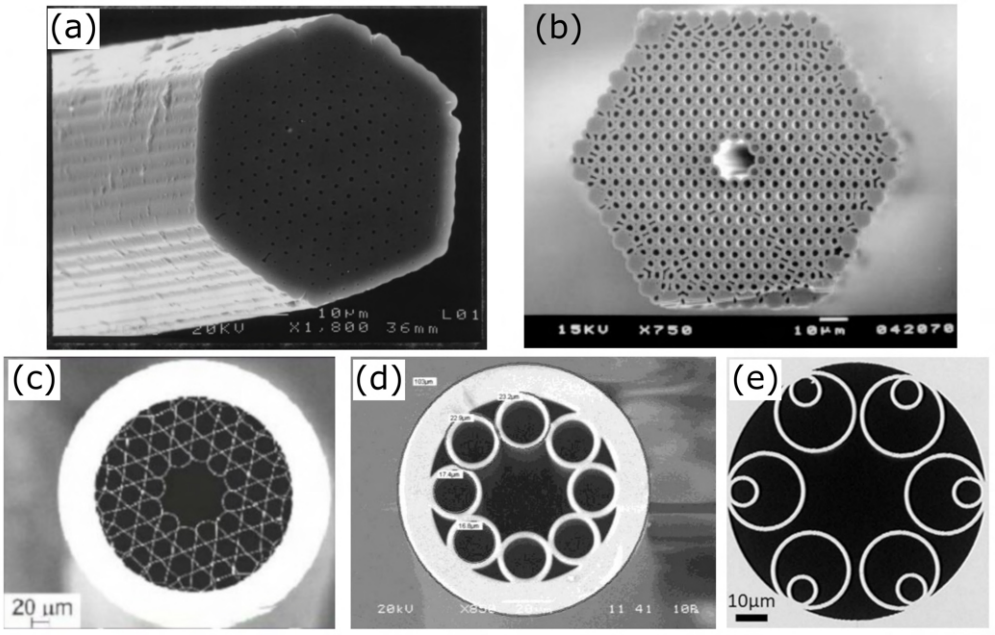

FIGURE 2.4: A selection of early scanning electron microscope images charting the development of micro-structured optical fibres: (a) the first fabricated solid-core PBGF by Knight *et al.* in 1996 [60], (b) a fabricated hollow-core PBGF from the 90s [19]. (c-e) are all examples of anti-resonant fibres moving from (a) the Kagomé lattice [61] to the simplified tubular fibres [62] and finally to the NANF [35].

This started to change in the 1990s; microstructured optical fibres began to be developed aiming to incorporate photonic crystals into the cladding [63]. At first these fibres were fabricated by drilling holes into bulk silica, e.g. Fig. 2.4(a), but soon more complex structures with an intricate microstructure were being made by stacking hollow silica tubes in the preform, e.g. Fig. 2.4(b), [19]. As well as reducing loss at conventional wavelengths, hollow-core guidance presented novel opportunities, for example transmission in the mid-IR [64, 65], novel nonlinear interactions [58] or enhanced light-gas interaction [66]. Since then there has been an incredible rate of development of hollow-core technologies resulting in entirely new designs, greater theoretical understanding and ever increasing performance. This is a far from an

exhaustive history and further information can be found for example in the reviews of Russell, Hayes *et al.* and Yu *et al.* [67–69]. In the following sections the guidance mechanism and properties of the class of fibres which are the subject of this thesis are described.

2.2.1 Anti-resonant fibres

Anti-resonant fibre (ARF) is a design of hollow-core fibre where guidance is by coherent reflections from a micro-structure cladding. In ARF, reflections from thin glass membranes in the cladding interfere constructively at certain wavelengths, where they are at resonance, presenting poor confinement, but at anti-resonance the light is strongly confined to the core. The earliest example of anti-resonant guidance was in the Kagomé fibre, a hollow-core fibre geometry first demonstrated in 2002 for which the cladding consists of a lattice configuration as shown in Fig. 2.4(c) [66]. More recent designs with a simpler micro-structure and better performance are discussed in Section 2.2.2.

The transmission spectra of AR fibres is a series of low-loss anti-resonant windows bounded by high-loss resonant peaks [70]. The positions of the resonant frequencies are well described by the ARROW model which treats cladding membranes as optical resonators and therefore the resonant and anti-resonant frequencies depend on their thickness [71]. In the ARROW model the resonant wavelengths are described by:

$$\lambda_m = \frac{2t}{m}\sqrt{n_{\text{glass}}^2 - n_{\text{air}}^2} \tag{2.24}$$

where $m = 1, 2, 3...$, n_{air} and n_{glass} are the refractive index of the hollow-core and glass regions, and t is the thickness of the cladding membranes. For an air-filled hollow-core fibre, $n_{air} \approx 1$. The fundamental window will generally allow the largest operation bandwidth but higher order windows may be targeted if, for example, the required thickness makes a fibre difficult to fabricate [35, 72]. It has also been shown that almost 2% higher input coupling efficiency is possible for single-mode ARFs operating in the second anti-resonant window [73]. Control of the position of the transmission windows is crucial in ARF design and it is useful to normalize the operating wavelength to these windows. The normalised frequency [68]:

$$F = \frac{2t}{\lambda}\sqrt{n_{\text{glass}}^2 - n_{\text{air}}^2} \tag{2.25}$$

For example, a silica membrane 600 nm thick would have the first resonance at 1250 nm placing the telecommunications wavelength 1550 inside the fundamental anti-resonant window with a normalised frequency, $F = 0.8$. This is demonstrated in Fig. 2.5 which shows the numerically simulated loss spectrum of an ARF with

thickness 600 nm. The simulation techniques used will be described in Section 2.3. Positions of the anti-resonant windows are well predicted by Eq. (2.25) and since they are evenly spaced in frequency, higher-order windows are narrower in wavelength bandwidth.

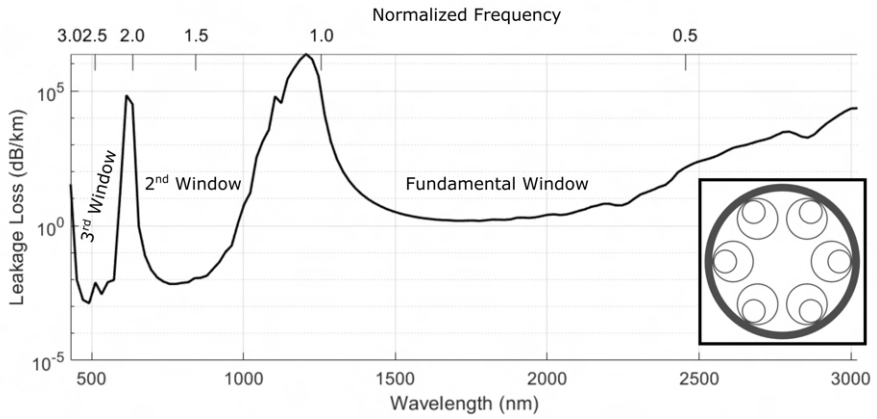

FIGURE 2.5: The leakage loss spectrum of a 6-tube NANF similar to those typically fabricated. The geometry of the fibre is shown in the inset and has core radius 15 µm, capillary thickness 600 nm and inter-capillary gap 4 µm.

2.2.1.1 Higher order modes

The behaviour of higher-order modes (HOMs) differs significantly in ARFs compared to TIR fibres. The core-guided modes of ARFs are not guided in the sense of TIR fibres; neither exclusively guided or radiative but somewhere between the two, leaky modes exhibit some leakage as light is guided along the fibre [74, 75]. Since the modes of hollow-core fibres are not guided there is no strict guided cut-off condition and ARFs have an infinite number of leaky modes. However, unlike in TIR fibres where loss is largely governed by material properties, the guidance mechanism of ARFs introduces large differential loss between HOMs. For example, using the model of [18], in the 1 mm hollow-core cylindrical, dielectric waveguide described in the previous section, the fundamental mode loss is 1.95 dB/km whereas the next lowest loss mode is more than double, 5 dB/km. With high differential loss between modes, practically leaky modes can only be considered as guiding light if the loss of those modes is sufficiently low for the application they are to be used in. The origin of differential loss in ARFs of interest is the subject of Chapter 3.

Effectively single-mode guidance is achieved in ARFs by designing the fibre such that HOMs are selectively stripped from the fibre. The microstructure cladding in ARF includes air cavities that guide their own set of leaky modes but with substantially higher losses than core-guided modes. Cladding modes are in close proximity to the core and so core guided modes will readily couple into the cladding if their phase constants are similar, a situation called phase matching [76]. The cladding

microstructure can be designed so that cladding modes are phase matched to higher-order core modes and therefore, any power in these modes is transferred into the cladding and then radiates out of the fibre over a very short distance [10]. The ability to selectively strip HOMs is one of the great strengths of ARF and in many cases simple design rules exist to achieve this [77].

In this thesis, it is of interest to achieve few- and multi-moded guidance in ARFs. Clearly this requires fibres to be designed to avoid phase matching between higher-order core and cladding modes, but equally to avoid or mitigate the high differential loss between modes in ARF. This is the subject of Chapter 4.

2.2.1.2 Sources of loss

Leakage is an inherent source of loss in the modes of ARFs but it is not the only, nor necessarily the greatest, source of loss. The different loss mechanisms are briefly described here and it will be discussed in Section 2.3 how, in this thesis, they are determined from numerical modelling.

Since the confinement of low-loss ARFs is high, the vast majority, typically $> 99.99\%$ [10], of optical power flows in the air core, for which Rayleigh scattering is negligible [78]. The cladding microstructure, however, does incur some surface scattering loss (SSL). The fabrication process of ARFs inevitably leads to roughness at the air/glass boundaries due to frozen-in thermodynamic fluctuations. Where the mode fields overlap with the boundary, light is scattered proportional to the power flow at the boundary [79]. Since reduced confinement generally results in higher electric field intensity at the air/glass interfaces higher-order modes with increased leakage loss will also exhibit higher SSL.

A uniform or gradual bend applied to a fibre causes additional leakage loss as the fields and propagation constants of the fibre modes are modified [80]. Bending loss is generally more severe for tighter bends and larger core radius. In ARFs, modification of the phase constant, the real component of the propagation constant, due to bending can additionally cause increased coupling between core and cladding modes [81, 82] which is often the significant source of bending loss. More details of this effect are given, for example, in Section 4.2.2. Since the ability to guide light in flexible fibres is one of the great strengths of optical fibre, determination of the limits of bending due to loss is of crucial importance for most practical applications.

Micro-bending describes the impact of small-scale mechanical perturbations on the modes. Discrete perturbations are understood to cause local coupling of power between the modes of the fibre [83]. In an ARF with high differential modal loss this generally results in additional loss. Although micro-bending can be purposefully induced [48], generally of more interest is the effect of randomly distributed bends

along the fibre length. In such cases power is lost at an average rate per unit distance. In a single-mode ARF, for example, micro-bending will cause a fraction of power guided in the fundamental mode to couple into the next HOM with adjacent azimuthal index. This mode is designed to have high loss in an effectively single-mode ARF and so the transferred power is radiated away before further perturbation can cause it to be coupled back into the fundamental mode [84]. The extreme low-loss of current single-mode ARFs being fabricated makes micro-bending an important consideration [36, 85]. The increased leakage loss of HOMs in multi-mode ARFs considered in this work generally makes micro-bend of less interest than reducing differential leakage loss.

2.2.2 Tubular and nested tubular anti-resonant fibres

Tubular fibre is a type of ARF that possesses a far simpler cladding but has been shown to be capable of excellent performance. Whereas PBGFs and Kagomé are fabricated with lattices of tubes, tubular fibres consist of a single ring of capillary tubes surrounding the core. The first tubular fibre was fabricated in 2011 and is shown in Fig. 2.4(d) [62]. The relative simplicity of this structure belies its potential for performance and in the years following there have been a series of improvements on the initial tubular design capitalising on this potential.

One undesirable feature of fibres formed of a lattice of touching tubes, such as Kagomé, arises during fabrication where the touching of capillaries leads to nodes acting as additional optical resonators [62, 86]. These nodes support high spatial-order glass-guided modes which easily couple to the core-guided modes at their resonant wavelengths leading to significant losses [87]. While reducing the cladding to a single ring of tubes significantly reduces the number of glass nodes, they still existed in early tubular fibres where the tubes are touching. The introduction of non-touching tubes all but eliminated this problem [71].

Figure 2.6(a) shows the geometry of a tubular fibre with non-touching tubes. The size of the inter-tube gap, d, is well known to have a significant impact on loss [11]. To target low-loss operation at specific wavelengths, it is common to design tubular ARF with a specific gap size, core size, R, number of capillaries, T, and capillary wall thickness, t. The inner radius of the cladding capillary tubes, R_1, in terms of these parameters is:

$$R_1 = \frac{2\sin(\pi/T)(R+t) - 2t - d}{2 - 2\sin(\pi/T)} \tag{2.26}$$

The designs of most ARFs currently fabricated and under investigation are based on this tubular design. In the following sections, several such designs are described and

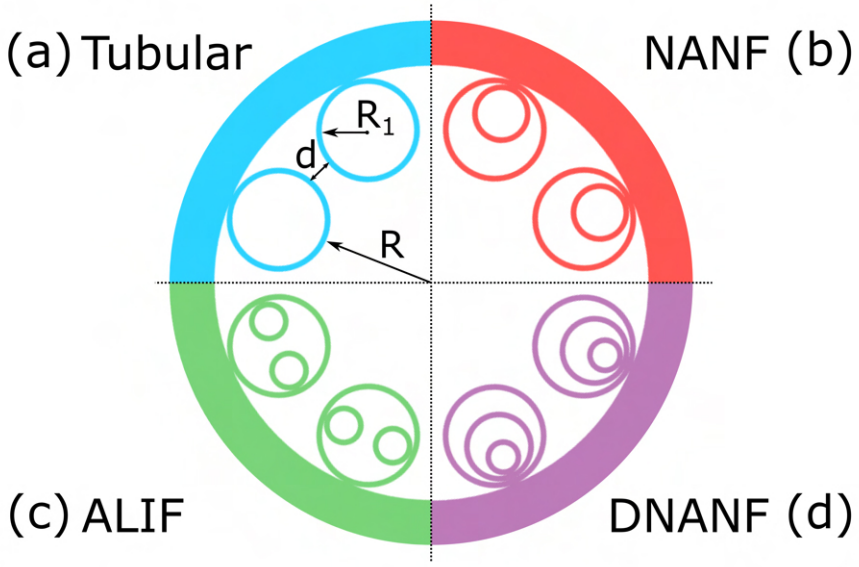

FIGURE 2.6: The geometries of (a) a tubular fibre, (b) a NANF, (c) an ALIF and (d) a DNANF.

discussed. Whilst these designs demonstrate superior performance compared to tubular fibres, they require a more complex cladding microstructure whilst exploiting the same basic guidance principles. For this reason the investigation into the origins of differential modal loss in Chapter 3 focuses on tubular fibre.

2.2.2.1 Nested-element anti-resonant nodeless fibres

The Nested-Element, Anti-Resonant, Nodeless Fibre (NANF) is a novel design first proposed by Poletti in 2014 [10]. A fabricated NANF is shown in Fig. 2.4(e) and Fig. 2.6(b) shows a diagram of its cross section compared to a tubular fibre. The nested element of a NANF is an additional smaller tube placed inside the outer capillary and fixed at the outer edge of the cladding. This modification shows not only a dramatic decrease in confinement loss but also a significant decrease in bending losses [88], e.g. more than 4 orders of magnitude lower losses for 80 µm core diameter at 8 cm bend radius [10, 82]. The outer capillaries are non-touching and there are no extra glass nodes compared to a tubular fibre.

As discussed previously the confinement loss of this family of fibres is comparable to their scattering losses. Numerical studies have found that the minimum loss in subsequent anti-resonant windows is well fitted by a λ^7 curve [10]. Scattering losses meanwhile are well known to follow a λ^{-1} trend. A larger core radius also decreases both confinement and scattering loss with an R^{-8} and R^{-3} dependence respectively. NANFs can also be designed to be effectively single mode without compromising the low-loss behaviour. One then record-low-loss NANF demonstrated in 2019 also achieved a higher order mode extinction ratio of over 1000 times [36]. This

demonstrates one of the great strengths of NANFs; beyond their impressive performance NANFs afford great control by simple geometric parameters. For example, by scaling up the entire fibre whilst maintaining tube thickness the confinement and scattering loss can be reduced whilst maintaining single-mode operation [10]. NANFs are generally considered a proven technology, with 100s of km of single-mode fibre produced in the lab, demonstration of coherent WDM data propagation through multi-thousand km distances [89] and commercial NANF cables already available. For all these reasons, the investigations into multi-mode ARF in Chapters 4 and 5 begin or focus on NANFs.

2.2.2.2 Anti-resonant leakage inhibited fibres

One modification of the NANF design came by using a geometric approach to analysing the sources of loss in the fibre. Jasion *et al.* conducted numerical simulation of NANFs and analysed the results using transverse power flow streamlines. This analysis revealed a counter-intuitive approach to improving on the NANF design [85]. Decreasing the size of the gap between outer capillaries is well known to reduce confinement loss which suggests that these gaps are a source of loss. The transverse power flow analysis, however, showed that the majority of the leakage was actually occurring through the nested capillary and that the gap was effective at confining light.

Anti-Resonant Leakage Inhibited Fibres (ALIFs) replace the nested element of a NANF with a pair of nested tubes. A cross section of this design compared to a tubular fibre or NANF is shown in Fig. 2.6(c). ALIFs have been shown in simulation to achieve over two orders of magnitude reduction in confinement loss versus NANFs [85]. In Chapter 4 ALIFs are considered for few-mode, low-loss guidance for short-haul telecommunication applications.

2.2.2.3 Double nested-element anti-resonant nodeless fibre

The double nested-element anti-resonant nodeless fibre (DNANF) uses two nested elements, as in an ALIF, but in a nested configuration, as shown in Fig. 2.6(d). DNANFs were first proposed at the same time as the NANF structure [10] but a fabricated example has only recently been reported [22]. The additional nested element provides an extra degree of confinement and reduces leakage loss. The fabricated DNANF described in Ref [22] is the first hollow-core fibre to reach the loss level of solid-core fibre at 1550 nm. Design of the cladding of DNANFs for multi-mode operation is discussed in Chapter 4.

2.2.2.4 Overview of additional anti-resonant fibre designs

Since the great potential of anti-resonant fibres has become clear, a great many designs have been suggested and in some cases fabricated. A complete and detailed review of these works would be a difficult and nuanced undertaking and shall not be attempted here. Instead, a few designs which have shown particular promise theoretically or practically will be mentioned.

The conjoined tube structure has outer tubes formed of two capillaries bonded together in a figure-of-eight-like configuration with a straight bar between them. This design was fabricated in 2018 and exhibited impressive 2 dB/km attenuation at 1512 nm [34]. This might be considered an early example of anti-resonant fibre formed of two concentric rings of outer cladding tubes instead of or in addition to nested elements. Several variations on these double-ring ARFs have been studied theoretically and show some promise for low-loss guidance in a single-mode regime [90–93]. A similar concept that has been practically fabricated is the hybrid Kagomé-tubular fibre design which in 2021 exhibited 1.6 dB/km at 1050 nm [94].

None of these designs are discussed further in this thesis, with the focus instead on fibres such as the NANF and ALIF, previously discussed, which possess a simpler micro-structure that has proven easier to fabricate. These fibres also present the opportunity for an excellent degree of control over the air regions in the micro-structure by simple geometric parameters which it will be shown is important for multi-mode guidance.

2.2.3 Recent achievements in fabricating single-mode ARF

Anti-resonant fibres are most commonly fabricated by a 2-stage stack and draw process. An initial preform is constructed of capillary tubes stacked in the desired orientation of the final fibre, the outer diameter of a preform is typically on the order of several cm, this is drawn through a vertical furnace where it contracts transversely. This results in a cane, with an outer diameter of several mm, which is placed in a thick jacket tube and once again drawn down, in a furnace, under tension to the dimensions of the final desired fibre design. During this second stage there are a variety of factors at work including but not limited to, surface tension, gas pressure and variable temperature and viscosity, which result in complex and difficult to control process [27]. This thesis does not seek to describe in any detail the fabrication process but it is important to note that it is a very complex one and that many of the loss reductions in single-mode ARFs demonstrated in the past decades have come about by improvements in fabrication. Some notable recent achievements are listed here.

2.2.3.1 0.22 dB/km NANF at 1550 nm

The lowest loss NANF to date of which I am aware was reported in 2020 by Jasion *et al.* [21]. Targeting the telecommunication wavelengths around 1550 nm, the NANF had 6 outer tubes and a core diameter of 37 µm. 0.28 dB/km loss was measured from 1510 to 1600 nm.

2.2.3.2 0.174 dB/km DNANF at 1550 nm

The first ever reported DNANF, reported by Jasion *et al.*, also targeted the telecommunication wavelengths and was comprised of 5 outer tubes each with 2 nested capillaries and a core diameter of 28 µm [22]. It was also the first hollow-core fibre ever to match the loss of solid-core fibre, 0.174 dB/km, at telecommunication wavelengths, a significant step for hollow-core fibre research. The loss spectrum of this fibre is shown in Fig. 2.3.

2.2.3.3 Low-loss NANFs at 850 and 1070 nm

The telecommunication bands are chosen since they are the lowest loss points of solid-core silica which makes matching this loss in hollow-core an impressive result. One of the great strengths of hollow-core fibres is to guide light at wavelengths where the absorption or scattering of solid-core silica is too high. NANFs have been reported by Sakr *et al.* which have loss lower than the fundamental limits of solid-core silica at shorter wavelengths: 0.6 dB/km at 850 nm and 0.3 dB/km at 1070 nm [59]. These are both very important wavelengths for short-haul telecommunications, which are discussed in Chapter 4, and for power deliver with high-power 1 µm Yb^{3+} based lasers, discussed in Chapter 5.

2.3 Numerical modelling of ARFs

In this thesis numerical simulation is used to study ARF. Analytical solutions exist for many azimuthally symmetric geometries, that is geometries for which the refractive index is a function of radius only. Bird, for example, presents models of ARFs consisting of concentric rings alternating between air and glass [95]. Estimation techniques have also been developed for a variety of types of geometry from arbitrary index profiles of solid cores to the complex cladding micro-structures and lossy, radiative modes of hollow-core fibres [96, 97]. None of these solutions, however, have the accuracy and robustness of numerical simulation which are discussed here.

Most properties of an optical fibre can be measured experimentally. Determination of the modes is a more difficult task. Light not perfectly matched to a single mode will couple into multiple modes and separating them is complex, for example S2 imaging [98]. Numerical simulation allows a depth of interrogation far beyond what is possible experimentally, for example, separating out the loss contributions from scattering, absorption and leakage or resolving the loss contributions spatially. With simulation a wide range of fibres can be studied without the need for costly fabrication and without the influence of any fabrication defects on the results. Even fibre that could never be fabricated can be simulated and often has analytical significance.

The finite element method (FEM) is by far the most common numerical simulation technique, not just in optics but across a great many fields in physics, engineering etc.. It is a fully vectorial technique that allows flexible and efficient determination of the range of fibres investigated by simulating a 2-dimensional cross section and exploiting the symmetry of the problem. A commercial FEM software package, COMSOL Multiphysics, is used in this work. In addition, bespoke software is employed to setup, run, extract data from the COMSOL software and analyse it. A version of this simulation code, collectively developed by this project's supervisors, Prof. Francesco Poletti, Dr. Eric Numkam-Fokoua and Dr. Gregory Jasion, was generously shared at the inception of the doctoral project. Over the course of the project I implemented a great many modifications and enhancements in order to, for example, simulate a range of novel fibre geometries, enhance the ability to simulate multi-mode fibres (some of which are described in Section 2.3.1), perform novel analysis of simulation results and simulate fibres with a built-in twist (described in Appendix B).

In the body of this thesis ideal fibres are simulated, but the fabrication process generally results in variation in the thickness of the capillary walls, the position and size of capillary tubes and the emergence of larger glass nodes in the cladding. Appendix A presents an overview of some of the techniques and work completed during the course of this project simulating realistic, fabricated fibres largely with the aim of supporting the work undertaken in the Optoelectronics Research Centre to fabricate low-loss single-mode NANFs.

2.3.1 Modelling steps in finite element simulation

The wave equation, Eq. (2.8), can readily be converted to a 2-dimensional problem by considering the general solution for an optical mode:

$$\mathbf{E}(x, y, z) = \tilde{\mathbf{E}}(x, y) \exp(-i\beta z) \tag{2.27}$$

where $\tilde{\mathbf{E}}$ is the transverse electric field. Substituting Eq. (2.27) into Eq. (2.8) and simplifying yields a Eigenvalue problem with the complex valued eigenvalue, β

describing the fibre dispersion and loss and the eigenvector $\tilde{\mathbf{E}}$ describing the transverse electric field profile from which the magnetic field can also be calculated.

The geometry of the fibre can be described as a series of polygons and input into COMSOL. Each region in the domain can then be assigned a material which dictates the refractive index in that region. In this work the refractive index of air was taken to be 1 and the wavelength dependent Sellmeier equation, Eq. (2.6) was used to approximate the refractive index of fused silica. The finite element process involves dividing the simulation domain into a large but finite number of subdomains, commonly known as meshing. For a 2-dimensional cross section triangular elements allow flexible filling of the geometry. COMSOL allows a significant degree of automation in this step via powerful meshing algorithms, designed with knowledge of the physical problem, that can adjust the density of the mesh to better describe the expected solution. A denser mesh more closely resembles the true, continuous nature of the physics and therefore generally results in a more accurate solution; however it also increases the computation time and memory required to complete the simulation. Convergence tests based on the mesh parameters showed that practically the most significant factor for accurate results when simulating ARFs was enforcing several mesh elements, i.e. at least 5 elements, across the thickness of the thin glass capillary. Convergence tests were conducted whenever significantly different geometries or wavelengths were to be simulated.

By meshing, the problem is discretised and for each finite element the equation describing the Eigenvalue problem is enforced, forming a set of equations. Each set of element equations can use the local material properties which allows discontinuous or exotic material properties to be modelled. The element equations are then combined into a global set which can be solved using the optimised numerical algorithms built into COMSOL. When solving the Eigenvalue problem it is important to specify how many solutions are to be found before finishing the search. In single-mode fibres, only the first few modes are of interest. When investigating multi-mode fibres, up to several 100 solutions might be required. Knowledge of the number of expected modes for a given geometry is important since finding additional solutions also increases computational time. This also presented a challenge for conducting post-processing the data, since all the solutions must be labelled in order to the identify, for example, core modes, cladding modes and in many cases the full vectorial designation of a mode (see e.g. Fig. 2.2). A number of algorithms were developed over the course of this work to assist in this process. These considered the effective index and fraction of power in the core to estimate the nature of the mode although some manual verification or correction was almost always required.

When solving a structure that possesses mirror-symmetry in one or multiple axes it is possible to exploit this symmetry and simulate only a subdomain of the whole geometry. Any tubular-based fibre with evenly spaced and regular outer capillary

tubes has one axis of symmetry and it is possible to simulate a half structure, a π sector. Any tubular-based fibre with an even number of evenly spaced and regular outer capillaries (for example those shown in Fig. 2.6) can be simulated with a quarter structure, a $\pi/4$ sector. Doing so greatly reduces the computational time and resources required to solve the problem. Boundary conditions must be applied to these symmetry boundaries which can be chosen as Dirichlet (perfect electric conductors) or Neumann (perfect magnetic conductors) conditions which results in solutions being limited to a set of modes, as described by McIsaac [99]. When simulating a half structure there are two possible boundary conditions, in a quarter structure there are 4 possible permutations. Since multi-mode fibres are investigated in this work it is useful to have knowledge of all the modes of the fibre. The solution employed here was to simulate the reduced geometry but repeat the simulation for all the possible permutations of boundary condition. Despite the need for multiple simulations, this was found to result in significant improvement in overall computation time. In addition, knowledge of the boundary conditions for which a particular solution was found limited the possible set of modes it could belong to, which simplified the mode identification algorithms mentioned above.

2.3.2 Perfectly matched layers

In FEM is is necessary to truncate the infinite area of the real world to a finite, preferably small, computational domain. In purely guided modes such as those of a TIR fibre it may be possible to simulate a large cladding but to accurately model the leaky modes of ARF it is necessary to employ a perfectly matched layer (PML).

By adding an extra layer around the edges of the simulation region that is designed to attenuate any signals passing through it, the field strength can be artificially reduced to negligible levels at the edge of the computational domain. In so doing any spurious reflections are suppressed [100]. PMLs must also have the same impedance as the edge of the fibre to prevent reflections at the fibre / PML interface. It has been shown that a well performing PML allows accurate computation of the leaky modes of hollow-core fibre [10, 101, 102]. In this work the built-in PML of COMSOL is found by convergence experiments to be sufficient for the fibres considered here; a cylindrical PML no less than 1/8th the radius of the core is used. The exception to this is the twisted fibre simulations described in Section 5.1.3 for which a bespoke PML was developed that is described in that section.

2.3.3 Modelling of bent fibres

Conformal transformations provide a method for the analysis, simulation and intuitive understanding of fibres with a gradual, constant bend. Heiblum *et al.* showed

that by considering the geometric transformation between a curved and straight waveguide, the material refractive index can be modified to model the curved waveguide [103]. Strictly the transformation involves multiplication of the refractive index of the curved waveguide by $\exp(x/R_{\text{bend}})$, however it is more common to use a first order approximation. In this case the modified refractive index $\hat{n}$ is described by:

$$\hat{n}(x,y) = \left(1 + \frac{x}{R_{\text{bend}}}\right) n(x,y) \tag{2.28}$$

for a bend around a vector parallel to the y-axis at a distance of R_{bend} from the centre of the fibre (the bend radius) where $n(x,y)$ is the refractive index of the bent waveguide. A bend about the x-axis can be modified by replacing x with y in Eq. (2.28). Note that simulating a bent fibre in this manner will modify the mirror-symmetry of the fibre cross section and it is necessary to simulate a half- or full-structure to model bending.

2.3.4 Calculating loss in numerical simulation

The use of well-designed PMLs allows the leakage loss of leaky modes to be calculated directly from the propagation constant. If simulating a bent fibre this will include the additional leakage loss due to bending. Bending loss can be determined by comparing the loss of the bend fibre with that of the same straight fibre. Although not described in the work shown in this thesis, the effects of material absorption can also be included in FEM, in which case the imaginary component of the propagation constant also incorporates the additional loss due to material absorption. The total loss can be calculated from the effective index and is most commonly expressed in decibels per unit length:

$$\alpha_{dB/m} = \frac{20}{\ln 10} \frac{2\pi}{\lambda} \operatorname{Im}(n_{eff}) \tag{2.29}$$

Surface scattering loss occurs where the mode fields overlap with the air/glass boundary. Light is scattered proportional to the power flow at the boundary and the loss associated with SSL can be estimated from the results of FEM. The normalised electric field intensity is given for a mode k by [104]:

$$\Gamma_k = \sqrt{\frac{\epsilon_0}{\mu_0}} \frac{\oint_B |\mathbf{E_k}|^2 \mathrm{d}l}{\iint \vec{\mathbf{z}} \cdot (\mathbf{E}_k \times \mathbf{H}_k^*) \mathrm{d}A} \tag{2.30}$$

where the line integral in the numerator covers the air/glass interfaces in the fibre cross section, B. Strictly, the scattering due to the electric field will depend on the power spectral density of the surface roughness [105], a very difficult quantity to measure. In practice an estimate that assumes the roughness is process-independent,

and that therefore all fabricated fibres have the same roughness, has shown accurate results against measured fibres [21, 36, 106]. Under this assumption the SSL can be estimated as:

$$\alpha_k^{(\mathrm{SSL})} = \eta \left(\frac{\lambda}{\lambda_0} \right)^{-3} \Gamma_k \tag{2.31}$$

where η is a normalisation parameter, calibrated at a wavelength λ_0. In this work a normalisation parameter of $\eta = 300$, calibrated at a wavelength $\lambda_0 = 1550\,\mathrm{nm}$ is used [10].

2.4 Summary

In this chapter, a broad introduction to the physics of fibre optics has been presented, discussing the fundamental equations which describe the operation of a waveguide and the emergence of optical modes that are of crucial importance for understanding optical fibres. Properties such as latency, dispersion and optical loss have been discussed and how these relate to fibre optic applications. Next, the background and a brief history of hollow-core and in particular ARF was described. The unique guidance properties resulting in high differential modal loss as well as low-latency, low non-linearity and the potential for unique gas-light interaction were discussed. This culminated in a brief review of some of the phenomenal results recently achieved in fabricating low-loss NANFs and DNANFs, including those with loss matching that of solid-core fibre at 1550 nm and some achieving lower loss at shorter wavelengths. Finally FEM, used to numerically simulate and investigate ARF in this thesis was discussed.

In the next chapter the results of an investigation into the origins of differential modal loss in ARF geometries of interest are presented.

Chapter 3

Origins of Differential Modal Loss in Multi-mode Anti-resonant Fibre

Despite the abundance of work and interest into designing, analysing and fabricating single-mode ARF, an all-encompassing model for predicting the loss of the fundamental and higher modes of ARFs remains beyond reach, as solving Maxwell's equations even for the simplest such structures must make use of numerical tools. Higher-order modes have in fact received little attention as the research focus has firmly been on effectively single moded fibres. Indeed, simple design rules have been developed [10, 77] to make the fibres effectively single mode, whereas few works have considered multi-mode operation in these fibres [47, 49].

In this thesis the goal is to design and study the possibilities of multi-mode ARFs. In this chapter the mechanisms of leakage loss in ARF are explored. It is shown by an intuitive understanding of this mechanism in ARFs and numerical simulation that, away from the glass resonances, leakage results from the coupling between the core-guided and the radiative modes supported in the rest of the structure. When core and lossy cladding modes are phase-matched, the result is prohibitively high leakage loss for the core mode. Reducing the loss therefore requires a large separation in effective index between core and cladding modes as well as minimum spatial overlap between their mode fields. Results are presented describing this relationship, which demonstrate which cladding modes are most significant for different geometries and it is discussed how to leverage these ideas for the design of few-moded hollow core fibres.

The chapter is organised as follows. Section 3.1 describes how leakage loss depends on mode order and the basic geometric parameters of the fibre. It is also discussed how leakage loss is related to other modal properties such as scattering loss and fraction of power propagating in air. Analytical models for simpler ARF geometries exist and their relevance to the tubular fibres of interest is discussed. In the remainder

of the chapter a deeper understanding of leakage loss in higher-order modes is sought by considering leakage as coupling to radiative modes in the cladding; Section 3.2 describes the theoretical basis for this postulate. In Section 3.3 it is demonstrated that the most significant source of leakage in low-loss geometries is the cladding modes confined in the tubes surrounding the core. The leakage loss of the fundamental and higher-order core modes is shown to be directly related to the degree of coupling to these cladding modes. This allows the study to continue only considering leakage by coupling between core and cladding tube modes, greatly simplifying the analysis and permitting deeper insight. In Section 3.4 the methods described and justified in the previous sections are used to quantitatively analyse leakage loss. A model for approximating leakage loss is developed that considers the strength of coupling between core and cladding modes. Comparison to loss attained by numerical simulation shows good agreement with this model which considers only the first three cladding tube modes.

The work described in Sections 3.2-3.4 has been previously been published in [107].

3.1 Higher-order mode properties

In order to illustrate the differential properties of higher-order modes in ARF, tubular fibres with a range of core sizes were numerically simulated. The geometry of one of these fibres is shown in Fig. 3.1(a). The radius of the cladding capillaries and the inter-capillary gap were kept constant, both with a value of 5 µm ($R_1/\lambda = d/\lambda = 3.2$), and the number of tubes was modified to control the core radius. Figure 3.1 shows the modal leakage loss (see Section 2.3.4) for the first 9 mode groups of these fibres near the minimum loss point of the fundamental anti-resonant window, normalized frequency $F = 0.6$. Leakage loss is increased for higher-order modes; for the largest fibre shown, with normalized core radius $R/\lambda = 22.8$, the leakage loss of the fundamental LP_{01} mode group is 0.05 dB/km compared to 0.6 dB/km in the LP_{03} mode group, a differential loss of 0.55 dB/km. As with the fundamental mode, leakage loss of HOMs increases with smaller core sizes, as does the differential loss between modes. For the fibre with $R/\lambda = 12.1$, the differential loss between the LP_{03} and LP_{01} mode group is 40 dB/km.

The loss of a mode group in Fig. 3.1(b) is considered to be the average loss of all the modes belonging to that group. Some mode groups have non-negligible differential loss between their constituent modes, notably those with azimuthal index 1 (LP_{11}, LP_{12}, LP_{13} etc.) due to the presence of transverse-electric and transverse-magnetic modes [18, 95]. This is discussed later in this chapter; however commonly there is negligible differential loss between modes belonging to the same mode group (see e.g. Fig. 3.6).

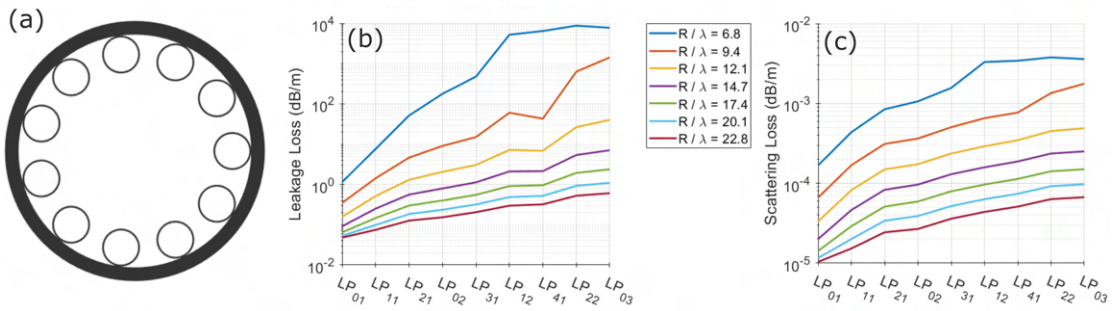

FIGURE 3.1: (a) the cross section of a tubular fibre with 11 tubes, gap and tube radius $d = Z_1 = 5\,\mu\text{m}$ and normalized core radius $R/\lambda = 12.1$. The modal (b) leakage and (c) surface scattering loss of the first 9 mode groups of a series of tubular fibres with increasing core size.

In ARF, surface scattering can be a significant source of loss in the fundamental mode, dependent on the nature of the geometry (tubular, NANF etc.), core size and wavelength [10]. The scattering loss, calculated using the techniques described in Section 2.3.4, for the same fibres and modes as discussed previously is shown in Fig. 3.1(c). The trend is very similar to that of leakage loss; loss is increased for higher-order modes and both loss and differential loss is decreased for larger cores. The magnitude of scattering loss in these fibres is approximately three orders of magnitude lower than leakage loss, as expected in tubular fibre.

The similarity in behaviour between leakage and scattering loss suggests a link between these two mechanisms. Indeed, scattering loss is proportional to the electric field intensity at air/glass interfaces [104] whilst leakage loss is a measure of the confinement of the mode with lower confinement leading to higher intensity at the core/cladding boundary. This relationship is captured in Fig. 3.2 which shows both the fraction of power propagating in the core and the scattering loss as a function of leakage loss. Data points are taken from a large set of simulations of tubular fibres with normalized core size ranging between $R/\lambda = 20$ - 116. All the core-guided modes found in simulation, up to 64 modes per geometry, are plotted. In both plots (the fraction of power in the core, Fig. 3.2(a), and the scattering loss, Fig. 3.2(b)) there is a strong correlation with leakage loss: regardless of the dimensions of the tubular fibre considered, modes with the same leakage loss have very similar scattering loss. Higher leakage loss results in higher scattering loss and less power propagating in the core. Here the relationship is only shown for the modes of tubular fibre at a single wavelength but the same is true of other ARF geometries at wavelengths far from coupling to dielectric modes [87] although the exact proportionality is different.

This observation is not directly useful since leakage loss is typically determined by numerical simulation in which case exact information about scattering and power is readily available. It does, however, indicate that leakage loss is the quantity to study when considering the behaviour of these modes; at the same wavelength and without

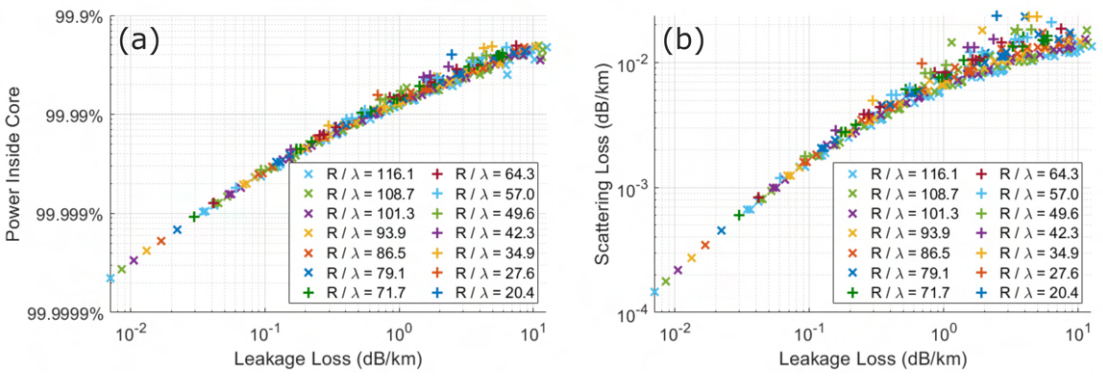

FIGURE 3.2: The (a) fraction of power inside the core region and (b) the scattering loss as a function of leakage loss for all the modes of a large range of tubular fibres. The colour and shape of the markers denote the geometry of the fibre.

drastic modification of the geometry (i.e. a NANF versus a tubular fibre) improving the leakage loss results in a commensurate improvement in scattering loss and air-guidance fraction. Likewise a theoretical understanding of the leakage loss can improve our understanding of those properties of the fibre and is the focus of this chapter. This is not, generally, the case for the dispersion properties of the modes, e.g. group delay and chromatic dispersion which are considered in Section 5.1.1.

3.1.1 Analytical solutions of similar geometries

The loss of ARF geometries which consist of concentric rings of air and glass has been calculated analytically by Bird [95]. Although these concentric ring fibres are structurally dissimilar to tubular fibres, and indeed typically cannot exist practically, these models can provide useful insight into tubular fibres. Concentric ring fibres can be characterised by an integer, N, the number of anti-resonant layers (including both air and glass regions) which make up the cladding. Examples of geometries are shown in Fig. 3.3(a) for a range of values of N. The fibre with $N = 0$ is not anti-resonant but rather is the hole-in-bulk-silica structure studied by Marcatili *et al.* [18]. The fibre with $N = 1$ is a floating thin-walled capillary, $N = 2$ is a thin-walled capillary surrounded by an air region surrounded by a glass jacket etc..

The leakage loss of the mode of a concentric ring ARF has been determined in decibels per unit length as [95]:

$$\alpha = \frac{20}{\ln 10} \frac{\lambda^{N+2}}{R^{N+3}} \left(\frac{u_{mn}}{2\pi} \right)^{N+2} \nu \prod_{i=1}^{N} \frac{1}{\sin^2(\phi_i)} \tag{3.1}$$

with R the core radius, λ the wavelength and N the previously described number of anti-resonant rings. Equation (3.1) clearly describes how the dependence of loss on core size and wavelength increases with additional anti-resonant layers. The leakage

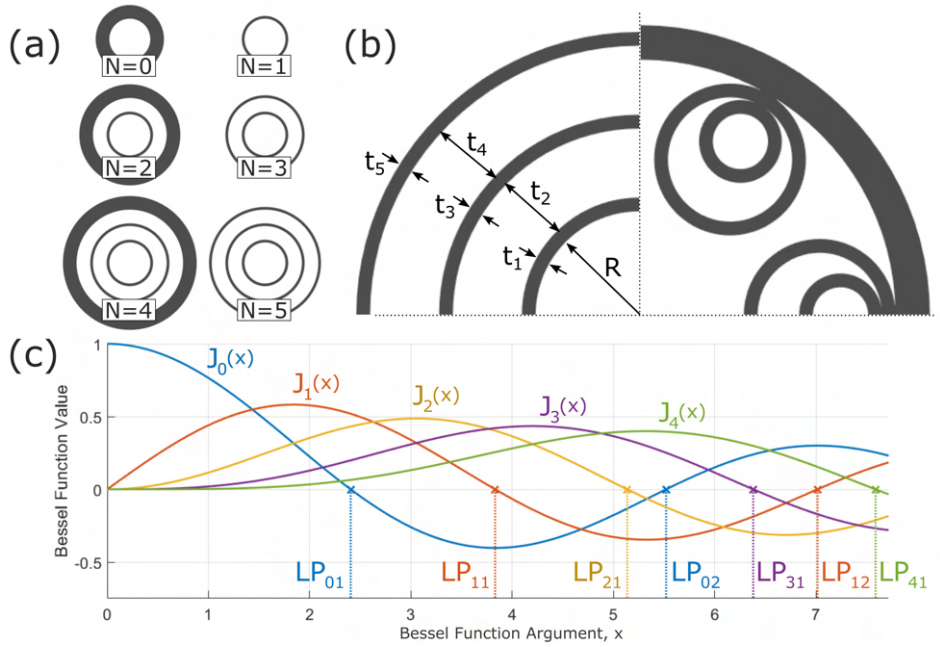

FIGURE 3.3: (a) Geometries of several concentric ring structures characterised by the number of anti-resonant layers, N, as in [95]. (b) The geometric parameters of an $N = 5$ concentric ring fibre alongside a NANF. (c) The first 5 Bessel functions and their zeros in the interval 0-8 which characterise the modes of the first 7 mode groups of ARF.

loss of the fundamental mode of a NANF is proportional to λ^7 and R^{-8} [10], indicating equivalence to a $N = 5$ concentric ring structure consistent with Eq. (3.1). Figure 3.3(b) compares the geometry of a $N = 5$ concentric ring structure to a NANF. Their equivalence in loss dependence suggests that the combination of the thin-walled capillaries near the jacket and the jacket itself act similarly to an additional anti-resonant glass layer. The behaviour of tubular fibre, without a nested element, lies somewhere between an $N = 2$ and $N = 3$ concentric ring structure but practically an $N = 3$ structure it typically used for comparison [49]. It should be stressed that although similar in dependence on core size and wavelength, tubular and NANF structures typically exhibit lower loss than their "equivalent" concentric ring structures for the same core size and wavelength [10]. For example, in this thesis, loss reductions by a factor of around 5x were commonly found in NANFs compared to similar concentric ring structures but this is highly dependant on the exact geometry of both fibres. The source of this increased confinement is attributable to reduced coupling between core and cladding modes in tubular fibres and NANFs, a concept which is investigated in this chapter. Equation (3.1) is used in Section 5.2 to calculate the minimum core size of multi-mode NANFs.

In Eq. (3.1) u_{mn} is a dimensionless quantity related to the transverse wavevector in the core and characterises the mode order, depending on the radial and azimuthal index. For the modes belonging to the LP_{mn} group u_{mn} is the n^{th} non-trivial zero of the Bessel function J_m. The value of the Bessel zeros dictates the order of mode groups in ARF.

The first 7 zeros are associated with the first 5 Bessel functions and their values are shown in Fig. 3.3(c). The order of Bessel zeros is the same order as the order of modes arranged by leakage loss, e.g. in Fig. 3.1(b).

The constant ν describes the dependence of loss on the refractive index of the dielectric material and depends on the nature of the mode:

$$\nu_{\mathrm{TE}} = \left(\frac{1}{\sqrt{\epsilon_r - 1}}\right)^{N+1} \qquad \nu_{\mathrm{TM}} = \left(\frac{\epsilon_r}{\sqrt{\epsilon_r - 1}}\right)^{N+1} \qquad \nu_{\mathrm{HE/EH}} = \frac{\nu_{\mathrm{TE}} + \nu_{\mathrm{TM}}}{2} \tag{3.2}$$

with ϵ_r the relative dielectric constant of the glass regions. For any effective waveguide $\epsilon_r > 1$ (for silica at 1550 nm $\epsilon_r \approx 2.1$), therefore, in the same mode group loss is minimal in the TE mode, maximal in TM mode and HE/EH modes are approximately the average of the TE and TM modes.

The final product term in Eq. (3.1) extends over the cladding layers and describes the transverse phase accumulated across each layer:

$$\phi_i^{(\mathrm{glass})} = \frac{2\pi}{\lambda_0} t_i \sqrt{\epsilon_r - 1} \qquad \phi_i^{(\mathrm{air})} = \frac{u_{mn}}{R} t_i \tag{3.3}$$

with t_i the thickness of the i^{th} cladding layer. The phase accumulated in the glass regions leads to the anti-resonant behaviour of the fibre: low-loss windows in the wavelength spectrum in-between high-loss resonant wavelengths, identical to those predicted by the ARROW model, Eq. (2.24), and well describing the behaviour of realistic ARFs of interest, e.g. Fig. 2.5. The optimum glass thickness where loss is minimised, as predicted by this model, is identical for all modes. An optimal thickness of air layers, however, is also predicted that depends on the mode order, u_{nm}. Eq. (3.1) predicts that loss is minimised when the ratio between the air thickness and the core is $t_i^{(\mathrm{air})}/R = \pi/(2u_{nm})$. Whilst there is no equivalent concept of optimal air thickness in realistic ARFs, the opposite, where loss of a particular mode is maximised is similar to the way in which single-mode guidance is engineered (see e.g. Section 2.2.1.1). Indeed, ratios between the size of the air region in the tube and the core have been found at which the loss of the LP_{11} mode is maximised [10, 77]. These geometric ratios correspond to maximum coupling between the LP_{11} core mode and the cladding mode guided in the air region inside the tubes. This observation suggests that cladding modes play a significant role in leakage loss and in this chapter the goal is to develop a model for understanding and predicting loss by considering the interaction of core and cladding modes.

3.2 Dependence of loss on geometric features

In ARFs, a carefully designed cladding allows light to be confined and guided in the central core region. Here, it is considered that the partitioned air regions created by the arrangement of the cladding tubes themselves form a collection of waveguides capable of supporting their own modes when isolated. These regions are the central hollow-core, the dielectric tubes, the hollow air-filled regions enclosed by the tubes, the spaces between the tubes, and the surrounding silica jacket.

When seen this way, the modes supported by the fibre are effectively supermodes of the full, complex structure and can therefore be conceived as a linear superposition of the modes of the individual constituent waveguides. Figure 3.4(c-g) shows contour plots of power distributions of modes confined predominantly in each of these constituent waveguides. It can be postulated that at wavelengths away from the resonances in the glass membranes, it is the coupling between the core guided modes of interest and these "cladding modes", which themselves suffer substantial attenuation as they can easily couple to radiation modes, which leads to leakage or confinement loss. The modes of the cladding are often far more readily analysed than those of the core. In this case, assuming the loss of these cladding modes is known, coupled-mode analysis can provide an important insight into the loss process of the core modes of interest. Indeed, such an approach has been employed previously in literature to explain the high loss suffered by the fundamental mode of hollow-core photonic-bandgap fibers in the vicinity of anti-crossing events with lossy surface modes [108, 109], and also extensively to interpret the loss in ARFs near the cut off of the modes confined in the glass membranes [110, 111]. In [108] it was shown that the additional loss due to coupling with a lossy surface mode would scale approximately as:

$$\alpha \propto \frac{\gamma|\kappa|^2}{(\Delta\beta)^2} \tag{3.4}$$

where γ is the assumed known loss of the cladding mode, κ the amplitude coupling coefficient between core and cladding mode and $\Delta\beta$ is the difference between their phase constants. Despite being an approximation, Eq. (3.4) shows powerfully that the stronger the spatial overlap between the two mode fields (as captured by the coupling coefficient κ), the stronger the loss. Further, and more importantly, the closer the separation between their phase constants (smaller $|\Delta\beta|$), the higher the loss. It is precisely this latter effect that is exploited in designing effectively single mode hollow-core fibers, i.e. by matching the phase constant of the lowest-order HOM to that of the fundamental lossy cladding mode, ensuring that all other HOMs also suffer significantly high loss [10, 59, 77]. Interestingly, the Lorentzian shape of Eq. (3.4) has

been found to explain very well the loss of core modes in ARFs near the cut-off of the dielectric tube modes [110, 111].

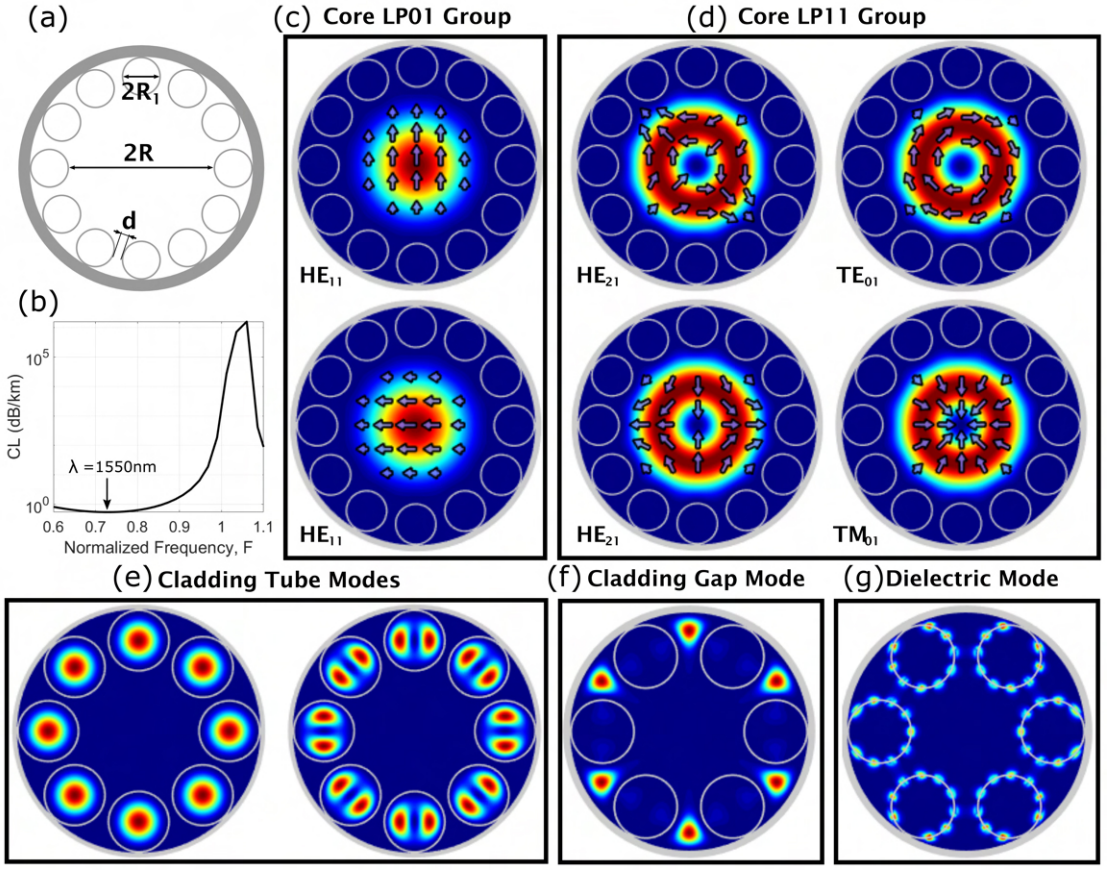

FIGURE 3.4: (a) The geometry of a tubular fibre. (b) Confinement loss spectrum of the fundamental core mode of (a) showing the fundamental anti-resonant window plotted as a function of normalized frequency F. Representative examples of (c,d) the core modes and (e,f,g) the cladding modes existent in tubular and NANF ARFs; contour plots describe power flow in the axial direction and arrows denote the transverse electric field. In order to show clearer examples of cladding modes, different geometries have been chosen; these series of modes are present in all tubular fibres.

With this understanding, one can therefore postulate that the loss of a given core mode, α_p^{core}, is given by:

$$\alpha_p^{\text{core}} \approx \sum_q \frac{\gamma_k |\kappa_{p,q}|^2}{(\Delta\beta_{p,q})^2} \tag{3.5}$$

where the summation extends over all the discrete cladding modes and takes the meaning of an integral over the continuum of radiation modes of the silica jacket cladding. Whilst conceptually straightforward, the great difficulty in estimating the loss of the fibre using this expression lies in the fact that the summation extends over a large number of modes, many of which are not easily computed without the use of numerical simulation. This difficulty is greater still if the anti-resonant structure of

interest has non-uniformities in tube thicknesses or contacting tubes, because the contact points result in glass nodes which support modes of their own. It is paramount in the design of low-loss structures to avoid such contact points altogether, or alternatively to ensure they are located far away from the core region where the modes of interest are confined (to minimize the coupling coefficient κ) [10, 112–114].

The geometry of the fibre determines the modes to which the coupling is strongest and that result in leakage. In particular, for the same number of tubes a design with large gaps will necessarily have smaller capillaries which brings the surrounding silica jacket closer to the core region, thus increasing direct coupling between the core modes and the continuum of radiation modes supported by the silica jacket. When the gaps are smaller however, the silica jacket is sufficiently far away from the core and in the following sections a simpler analysis considering only the modes in the hollow regions of the cladding is shown to provide adequate insight. The analysis presented in this chapter is therefore restricted to such structures with small inter-tube gaps as they have higher potential for low-loss operation. In this thesis a small inter-tube gap is defined as $d < 4\lambda$ for operational wavelength λ, Fig. 3.4(a).

Under these conditions, useful simplifications can be made, leading to important physical insight into the core-guided modes and their differential loss. In particular, it is found that when the gaps between the tubes are small, loss of the core modes is dominated by coupling to the modes confined within the tubes, Fig. 3.4(e), as they are the largest of the cavities in the cladding. The loss of cladding tube modes is significantly higher than those guided in the core due to the proximity of the jacket glass, the smaller radius of the tubes compared to the core and the lack of a light confining micro-structure. For example, using Eq. (3.1) a tube of radius 19.5 µm, thickness 530 nm at wavelength 1550 nm, the loss is 50 000 dB/km [115]. Because the field distributions within such cylindrical tube waveguides and their propagation constants can be calculated analytically, this makes the analysis of the coupling process more tractable.

In the following section, the relationship between these cladding tube modes and the loss of the core-guided modes from a coupled-mode perspective is examined. Beginning with detailed numerical simulations that justify the restriction to the analysis of tube modes, the calculated loss is then compared to quantitative predictions from this analysis.

3.3 Core mode loss through coupling to tube modes

Great insight into the loss of ARF can be obtained by analyzing the Poynting flux in the radial direction at the perimeter of the fibre which indicates the local leakage loss from the structure. This azimuthally resolved radial Poynting flux, together with

transverse power flow analysis is a powerful tool that can link leakage loss to specific geometric features. For example, its use has led to the design of new fibre geometries with ultra-low leakage loss [85]. Here, similar analysis is applied to a tubular fibre, to reveal which cladding modes the light is coupled into as it leaves the core and show the results in Fig. 3.5. Using numerical simulation, the modes of a large-core ARF ($R = 32\lambda_0$), having 12 cladding tubes of radius $r = 0.26R$, thickness $t = 530\,\text{nm}$ and gap size $d = 5.8\,\mu\text{m}$ are found. A structure with 12 tubes was chosen that will guide many core modes with low loss. The wavelength of operation was chosen at $\lambda_0 = 1550\,\text{nm}$ that corresponds to a normalized frequency (Eq. (2.25)), $F = 0.71$ and is located at the minimum loss of the fundamental anti-resonant window (see Fig. 3.4(b)). At this wavelength, no mode guided in the thin silica membranes, Fig. 3.4(g), interacts appreciably with the core modes [87], suggesting that leakage via modes located in air alone should be able to account for the loss.

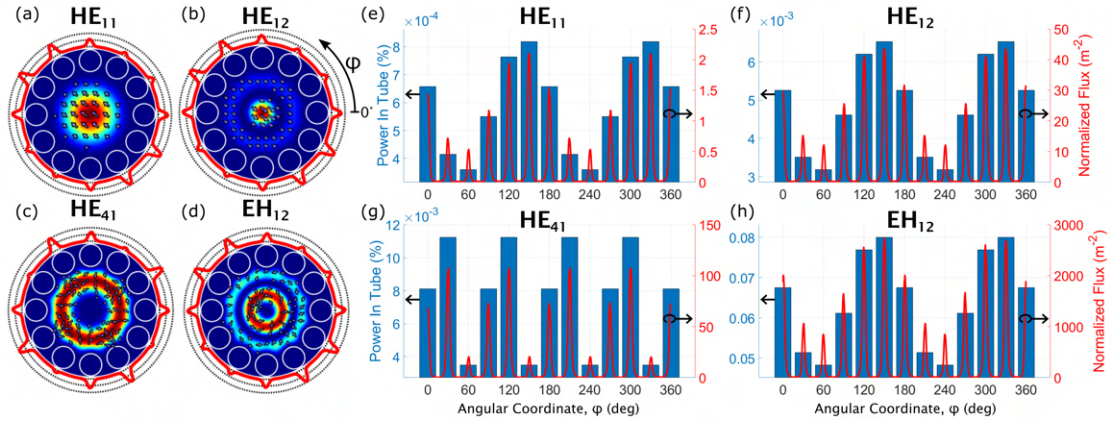

FIGURE 3.5: (a-d) Mode plots of several core modes that have been numerically simulated, black arrows superimposed on the mode denote the transverse electric field vectors. Around the perimeter of each mode figure is plotted the radial power flux (red line), normalized to the total modal power, as a function of the angular coordinate ϕ. (e-h) The percentage of the total modal power flow in the axial direction inside individual cladding tubes (blue bars) is superimposed with the normalized radial flux. In order to emphasize the relationship between the two quantities the bar for the tube at 0° is repeated at 360°.

In Fig. 3.5(a-d) shows the mode profiles of a representative selection of modes: the (a) HE_{11}, (b) HE_{12}, (c) HE_{41} and (d) EH_{12} core modes. The azimuthally-resolved loss at the outer boundary with the geometry of the fibre is overlaid. It can be seen that leakage loss peaks at the azimuthal locations of the tubes, indeed for all modes studied more than 90% of leakage loss occurs within ±5° of the centre of the tubes (in this structure each tube covers an angle of approximately 30°). This is indicative of the fact that the loss is caused by the coupling to the cladding tube modes. It can be observed that the magnitude of the peaks is different, depending on the azimuthal position of the cladding tube, e.g. in Fig. 3.5(a) the peaks are minimum at 30° and 210° and maximum at 150° and 330°. This can be attributed to the electric field polarisation; leakage loss is higher where the transverse electric field is normal to the jacket as expected when

considering the difference in reflection coefficient, described by Fresnel's equations, for s and p polarizations.

To confirm that coupling to tube modes is the origin of loss, the extent to which core modes are hybridised with cladding modes is examined. Note that this section does not discuss the mechanisms of coupling, but rather attempts to observe and quantify its effect in order to show that it is the cladding tube modes which are the significant source of loss. For each core mode the fraction of modal power is measured, given as the time averaged Poynting vector in the direction of propagation, that is located and propagating inside the cladding tube. Fig. 3.5(e) compares, for the fundamental HE_{11} mode, the power inside each tube to the azimuthally-resolved power flux. For all tubes, the relative magnitude of the tube power almost exactly matches that of the corresponding peak in the power flux. This is the case for all of the core modes considered (e.g. Figs. 3.5(f-h)). Considering other modes it can also be observed that the fraction of power in tubes increases with the mode order as does the total amount of leakage through the tubes; the maximum and minimum powers for the fundamental HE_{11} mode (Fig. 3.5(e)) are 2 orders of magnitude lower than the EH_{12} (Fig. 3.5(h)) mode. Given the strong association of loss to the degree of coupling it is logical to say that the primary source of loss is via the tubes. This is an indication that confinement loss can be directly linked to coupling to tube modes and that a tube coupling model can be used for quantitative prediction of the modal leakage loss.

As further evidence, Fig. 3.6 shows the correlation, for 40 core-guided modes, between the confinement loss and total fraction of power in the cladding tubes tubes. The fraction of power in the entire cladding (Region B in the inset of Fig. 3.6) increases with mode order as expected for less confined modes. However this is not proportional to the increase in confinement loss. The fraction of power in the tubes (Region A) on the other hand shows excellent correlation with confinement loss, supporting the claim that that the loss of all core-guided modes in tubular anti-resonant fibre is primarily due to coupling to tube modes.

An argument might be made that the described correlation between leakage loss and power guided in the cladding tubes can be explained with the statement that higher-order modes are less confined and therefore have more power propagating outside the core. However, using this analysis it is evident that, although increasing with mode order, power in the entirety of the cladding (Region B, green line in Fig. 3.6) does not show any meaningful correlation with confinement loss. It is interesting to note that despite this, for the relatively low-loss, lower-order, core-guided modes, most of the power in the cladding is propagating outside the tubes (in Region C). For the HE_{11} modes in this fibre, 0.12% of the total power propagates in the cladding (in Region B) over 96% of which resides outside the cladding tubes (Region C). As the loss increases a higher fraction of the cladding power is found to reside inside the tubes: for the HE_{22} mode 1.3% of the power propagates in the cladding of which 87%

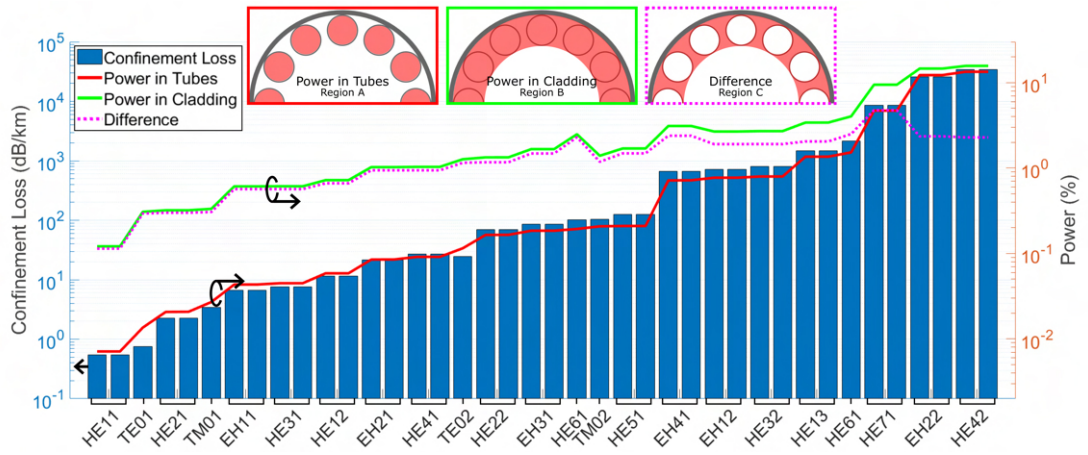

FIGURE 3.6: The confinement loss of the core modes of a large core tubular ARF (blue bars) and the percentage of the total modal power propagating in various regions of the cladding (lines), the regions A, B and C are highlighted in red in the insets.

propagates outside the tubes. Modes very near phase matching are strongly hybridised with cladding modes and the tubes are found to contain more power than the rest of the cladding: the EH_{22} mode has only 16% of power in the cladding propagating outside the tubes. This further supports the conclusion that the magnitude of leakage loss is strongly linked to the cladding tube modes.

3.3.1 Relation to NANF geometries

Air modes that are guided in the gap regions between the tubes account for some of the extra power in the cladding. From all that is shown above, it is logical to expect that these gap modes contribute significantly to loss in tubular anti-resonant fibres when the gap between the tubes is large as confirmed by the study in ref [116]. For lower loss geometries with smaller gaps, for example as defined in this thesis $d < 4\lambda$, these gap-modes have a much smaller impact compared to the tube modes. To compare this behaviour to designs with reduced leakage through tubes a 12-tube tubular fibre is contrasted with a NANF that is identical with the exception of the addition of a nested tube. Both fibres are shown together in Fig. 3.7(a) with their radial power flow at the outer boundary of the fibre. The fraction of the power lost through the tubes is compared to that lost through the gaps. In the case of the tubular fibre in Fig. 3.7(a), less than 5% of the total leakage is through the gaps. For the NANF in Fig. 3.7(b) the nested tube reduces the size of the cladding tube air regions and therefore increases the phase-mismatch between the core and cladding tube modes. This results in lower loss by, according to Eq. (3.4), reducing coupling to the tube modes. One can imagine that coupling to gap modes would be unaffected and therefore leakage associated with these modes would become a greater proportion of total loss. There is indeed a higher proportion of the total loss associated with the gaps in a NANF: 7.6%, 2.7% more than in the tubular fibre. This is a very small increase,

however, suggesting that leakage through gap modes is also decreased in a NANF compared to tubular fibre. The exact value of leakage through the gaps depends on the size of the nested element, with lower loss geometries having a higher proportion of that loss through the gaps [85]. The significance of tube and gap modes is discussed in detail in Section 4.2.3.

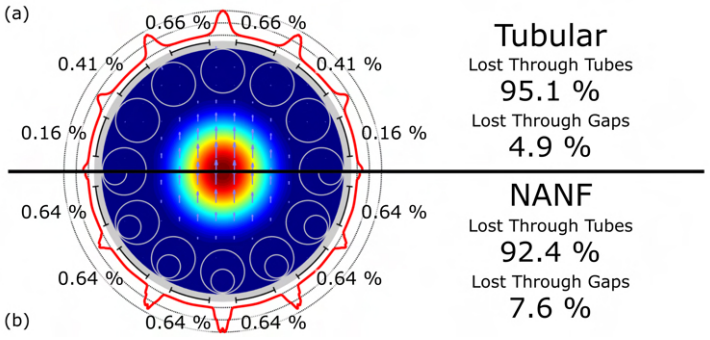

FIGURE 3.7: The normalized radial power flux at the jacket of the fundamental mode in (a) tubular and (b) NANF fibre. The black arcs centred on the gaps show a 12° angle. The loss through this angle is calculated and displayed as a percentage of the total loss.

What is clear from this analysis is that the majority of leakage loss in NANFs, as in tubular fibre, is associated with coupling to cladding tube modes. Therefore, although this study focuses on tubular fibre, the insights gained herein remain applicable to more complex ARFs with nested elements such as the NANF.

3.4 Model for analysing leakage loss

Having demonstrated that the primary source of confinement loss in low-loss tubular fibre is via coupling to the modes of the cladding tubes, the coupling process between core-guided modes and those tube modes is investigated. From Eqs. (3.4) and (3.5), the loss of a given core mode scales with the strength of its coupling to the tube modes and inversely with how well it is phase matched to such modes.

In this further investigation, it is studied how the loss of any core mode depends on the separation between its propagation constant and that of cladding tube modes. This required the simulation of a range of ARFs for which the propagation constant of the core and cladding modes can be specified. In [115], an analytical formula for propagation constants of HE modes confined inside a dielectric tube waveguide is presented as:

$$\beta = \frac{2\pi}{\lambda}\left\{n_{\text{air}} - \frac{u_{nm}^2}{2}\left[\frac{1}{n_{\text{air}}}\left(\frac{\lambda}{2\pi R}\right)^2 + \frac{1}{n_{\text{air}}^2}\left(\frac{\lambda}{2\pi R}\right)^3 \frac{\epsilon_r + 1}{\sqrt{\epsilon_r - 1}}\cot(\phi_{\text{glass}})\right]\right\} \tag{3.6}$$

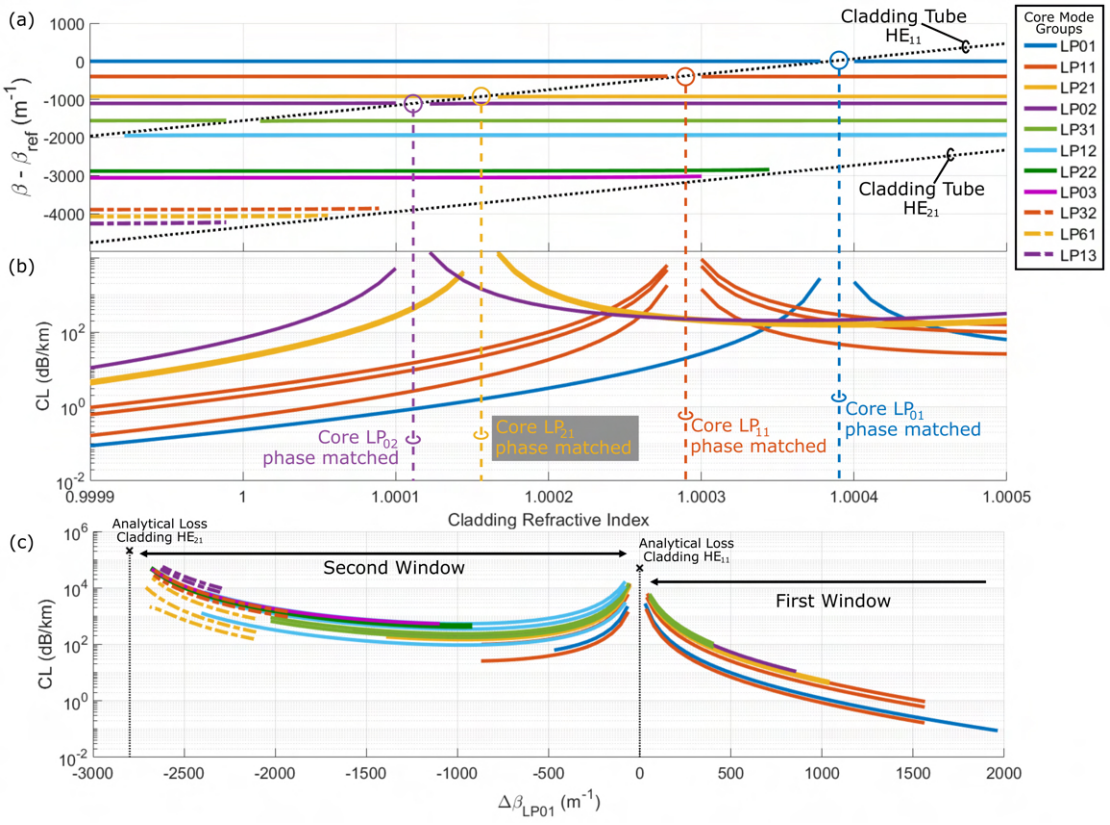

FIGURE 3.8: Numerical simulation of the tubular fibre (Fig. 3.4(a)) for which the refractive index of the air within the cladding tubes is controlled. (a) The propagation constant of the core and cladding modes relative to β_{ref} which is taken as the propagation constant of the fundamental, LP_{01}, core mode. The propagation constant of the cladding modes is calculated using Eq. (3.6). (b) The confinement loss of the first 4 core modes. The x-axis of (a) and (b) are shared; the vertical dashed lines highlight the points at which the propagation constant of the first 4 core modes intersects with that of the fundamental cladding tube mode. (c) The confinement loss of all the core modes plotted against their difference in propagation constant to the fundamental cladding modes. The black crosses indicate the predicted loss of the first two cladding modes using the model of Bird [95].

with n_{air} the refractive index of the air or gaseous medium. In this study, of interest is the propagation constant of the cladding tube modes and therefore R is taken as the radius of the cladding tubes, R_1. All other variables have the same definitions as in Eq. (3.1). It follows from Eq. (3.6) that the propagation constant of the cladding tube modes can be modified either through changing the size of the tubes, R_1, or by changing the medium with which they are filled, n_{air}. Changing the tube size to increase or decrease the effective index of the tube modes would result in either changing the number of tubes or the size of the gaps between them and the proximity of the jacket glass. Such changes to the geometry are known to impact the loss of the core modes on their own. Instead, in the simulations presented here the refractive index of the hollow regions inside the cladding tubes, n_{air}, is modified whilst keeping that of the core and of the glass constant and with no changes to the overall geometry. The magnitude of the change in refractive index is less than 0.1% of the contrast of air

and glass and so has a negligible impact on the anti-resonance conditions. Numerical simulations using this technique are used to study the effects on loss of the difference in phase constant between core and cladding tube modes.

3.4.1 Low-loss phase-mismatch windows

Figure 3.8 shows the results of this study in which the geometry of Fig. 3.4(a) is simulated with modified refractive index of the material within the cladding capillaries, varied between 0.9999 and 1.0005, in order to manipulate the propagation constant of the cladding tube modes. The fibre studied has an inner capillary radius of 19.5 µm and a wall thickness of 530 nm and the wavelength studied is 1550 nm. With these parameters the effective index of the HE_{11} mode, calculated using Eq. (3.6), is the same for a gas with refractive index 0.9999 as for air, refractive index 1, with a tube radius 1.9 µm smaller. Acquiring solutions for core modes with propagation constant lower than that of the HE_{21} cladding tube mode proved to be computationally expensive and time consuming, so the study is limited without loss of generality to modes above it.

Figure 3.8(a) confirms that the propagation constants of the core modes (coloured horizontal lines) are effectively constant, whilst those of the cladding modes (black dotted lines) vary approximately linearly with the refractive index. The propagation constant is plotted relative to that of the fundamental mode to make clearer the relationship with phase matching, quantified by the difference in propagation constant, $\Delta\beta$ in Eq. (3.4). Where the propagation constant of the core modes and fundamental cladding tube mode intersect, the phase match condition, $\Delta\beta \approx 0$ is satisfied and strong coupling occurs according to Eq. (3.4). Core modes belonging to the same LP mode group are typically approximately degenerate, their phase constants are nearly equal. Therefore the discussion is simplified by referring to modes using their LP group name from this point onward. When calculating cladding tube modes the phase constant and loss of the group is taken to be that of the HE mode belonging to that group.

In Fig. 3.8(b) the confinement loss of the first 4 core mode groups is plotted against the refractive index of the cladding gas medium and the points of phase matching are highlighted (dashed vertical lines). For each mode the loss increases as phase matching is approached. Very near to phase matching, owing to the strong hybridisation between core and cladding modes, it is very difficult to label the solutions of the numerical solver as specific core modes and so they are not included in this graphic. This results in the gaps noticeable near phase matching.

Figure 3.8(c) plots the confinement loss of all core modes versus the difference in propagation constant between the core and fundamental cladding tube mode. Here,

the notation is introduced: $\Delta\beta_q = \beta_{\text{core}} - \beta_q$ having the meaning of the difference in propagation constant between each core mode and the cladding tube mode group specified by the subscript q. Hence, phase matching with the fundamental, LP_{01}, cladding tube modes occurs at $\Delta\beta_{\text{LP01}} = 0$. The difference in phase constant between cladding modes remains approximately constant (see Eq. (3.6)) so phase matching to the second cladding mode, HE_{21}, occurs at $\Delta\beta_{\text{LP01}} = -2800\,\text{m}^{-1}$. Very near phase matching, $\Delta\beta \approx 0$, the strong coupling between core and cladding tube modes means that the loss suffered by the core mode is very similar to that of an isolated tube mode. The loss of such modes can be estimated as the $N = 1$ structure of Eq. (3.1). In Fig. 3.8(c) it is found that this analytically calculated loss well describes the asymptotic peak value of the core modes at phase matching.

Looking at the plots of Fig. 3.8(c), the Lorentzian-like behaviour of the loss as a function of $\Delta\beta$ can clearly be observed, as may be expected from Eq. (3.4). Indeed, at phase matching, all the core modes experience high loss as a result of the resonant out-coupling to tube modes. As $|\Delta\beta|$ increases, the loss falls off sharply towards a minimum value. This results in a series of low-loss "windows" between the phase matching points, conceptually similar to anti-resonant windows in wavelength that occur between the resonant modes in the glass membranes [110]. This phenomenon shall be referred to as "phase-mismatch" windows in this thesis.

For all the modes, the lowest loss is achieved in the first phase-mismatch window, i.e., $\Delta\beta_{\text{LP01}} > 0$ on the figure. Looking at Fig. 3.8(c), the minimum loss in the second phase-mismatch window is nearly two orders higher than the lowest loss achievable in the first. This can be explained by considering that in the second window not only the HE_{11} tube mode will contribute but also the lossier HE_{21} mode. This observation has practical significance when designing ARFs with specific modal properties. If for example multi-mode guidance is desired with relatively low differential loss between the modes, a strong goal in this thesis, then all desired core modes should preferably be guided in the first phase-mismatch window, $\Delta\beta_{\text{LP01}} > 0$. Conversely, when aiming to out-couple a specific mode, for example to achieve effectively single mode guidance, it can be more desirable to target a geometry that guides that core mode just inside the second phase-mismatch window rather than exactly at phase matching. For small, negative $\Delta\beta_{\text{LP01}}$ loss remains high and the fibre will be more robust against variations in fabrication or bending that would alter the propagation constants of core and cladding modes.

3.4.2 Quantifying coupling losses

To further investigate this coupling behaviour, the magnitude of the amplitude coupling coefficient, κ of Eq. (3.4), is examined. For two modes, p and q, described by their normalized electric fields, $\hat{\mathbf{E}}_p$ and $\hat{\mathbf{E}}_q$, for simplicity the overlap integral is

considered [116]:

$$\eta_{\mathrm{p,q}} = \iint \hat{\mathbf{E}}_p \cdot \hat{\mathbf{E}}_q^* \, dA \tag{3.7}$$

that is proportional to the coupling coefficient, κ. In coupled mode theory where we would effectively regard the fibre as a directional coupler made of the core and the lossy cladding tubes, one ought to rigorously consider the modes of these different structures when they are isolated and uncoupled. In this case however, an approximation is needed because the core cannot be defined as an isolated waveguide and therefore no analytical solution is available. With the knowledge of this difficulty, the core modes are approximated as those guided within the core when surrounded by the cladding tubes and which are obtained by finite element simulations. A similar approach to the approximation used here has previously been used by Deng *et al.* [116]. The electric fields of the cladding tube air modes can therefore be calculated analytically by treating them as isolated tubes, an approach previously employed in analysing the dielectric modes of the cladding tubes [110, 111]. In this section therefore, overlap integrals are calculated between core modes, the numerical solutions of the full fibre, and modes of isolated cladding tubes which are determined analytically.

There are a large number of tube air modes as each tube supports its own full set of modes. Since all the tubes in an ideal fibre are identical, however, all tube modes belonging to the same mode group have equal propagation constants. An overlap integral between a core mode p and a cladding tube mode group Q is therefore defined as:

$$\left|\eta_{\mathrm{pQ}}\right|^2 = \sum_q \left|\eta_{p,q}\right|^2 \tag{3.8}$$

where the sum extends over all tubes and all modes belonging to group Q.

Using the data set previously studied (i.e. Fig. 3.8), the overlap integral between the first three analytically determined cladding tube modes and the numerically solved core modes of the first 5 core mode groups, is calculated and in Fig. 3.9 is plotted against the difference in propagation constant of that tube mode. The lower x-axis describes the difference in propagation constant between the core mode and the cladding tube mode for which the overlap is calculated. The same upper x-axis, $\Delta\beta_{LP01}$, is repeated for Fig. 3.9(a-c) to emphasize that they share the same range of data. In Fig. 3.9(a) the coefficient of coupling to the fundamental cladding tube mode, η_{LP01}, also exhibits a Lorentzian-like behaviour centred at $\Delta\beta = 0$ where each core mode has a maximum value of η that falls off sharply as $|\Delta\beta|$ increases. This can be understood by considering that core modes become strongly hybridised with cladding modes near phase matching and therefore the electric field overlap with a pure tube mode increases as described by Eq. (3.7).

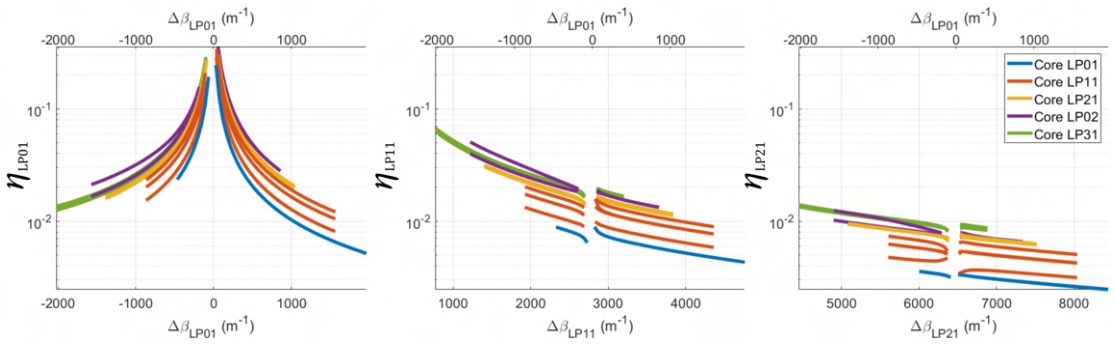

FIGURE 3.9: The overlap integral, Eq. (3.7), between several core modes (line colour) and (a) the LP_{01} cladding tube mode, (b) the LP_{11} cladding tube mode and (c) the LP_{21} cladding tube mode. These values are plotted against the difference in propagation constant between the given core mode and the specified cladding tube mode.

For the geometry and cladding refractive index range considered, the core modes plotted here are far from phase matching to higher-order cladding tube modes (see Fig. 3.8(a)). When the overlap integral to these tube modes is calculated, therefore, $|\Delta\beta|$ is large and Fig. 3.9(b,c) show the tails of a Lorentzian curve.

For all tube modes the magnitude of the overlap integral increases with the core mode order. In Fig. 3.9(b), the overlap integral of the LP_{02} core mode is roughly double that of the fundamental LP_{01} core mode at $\Delta\beta_{LP11} = 3000$. Considering Eq. (3.4), this result goes some way to explain the large differential loss between core modes even when both are in the first phase-mismatch window which has the lowest loss (see Fig. 3.8(c)).

Seeking to quantify the loss of the core modes, it is found, as in [111], that the loss of core modes can be well approximated by a modified version of Eq. (3.5), that is:

$$\alpha_m^{core} \approx \sum_k \frac{\gamma_k |\eta_{m,k}(\Delta\beta_{m,k})|^2}{\delta^2 + (\Delta\beta_{m,k})^2} \tag{3.9}$$

where δ is introduced to account for the finite loss when $\Delta\beta = 0$ and the dependence of the coupling strength on $\Delta\beta$ has been made explicit.

Fitting Eq. (3.9) to the simulation data, there is indeed good agreement. In Fig. 3.10 the predicted loss from this simple coupling model is compared with the results of numerical simulations for two core modes: LP_{01} in (a,b,c) and LP_{21} in (d,e,f). Initially, in Fig. 3.10(a) and Fig. 3.10(d) only the contribution from coupling to the fundamental LP_{01} cladding tube modes are included. The low-order core modes are near the phase matching condition with the fundamental cladding tube mode, indeed the point of phase matching ($\Delta\beta_{LP01} = 0$) is contained in this data set. It can clearly be seen that this cladding mode is the most significant contributor to the loss; when considering only the fundamental cladding tube mode in Figs. 3.10(a,d) there is already some agreement to the data; in Fig. 3.10(a) near phase matching at $\Delta\beta_{LP01} = 250$ the model

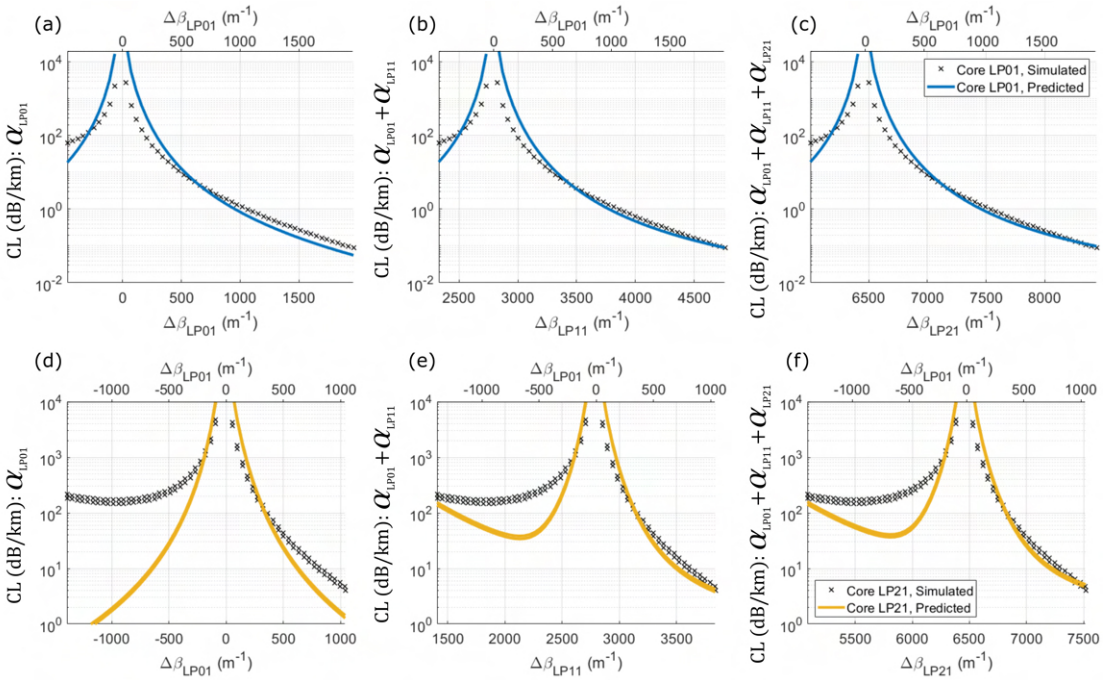

FIGURE 3.10: The confinement loss for (a,b,c) the LP_{01} core mode and (d,e,f) the LP_{21} core mode found by fitting Eq. (3.9) to the simulation data. Shown is the contribution of (a,d) the fundamental LP_{01} cladding tube mode, (b,e) the LP_{01} and LP_{11} cladding mode groups and (c,f) the LP_{01}, LP_{11} and LP_{21} cladding mode groups. Loss is plotted versus the difference in propagation constant between the core mode of interest and the specified cladding tube mode, i.e. in (b) $\Delta\beta_{LP11} = \beta_{LP01}^{\text{core}} - \beta_{LP11}^{\text{cladding}}$.

overestimates the loss of the LP_{01} core mode by factor 2x and the error is reduced for increasing $\Delta\beta_{LP01}$, moving away from resonance.

When including the contributions of all three cladding tube modes considered here (Figs. 3.10(c,f)) this model does slightly overestimate the loss very near the phase-matching point which is likely due to the approximations made by the introduction of δ in Eq. (3.9). A very localised underestimate of loss can be observed in the region at the edge of the second phase-mismatch window (e.g. $\Delta\beta_{LP21} = 5900$ in Fig. 3.10(f)). In this region, although the fit is improving as additional tube modes are considered, the model appears inadequate to describe the complex interplay between modes. Improvements could be found by considering the phase change of the tube modes in the presence of strong hybridization and due to coupling between individual tube modes.

Equation 3.9 describes a summation over all cladding modes but here the contribution of modes only up to the third, LP_{21}, cladding tube mode are included. As the contributions of additional cladding tube modes are included, the fit improves. To truly capture the loss using this model it would be required to calculate the phase mismatch and overlap with all of the cladding modes including the dielectric modes and the air modes of the inter-tube regions. There is, however, very reasonable

agreement using 3 or even only 2 cladding tube modes in the first phase-mismatch window ($\Delta\beta_{LP01} > 0$), that is where low-loss modes are typically desired to be guided.

Here the powerful concept of mode-coupling is explored for understanding and analysing the behaviour of anti-resonant fibres in the low-loss regimes in which they are typically operated. Although the concept of modifying material index explored here can be studied in practice by modifying for example the gas pressure inside the tubes [117], in a more typical deployment, controlling the phase matching condition must be achieved by controlling the difference in size between the core and cladding tubes. Without adding additional tubes and maintaining the core size, smaller tubes have wider gaps and larger air regions between them. The gap modes therefore become more significant and, in addition to the effect of coupling to tube modes one must also consider the effect of coupling to gap modes even for low-loss structures where gap modes have a lesser effect. The effect of gap modes in NANFs is increased by virtue of loss to cladding tube modes being reduced and so gap modes are expected to be more important to the analysis of NANFs.

The results shown here could be applied to a number of practical applications, for instance in designing multi-mode ARFs. Previous work has shown how the size of the core impacts the number of low-loss modes guided [49] but these studies ignored the effect of resonant out-coupling when in fact this is currently the primary method of engineering the modes of ARFs. Here, it is shown that the first phase-mismatch window is the only regime in which low-loss guidance can be achieved and that phase matching to the fundamental cladding tube mode well describes the loss of the fundamental and higher order core modes in this region. This knowledge can guide the development of a technique for designing ARF geometries which guide a desired number of modes under a loss threshold.

3.5 Conclusions

In this chapter the sources of differential modal leakage loss in multi-mode anti-resonant tubular fibre are investigated. In fibres that have small inter-tube gaps in the cladding, common in low-loss geometries, the confinement loss for core-guided modes operating in anti-resonant windows, far from resonance with dielectric modes, can be analysed and understood as the result of coupling to air-guided cladding tube modes. Air guided modes propagating in the gaps between tubes and dielectric modes in the tubes themselves on the other hand have very little impact on the loss.

A crucial quantity that drives the strength of coupling from core modes to tube modes and thus loss, is the separation between the propagation constants of the core and cladding tube modes which can be readily determined from the geometry. When exactly phase matched, core modes suffer leakage loss as high as that of the cladding

modes themselves. From the results here some useful insight are derived into the design of few-moded, multi-moded and effectively single-mode ARF; in particular the concept of phase-mismatch windows. All desired modes must be guided in the fundamental phase-mismatch window, with propagation constant greater than that of the cladding tube modes, to achieve low loss operation. In tubular fibre this might require choice of small cladding tubes which can cause high loss due to the jacket glass being closer to the core, however, geometries with nested elements such as NANFs can guide multiple low-loss modes without prohibitively high losses.

Using this understanding a model was developed to approximate leakage loss based on the concept of resonant coupling to tube modes. By considering only the contributions of the first three cladding tube modes good agreement to numerical simulation was attained. This model demonstrates that the loss of core modes is dependant on not just coupling to the fundamental cladding tube mode but also to the higher-order cladding tube modes. Future work could improve on this model by taking a similar approach to also include the impact of other cladding modes, for example those propagating in the gaps between tubes or the glass modes. The insight gained in this chapter is used in Chapter 4 to develop techniques for understanding and reducing differential modal loss in a ARFs with a variety of micro-structure cladding designs, including the NANF.

Chapter 4

Designing Few-moded Anti-resonant Fibres with Low Differential Loss

In Chapter 3 differential modal loss and the sources of loss in multi-mode ARFs were investigated. Although applicable to ARF in general, that chapter focused on tubular fibre due to the simplicity of that geometry. Of more interest are other structures, such as the NANF, DNANF and Anti-resonant Leakage Inhibited Fibre (ALIF) which are predicted [10, 85], and have been demonstrated [21, 22], to be capable of very low-loss single-mode operation compared to tubular fibres. These structures are the focus of this chapter.

Section 3.1 demonstrated that the simplest route to achieving low-loss higher-order modes is to increase the size of the core. For example, in 2019 Winter *et al.* demonstrated a 10-mode hollow-core fibre by fabricating a very large, 164 µm diameter core, tubular fibre which guided 10 modes [49]. Chapter 5 will discuss ARFs with large cores for guiding many tens of mode groups. By contrast, in this chapter, the objective is to achieve few-mode guidance, which shall be defined here as fewer than 10 guided mode groups. Towards this goal, a greater understanding of the behaviour of the cladding modes in ARF geometries of interest, which Chapter 3 demonstrates are critical for low-loss guidance, is required.

Current short-haul links, with reaches up to a few 100 metres, employ multi-mode graded-index fibres with a strict core radius specification of 25 µm and operate at a wavelength of 850 nm [118]. Short-haul is deployed extensively in data centres where the demand for higher data rates is always increasing and yet solid-core fibres are rapidly reaching the limits of what is achievable. By contrast, single-mode NANFs have been demonstrated with lower loss than solid-core fibres at 850 nm [59] and the wide bandwidth and low dispersion of ARFs suggests that they may be capable of

improving on the data-rate and link length achievable in solid-core graded-index fibre. The question of whether few-mode, hollow-core fibres can be designed with low differential loss is integral to the task of using hollow-core fibres for short-haul telecommunications. Meanwhile the fixed core size requirement provides a useful constraint to explore the techniques required to design the cladding of NANFs, ALIFs and DNANFs in order to achieve low-loss few- and multi-mode guidance.

The chapter is organised as follows. Section 4.1 presents a brief background on the current standards and requirements for short-haul, multi-mode telecomms. Section 4.2 investigates few-mode guidance in NANFs. The effects of the number of tubes and cladding parameters on loss and higher-order mode limitations is discussed. The cladding modes are studied and techniques are developed to both predict the quantitative effects of bending on HOM suppression and to design the cladding of a NANF or DNANF to optimise multi-mode guidance. Section 4.3 considers other ARF geometries with additional nested, adjacent elements. Although demonstrating very impressive confinement of HOMs, the effect of glass resonances due to additional glass nodes is found to be severely limiting and the investigation is limited to the ALIF with 2 nested, adjacent tubes. In Section 4.4 the ALIF design is investigated further. Similarly to the NANFs and DNANFs, a technique is developed to predict the effective index of the cladding modes and thereby design ALIFs for multi-mode operation. Finally, this technique is used to develop a 10-tube ALIF fibre for short-reach telecommunications, capable of double the bandwidth and significantly reduced loss compared to current standard multi-mode, graded-index fibres.

The work described in Section 4.4 has been previously been published in Ref. [119].

4.1 Short-Haul Telecommunications

As demand for internet services increases, the end-to-end transmission capacity must increase, but so too must the capacity of data centres which store, process and generate the massive amounts of data communicated. While individual links are typically only several tens of metres or at maximum a few hundred metres in length, in total there may be tens of thousands of kilometres of fibre deployed in a single data centre. For the companies running these data centres it is imperative that the links, from source to receiver, are low-cost whilst also meeting the low power and high data rates they require. For short-haul links in the region of 100 m or less a common solution is Vertical Cavity Surface Emitting Lasers(VCSELs), which are very low-cost to manufacture at scale compared to other solutions, coupled with graded index multi-mode fibres. Other short-haul deployments employ single-mode lasers to leverage the higher data-rates generally possible in single-mode fibres but lower-cost multi-mode VCSEL-based links remain wide-spread and are the target of this chapter

[120]. It is likely that single-mode ARF would prove beneficial in single-mode short-haul links as they are predicted to be in long-haul [12].

4.1.1 Vertical Cavity Surface Emitting Lasers

VCSELs are a type of semiconductor diode laser unique in that emission is perpendicular to the top or bottom surface, rather than a cleaved edge as in edge emitting diode lasers. The key advantage of this is that the laser is functional on the slab upon which it is manufactured. They can be tested during production allowing manufacturing defects to be caught early on. This in turn makes them very cheap to produce. It is even possible for VCSELs be deployed on the slab in large two-dimensional arrays, raising the possibility of very tightly integrated multi-laser systems for WDM, highly-parallel data transmission or high-power applications [121, 122].

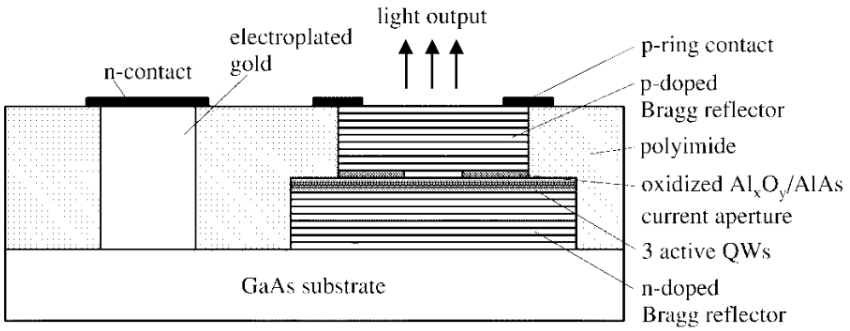

FIGURE 4.1: Cross section of a selectively oxidised VCSEL [123]. The structure is broadly that of a PN junction. The oxidized layers are insulators confining the current to the small active region formed in this instance of three quantum wells (QW).

VCSELs were first demonstrated operating at room temperature in 1988 [124]. The structure is that of a PN junction forming a diode as shown in Fig. 4.1. Reflectors on the top and bottom turn the diode into an optical resonator with the active region formed of one or more quantum wells in the middle. Due to the comparatively short active region, high reflectance is required to produce sufficient lasing. Distributed Bragg reflectors are therefore employed, producing reflectivity greater than 99%. Current is injected into the top surface and passes through to the bottom.

Due to the short cavity, the longitudinal mode spacing of a VCSEL is typically tens of nm, two orders of magnitude greater than that of an edge emitting laser. Therefore, for most applications, surface diode lasers emit a single longitudinal mode [125]. VCSELs however, typically display multiple transverse modes. The exact nature of these modes is highly dependent on the driving current and the optical feedback on the device [126]. Emitted modes are very well approximated by Laguerre-Gaussian beams

and will tend to emit at slightly different wavelengths, typically a few nm difference. As the driving current is increased the output power will shift towards the higher order modes and it is quite common in a multi-moded VCSEL for most of the output power to not be in the fundamental mode [125]. In communications, VCSELs can typically be modulated directly very effectively and up to 25 Gb/s direct modulation has been demonstrated [127].

Active diameters for the modes of telecommunication VCSELs are designed to be between 15 µm and 25 µm, similar to the core dimensions of multi-mode optical fibre allowing efficient butt coupling [128, 129]. Although VCSELs are typically fabricated in the GaAs platform which supports wavelengths from around 700 nm to 1300 nm, 850 nm is used for many purposes including telecommunications [125].

Power conversion efficiencies greater than 50% have been demonstrated since the advent of selective oxidisation [121, 130]. It follows that there is far less heat generated and VCSELs are typically operated without any cooling or heat dissipation system. It should be noted however, that despite their high efficiency and low driving currents compared to edge emitting lasers, VCSELs have not approached the maximum output power of other devices.

4.1.2 Short-Haul Fibre and Standards

Coupling a high fraction of the light emitted by a multi-mode VCSEL generally requires a multi-mode fibre. To reduce the impact of inter-modal dispersion large, 50 µm core, graded-index (GI) fibres are chosen. The Optical Multi-mode (OM) series is a collection of performance standards for multi-mode optical fibres used in short-haul telecommunications. The data rates of VCSEL/GI links are limited by the fibres' inter-modal dispersion, driven by differential group delay (DGD) between the modes. GI fibres are highly multi-mode, often guiding more than 1000 modes. The actual performance of the fibre is therefore very sensitive to the launch conditions; if most of the light couples into lower order modes then the DGD will be small but as more light propagates in higher order modes the DGD will increase. The OM standards therefore define bandwidth-distance product for a certain encircled-flux launch condition such that DGD is within tolerances and desired data rates are achievable.

OM3 fibres have a maximum DGD of the order of 0.22 ns/km [131]. The OM4 standard released in 2009 improves on the maximum data rate but further improvement is limited by the fundamental limits imposed by solid-core guidance in silica [118]. The most recent, OM5 standard from 2017, instead of further reducing the fibre dispersion expands the optical bandwidth from single-wavelength operation at 850 nm to instead covering the band 850 - 950 nm, optimizing it for shortwave WDM

	OM3 TIA 492-AAAC	OM4 TIA 492-AAAD	OM5 TIA 492-AAAE
Year	2002	2009	2016
Attenuation	2.5 dB/km	2.5 dB/km	2.5 dB/km
Bandwidth-Distance Product	1500 MHz − km	3500 MHz − km	3500 MHz − km
Wavelength Range	850 nm	850 nm	850 - 950 nm

TABLE 4.1: A summary of the laser-optimized, optical multi-mode fibre specifications for graded index fibre. The OM1 and OM2 specifications are both for light emitting diode sources and are not applicable to this work. The year is the date that the original version of the specification was published.

Standard	**Cable**	**Modulation**	**Minimum Distance**	
			OM3	**OM4**
100GBASE-SR10	2x12 / 1x24 fibre	10 x 10G, PAM2	100 m	150 m
100GBASE-SR4	1x12 fibre	4 x 25G, PAM2	70 m	100 m
100GBASE-SR2	2x2 fibre	2 x 25G, PAM4	70 m	100 m

TABLE 4.2: A summary of the 100 Gb Ethernet connection standards for short-haul optical fibre links.

applications. The usable bandwidth is again limited by the optical loss and dispersion. A summary of the pertinent data is given in Table 4.1. The OM specifications also define the fibre performance at 1310 nm; however they are optimised for 850 nm, which is the more common wavelength for short-haul telecommunications.

Current Ethernet standards achieve 100 Gb/s transmission by deploying bundles of 4 or 8 GI fibres, each carrying 50 or 25 Gb/s, up to 100 m as described in Table 4.2. Increasing the number of fibres in a cable also requires scaling of the optical switches and connectors which generally must occupy the same physical footprint [120]. Emerging requirements for 200 and 400 Gb/s Ethernet require a new approach to achieve the required bandwidth over usable distances and without an excessive and unsustainable (in terms of expense and practicality) increase in the already substantial hardware infrastructure. Hollow-core anti-resonant fibres suggest a route for meeting future demands on data rate in multi-mode short-haul links, as they are predicted to do in single-mode long-haul links [12]. In addition to lower dispersion and nonlinearity [10] ARF has already been demonstrated with lower loss that solid-core fibres at 850 nm [59]. Furthermore, lower latency [24] and thermal sensitivity [132] may be beneficial in data-centre applications.

4.2 Few-moded guidance in NANFs

The NANF is a very well understood and proven technology for single-mode operation: multiple hollow-core low-loss records have been achieved in NANFs [21,

59, 133], hundreds of km of single-mode NANF have been produced in the lab and commercial NANF cables are already available [30]. The excellent performance demonstrated makes NANF a logical structure with which to begin the investigation. Single-mode NANF is engineered so that the cladding modes strongly couple to the LP_{11} core mode group, ensuring high loss amongst the high-order modes [77]. Chapter 3 discussed the origins of differential modal loss in ARF and demonstrated that low-loss operation demands that ARFs be designed such that the phase constant of the core modes are within a phase-mismatch window where coupling to cladding air modes is reduced. In Section 3.4.1 I demonstrated that core modes in the fundamental phase-mismatch window, with effective index greater than that of the fundamental cladding tube mode, have the lowest leakage loss.

Figure 4.2 shows examples of the modes of a NANF. The core modes, Fig. 4.2(a-d), are similar to those of a tubular fibre and are labelled in this chapter by their LP group using the notation described in Section 2.1.3. The nested capillary subdivides the tube air cavity and each region guides its own set of inner-cladding (IC) modes. The notation IC_1 is adopted to refer to modes guided inside the innermost tube, Fig. 4.2(e), and IC_2 for modes in the outer region, Fig. 4.2(f). As in tubular fibre there also exists an air cavity bounded by the jacket glass and the outer capillary tubes and the outer-cladding (OC) modes guided in this region are referred to by the notation OC_1. It is important to note that each of these cladding air cavities guide a full set of modes just as in the core region. Typically the only cladding mode of interest is the fundamental, HE_{11}-like mode (which is shown in Fig. 4.2(e-g)) that has the highest phase constant (see Eq. (3.6)). For simplicity, therefore, IC_n and OC_1 shall henceforth refer to the fundamental mode group of the respective set and where necessary specific mode groups shall be referred to by e.g. IC_1-LP_{11}.

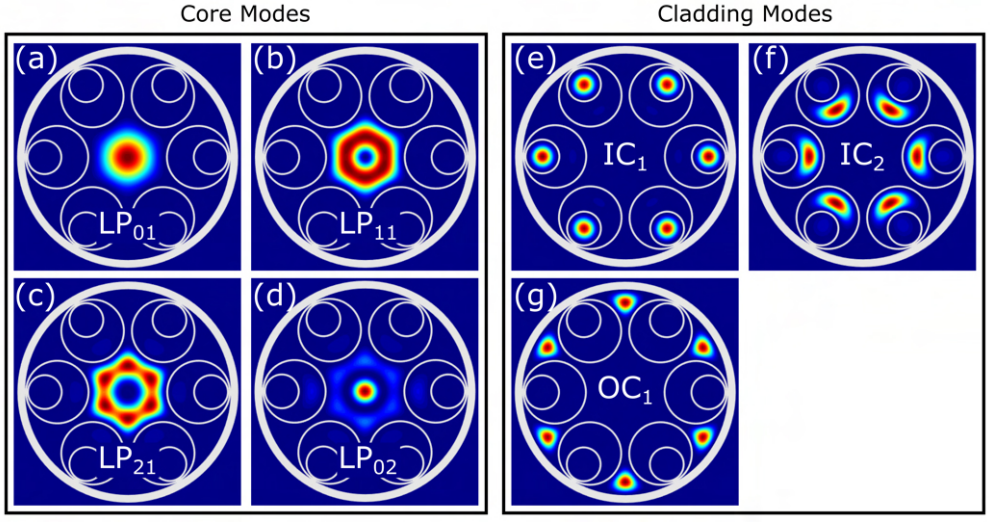

FIGURE 4.2: Mode profiles of the first few modes in the core (a-d) and cladding (e-g) of a NANF found by numerical simulation.

Increasing the size of the core reduces leakage loss (Eq. (3.1)) and raises the effective index of core modes (Eq. (3.6)) causing more modes to be guided in the fundamental phase-mismatch window. In this chapter, however, a fixed core size of 25 µm is targeted and of interest is the design of the cladding and the modes guided therein which define the phase-mismatch windows. Section 3.3.1 describes how outer-cladding modes, OC_1, are not significant for low-loss NANF designs with small inter-tube gaps (this will be elaborated on further in Section 4.2.3). The phase constant of the IC_1 and IC_2 cladding modes define the edge of the fundamental phase-mismatch window.

4.2.1 Effect of cladding design on multi-mode guidance in NANFs

A direct route to reducing the effective index of the IC_1 and IC_2 cladding modes is to increase the number of tubes in the cladding, whilst keeping constant the size of the core and of the inter-tube gap, which results in smaller outer tubes and consequently smaller air cavities in the cladding (Eq. (2.26)). This lowers the effective index of the IC_1 and IC_2 cladding modes. Several NANF designs with core radius $R = 25\,\mu m$, gap $d = 5\,\mu m$ and a number of outer tubes between 6 and 12, have been numerically simulated. A tube thickness of 330 nm is selected such that the operational wavelength, 850 nm, is near the low-loss point of the fundamental anti-resonant window. This corresponds to a normalized frequency, $F = 0.82$ (Eq. (2.25)). Figure 4.3 shows the modal loss of a selection of these structures, including leakage and SSL, calculated using the techniques described in Section 2.3.4. For each number of tubes, several different nested tube ratios (Z_1/R) were simulated and in Fig. 4.3 the best performing designs are shown. While 6-tube NANFs are often designed to be single-mode [35, 36] the choice of nested tube ratio here results in a few-mode fibre that guides 5 mode groups with less than 10 dB/km loss. Of these 5 mode groups, the LP_{21} and LP_{02} mode groups exhibit moderate coupling to cladding modes. This is evidenced, for example, by their higher loss compared to the higher-order LP_{31} mode group; in the absence of strong coupling a higher-order mode would be expected to have higher loss (e.g. Eq. (3.1)). Increasing the number of tubes lowers the loss of HOMs that exhibited coupling to cladding modes. By moving to an 8-tube structure the loss of the LP_{02} mode group is reduced from 5.5 dB/km to less than 1 dB/km. The overall trend in loss, however, is increasing with the number of tubes. The fundamental LP_{01} group scattering and leakage loss is less than 0.1 dB/km in the 6-tube structure but in the 12-tube structure this is increased to 5.5 dB/km. This is to be expected when considering that reducing the size of the outer cladding tube also decreases the separation between the core and the jacket glass, which is well known to increase leakage loss. Indeed, as the size of the cladding tubes tends towards zero the loss of the structure tends towards that of a hole-in-bulk-silica fibre with no micro-structure. Without modification of the size of the core, an increased number of

outer tubes can increase the modality of NANFs but at cost of higher loss for all modes.

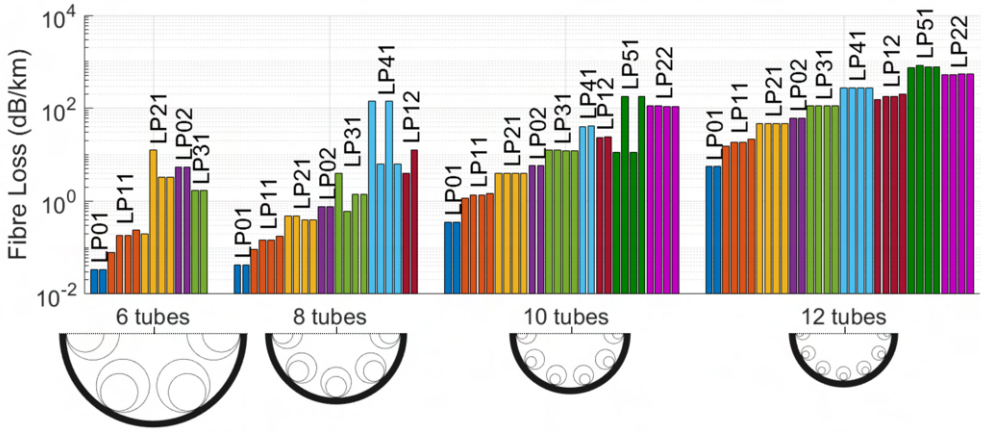

FIGURE 4.3: The modal loss at a wavelength 850 nm for a range of 25 µm core radius NANFs designed for multi-mode operation. Loss is found by numerical simulation and is considered the sum of leakage and SSL. All structures have gap $d = 5$ µm and thickness $t = 330$ nm.

It is also possible to control the IC_1 and IC_2 cladding modes by modifying the size of the nested capillary tube, and therefore the relative size of the regions in which those modes are guided. The geometric parameters which determine the size of these regions are Z_1 and Z_2 and are shown in Fig. 4.4. Figure 4.5(a) shows the modal loss of three 6-tube NANF designs characterised by the diameter of the nested capillary relative to the core radius, Z_1/R. All other geometric parameters are identical to the structures previously described therefore the size of the outer tube, R_2, is the same in each structure and the size of the outer cladding region, Z_2 decreases as Z_1 increases: $Z_2 = R_2 - 2t - Z_1$ (see Fig. 4.4).

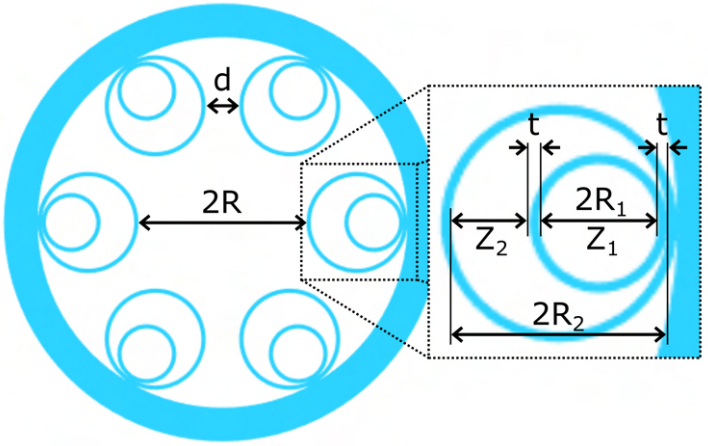

FIGURE 4.4: The geometric parameters of a NANF.

The $Z_1/R = 1.1$ design in Fig. 4.5(a) is the 6-tube NANF shown in Fig. 4.3 and guides 5 mode groups with less than 10 dB/km loss. The loss of the LP_{31}, LP_{02} and LP_{21} mode groups is increased for the designs with $Z_1/R = 1.0$ as the cladding modes are

brought closer to phase matching with those core modes. The $Z_1/R = 0.9$ design has even stronger phase matching between the the cladding modes and the core LP_{02} and LP_{31} mode groups but the LP_{21} has reduced coupling strength to cladding modes and reduced loss. The phase mismatch between the cladding modes and the core LP_{01} and LP_{11} mode groups is sufficiently large for all designs shown that there is negligible difference in the loss of those core modes.

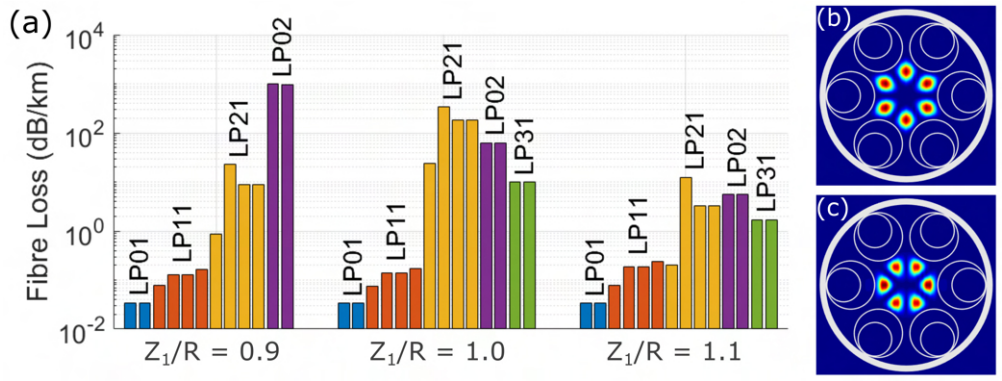

FIGURE 4.5: (a) Confinement and scattering loss at 850 nm of three 25 µm core radius NANF designs with identical outer capillary size and varying nested capillary size. All designs have gap $d = 5\,\mu$m and thickness $t = 330$ nm. Mode profiles for the (b) even and (c) odd LP_{31} modes of the $Z_1/R = 1.1$ structure.

It is of interest to note that only two of the four modes belonging to the LP_{31} group appear in Fig. 4.5(a), indicating large (> 10 dB/km) differential loss within this mode group. Figure 4.5(b-c) shows mode profiles of the even and odd LP_{31} modes respectively The two LP_{31} modes shown in Fig. 4.5(a) are the two polarizations of the even parity. The even LP_{31} in Fig. 4.5(b) has lobes at the azimuthal position of the gaps between capillary tubes and therefore can expand into them whereas the lobes of the odd LP_{31} mode in Fig. 4.5(c) are aligned with the cladding tubes. This can be understood as the effective core radius observed by the even modes being larger than that of the odd modes with the result that the even modes have increased phase constant and are no longer degenerate with the odd modes. It is expected that a smaller effective core radius would lead to higher leakage loss (e.g. Eq. (3.1)); however, in this instance more significant is the reduced phase constant which leads to stronger coupling to cladding modes. Non-degeneracy and differential loss is a general observation in ARFs common to core modes with an azimuthal index that matches the symmetry of the fibre geometry. For example in Fig. 4.3 the same effect is visible in the LP_{41} mode group of the 8-tube design and in the LP_{51} mode group of the 10-tube design.

It appears in Fig. 4.5 that the $Z_1/R = 1.1$ design has the best performance, with the lowest loss across the first 5 core mode groups. Closer examination however, reveals that only the LP_{01} and LP_{11} core modes are operating in the fundamental phase-mismatch window and higher-order core modes are in higher phase-mismatch

windows: strong coupling to cladding modes is avoided but their effective index is lower than that of the highest cladding mode, in this case the IC_1 mode. It is apparent that low-loss operation is possible in the higher phase-mismatch windows of NANFs, but this is not the case for practical fibres which will be demonstrated by considering the fibre under bending.

4.2.2 Cladding modes under bending

It is common to model an optical fibre with a constant rate of bend using a conformal mapping, described in Section 2.3.3. To first order approximation this mapping is given by Eq. (2.28) which describes a tilted refractive index distribution. Figure 4.6(a) overlays the geometry of a 6-tube NANF with an indicative plot of the refractive index of air for a fibre bent around the y-axis. The average refractive index of air inside the core region is the same in the bent and straight fibre and the effective index of modes propagating inside the core is unchanged except for extreme bends. Each air region however will in general have a unique refractive index (taken as the average across that area) and for the nested capillary this will be the refractive index at the centre of the nested tube and is given by:

$$\hat{n}_{\text{air}}^{(Z_1)} = \left[1 + \frac{(R + R_2 - Z_1/2)\cos(\phi)}{R_{\text{bend}}}\right] n_{\text{air}} \tag{4.1}$$

where R_{bend} is the radius of the bend and ϕ is the azimuthal position of the tube measured from the transverse bend axis. Clearly the maximum and minimum values of Eq. (4.1) occur for tubes with $\phi = 0$ and $\phi = \pi$, that is tubes aligned with the transverse bend axis which is the situation shown in Fig. 4.6(a). For a 6-tube fibre aligned with the transverse bend axis there are 4 unique values of $\hat{n}_{\text{air}}^{Z_1}$ which are described in Fig. 4.6 Position 1-4.

To understand the effects of bending on cladding modes the 6-tube NANF with $Z_1/R = 1.1$, described in the previous section, has been numerically simulated with a range of bend radii using the technique described in Section 2.3.3. Figure 4.6(b) shows the effective index of the most important cladding modes. The IC_1-LP_{01} modes found numerically are denoted with blue crosses and clearly shows the 4 sets of discrete, non-degenerate modes that correspond to positions 1-4. The separation in phase constant of these modes increases for smaller bend radius, as predicted by Eq. (4.1). An estimate for the phase constant of the IC_1 cladding modes is obtained by substituting Eq. (4.1) into Eq. (3.6), a technique previously employed by Frosz *et al.* [82]. The results of this model are plotted as solid lines in Fig. 4.6(b) and show excellent agreement to the results of numerical simulation.

For the geometry considered, the outermost cladding tube air region, Z_2, is small compared to other cladding air regions and the next most significant cladding mode

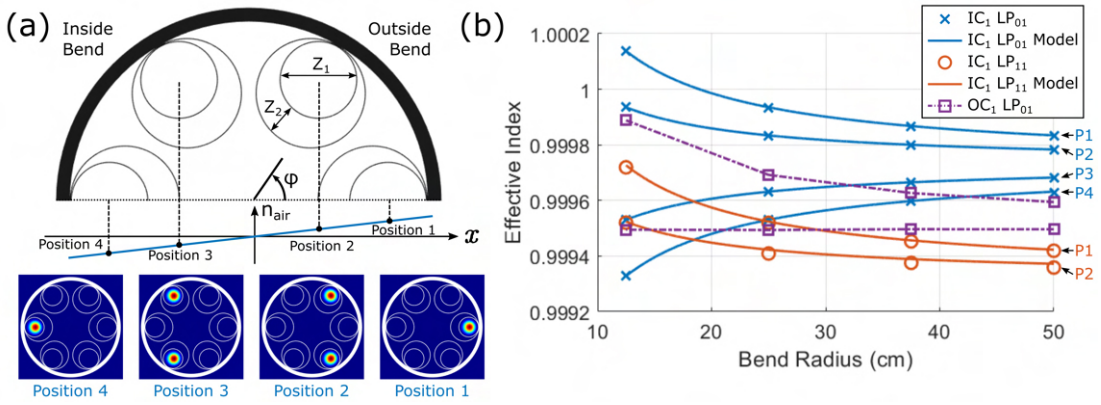

FIGURE 4.6: (a) The cross section of a bent NANF superimposed with an indicative plot of the refractive index according to the conformal map technique, Eq. (2.28). The insets show the mode fields of the IC_1 cladding mode guided in each unique tube position. (b) The effective index of the IC_1-LP_{01}, OC_1 and IC_1-LP_{11} cladding modes of a 6-tube NANF as a function of bend radius. Markers and dot-dashed lined denote the results of numerical simulation and solid lines are the predictions of the model described in the text. "Position i" is abbreviated as "P i"

(with highest effective index) is the fundamental OC_1 mode; these modes are plotted in Fig. 4.6(b) with purple squares. Again, since a pair of tubes is aligned with the transverse bend axis, there are 3 unique positions for this mode to propagate. The phase constant of the mode on the outside of the bend increases with smaller bend radius. The average refractive index of the centre gap region is unchanged with bending and so the mode guided in this region is approximately unchanged in phase constant with bending. The mode on the inside of the bend has not been found in the numerical simulation and so is not plotted but is expected to decrease in phase constant with smaller bends, mirroring the effect of the OC_1 mode on the outside of the bend. This mode could have been found numerically if more solutions were searched for but this becomes increasingly computationally expensive. Note that no analytical model exists for the phase constant of the OC_1 modes (this is discussed in Section 4.2.3) and in Fig. 4.6(b) the numerical solutions are joined with straight, dot-dash lines. The next most significant cladding modes are the IC_1-LP_{11} mode. As with the IC_1-LP_{01} set of modes, there are four unique positions. In numerical simulation however, only two of these were found for the same reasons as the OC_1 set. The IC_1-LP_{11} modes are plotted with red circles. The results of the model using Eq. (4.1) are plotted in solid red lines and once again show excellent agreement with numerical simulation.

Numerical simulation is a very useful tool for understanding the response of cladding modes to bending. In this instance, however, it does not provide a realistic indication of the fibre behaviour. Practically, a deployed fibre will experience some twist and therefore the alignment of tubes relative to the bend axis will generally be random. Also to consider are: the effects of variable bend radius along the length of a deployed fibre, slight geometric variation between tubes in fabricated fibre and the formation of

super-modes between similar cladding modes [134]. The result will be that cladding modes occupy a continuous range of effective indices, here referred to as bands, rather than discrete modes. The edges of these bands can be approximated by taking the minimum and maximum values of Eq. (4.1) ($\phi = 0$ and $\phi = \pi$) over a range of bend radius between straight and the minimum bend applicable to the application in which the fibre is to be employed. In Fig. 4.7 the edges of the cladding bands for the IC_1-LP_{01}, OC_1 and IC_1-LP_{11} are taken from the results of the numerical simulation and the effective index of the first 5 core modes are overlaid. For the straight fibre ($R_{\text{bend}} = \infty$) the LP_{01} and LP_{11} mode groups are guided in the fundamental phase-mismatch window whilst the LP_{21}, LP_{02} and even LP_{31} modes are guided in the second window. As shown in Fig. 4.5 these modes have less than 10 dB/km loss when straight. As the fibre is bent however, the size of the cladding bands increases, shrinking the phase-mismatch windows. This occurs much more rapidly for higher order windows which are bounded by multiple cladding modes. For a bend radius, $R_{\text{bend}} = 50$ cm, all the core modes previously in the second window are within the cladding mode bands and can be expected to demonstrate strong coupling to cladding modes and high loss in a practical deployment. For the same bend, the LP_{11} mode in the fundamental window is on the edge of the IC_1 cladding band and demonstrates increased loss (numerical simulation predicts approximately 70x higher leakage loss compared to the straight fibre). This indicates that practically, this is only a dual-mode fibre with a minimum bend radius of more than 50 cm, which would make this NANF impractical for short-haul telecomms applications.

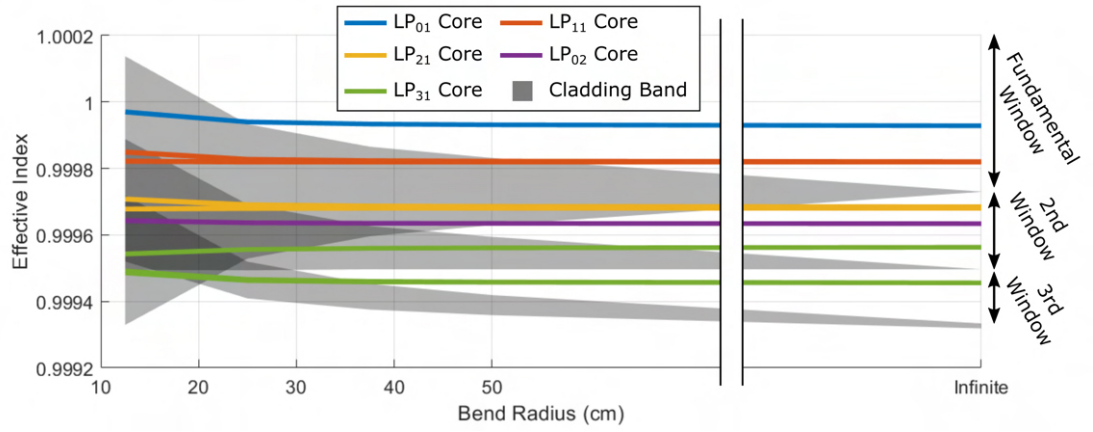

FIGURE 4.7: The effective index of the core modes of a 6-tube NANF, found by numerical simulation, as a function of bend radius. The grey blocks show the bands of cladding modes determined by the minimum and maximum effective index of cladding modes found by numerical simulation. Note that the x-axis employs a broken scale in order to compare the results of the bent fibre to those of a straight (with infinite bend radius) fibre. The limits of the first three phase-mismatch windows are indicated.

Clearly, bending has a significant impact on the behaviour of cladding modes which must be taken into account when designing multi-mode ARFs. This, for example, precludes the possibility in practical fibres of guiding core modes in higher-order

phase-mismatch windows, with lower effective index than the fundamental cladding tube modes, even when numerical simulation indicates low-loss behaviour since once bent these modes would suffer dramatic loss increases. This also suggests a convenient method of understanding and quantifying the increased leakage loss when bending: the effect of reduced phase-mismatch with cladding modes and therefore stronger coupling between core and cladding modes. This is similar to the models described for straight ARF in Chapter 3. By describing the bend as a conformal map of refractive index, the phase constants of the IC_1 cladding modes can be well predicted from the geometry of the fibre and this is an effective technique for predicting the bend resilience of multi-mode ARFs which is used in Chapter 5 to design ARF for specific applications.

4.2.3 Engineering NANF and DNANF cladding

Engineering the phase constant of cladding modes is crucial to avoiding phase matching to core modes. In this section a simple technique is investigated to design the cladding of tubular fibres such that all cladding modes guided within the tubes have approximately equal phase constant. Due to the similarity of the structures this technique is applicable to a NANF with one nested tube or a DNANF with two nested tubes.

The cladding of a DNANF is shown in Fig. 4.8(a) which is defined by the width of each air cavity in the radial direction, Z_i. The most nested tube, $i = 1$, has Z_1 equal to the inner diameter of that tube. It can be observed in both NANFs and DNANFs that the mode field of the outer cladding-tube modes is locally confined to a region of the cavity most proximal to the core (see for example Fig. 4.2(f)). This region can be approximated with simple primitives as an ellipse, as in Fig. 4.8(b). The diameter along the minor axis is the radial width of the region, Z_i and the diameter of the major axis is chosen such that the apogee of the curve touches the containing tube. I propose that if the area of these primitives are equal then the phase constants of the modes guided within will be approximately equal. This situation is shown in Fig. 4.8(b) for which the highlighted red areas have equal area. When the cladding modes are near phase matching, their effective index is minimised which strongly reduces phase matching to core modes and maximises potential for multi-mode guidance.

The radial cladding cavity widths are defined relative to the size of the innermost tube: $Z_i = x_i Z_1$ with x_i the ratio of the i^{th} region. In this way the analysis is approximately independent of the absolute dimensions of the cladding. With the above definitions it can be shown that the equal area requirement is met when the following equation is satisfied:

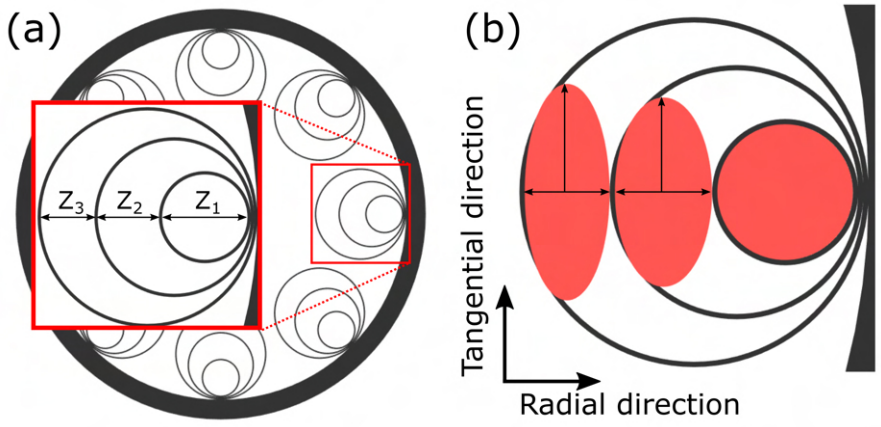

FIGURE 4.8: (a) The geometric parameters of the cladding of a DNANF, the same notation is used for a NANF with the Z_3 region omitted. (b) The approximate air regions in which the cladding modes of NANFs and DNANFs are guided.

$$x_i^4 + 4\left(\frac{t + R_{i-1}}{Z_1}\right)x_i^3 - 1 = 0 \quad \text{for} \quad i = 2, 3, ..., n \tag{4.2}$$
$$R_1 = \frac{Z_1}{2} \quad R_i = \frac{Z_i}{2} + t + R_{i-1}$$

Equation (4.2) can be solved sequentially for increasing values of i and generally depends on the thickness of the capillary walls t and thereby on the operating wavelength of the fibre. The wall thickness, however, is typically small compared to the size of the air cavities and under the assumption $Z_1 \gg t$, Eq. (4.2) has a single real, positive solution for each value of i. For a NANF $x_2 = Z_2/Z_1 \approx 0.717$. The relative sizes of the two nested capillaries in a DNANF are identical to those of a NANF, $x_2 \approx 0.717$, and the outer tube is described by $x_3 = Z_3/Z_1 \approx 0.627$. The relative radial width of air cavities, x_i, decreases for increasing i as the modes are less confined in the tangential direction by the larger tubes.

To test the efficacy of this technique a range of DNANFs were simulated where the dimensions of the cladding satisfies Eq. (4.2). The effective index of the core and cladding modes of one such 6-tube DNANF is shown in Fig. 4.9. The core radius is 32 µm and the inter-tube gap is 4 µm resulting in a nested tube radius $R_1 = 11.5$ µm. The first 5 core mode groups, up to LP_{31}, are guided in the first cladding phase window, with effective index greater than the fundamental cladding modes. The first two tube cladding modes, IC_1 and IC_2, have very similar phase constants, separated by less than 4×10^{-5} across the entirety of the wavelength range shown here. Indeed, their mode fields, shown in the inset of Fig. 4.9, indicate that the phase constants are so similar that the modes are strongly hybridised. The solutions labelled IC_1 + IC_2 are those that have a higher intensity in the innermost cladding tube and likewise the IC_2 + IC_1 labelled solutions are those with higher intensity in the Z_2 air cavity. The phase

constants of these modes is very well predicted by approximating the innermost tube as a isolated, floating capillary, as was done for tubular fibres in Eq. (3). The dotted black line in Fig. 4.9 shows the result of using Eq. (3.6) with $R = R_1 = Z_1/2$ and has excellent agreement with the numerical solutions. Although shown here for a DNANF, near identical results were observed for these two sets of modes that are present in NANF for all the NANF designs tested. The ability to easily design a NANF with strongly phase matched cladding modes and accurately predict the phase constant of those cladding modes is extremely useful and this technique is used extensively to design the cladding of multi-mode NANFs in Chapter 5.

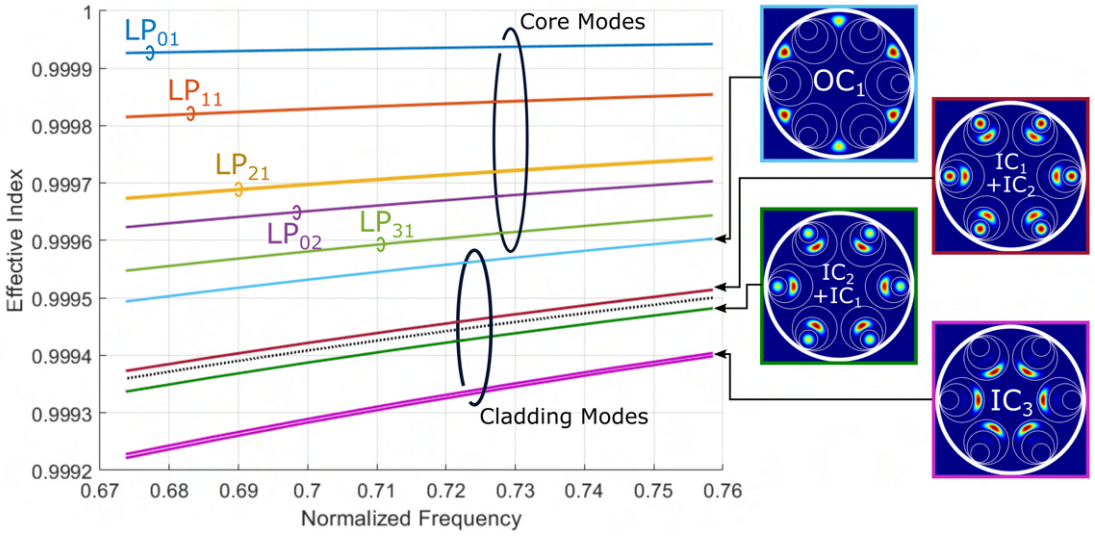

FIGURE 4.9: The effective index of several core and cladding modes of a 6-tube DNANF which has been designed to match the effective index of the tube cladding modes together. Solid, coloured lines are the results of numerical simulation. The insets show the mode fields of the cladding modes. The predicted effective index of the IC_1 according to Eq. (3.6) is plotted with a dotted, black line.

When considering the additional IC_3 mode in the Z_3 region of a DNANF, the phase matching is not as strong as for the other cladding modes and the separation of phase constant is approximately 1×10^{-4} although visual inspection of the mode field shown in the inset of Fig. 4.9 indicates a degree of very weak hybridisation with the IC_2 cladding mode. When designed using our technique the IC_1 and IC_2 modes have larger phase constants and therefore the IC_3 mode does not limit the multi-mode guidance of the fibre, indeed due to the closer proximity to the core and consequently greater field overlap with core modes it may be beneficial to have a greater separation in phase constant (see Section 3.2). The work presented here as well as additional simulations undertaken suggest that Eq. (4.2) is effective at designing the cladding of multi-mode NANFs. In multi-mode DNANFs, whilst further improvement is possible, Eq. (4.2) is useful for designing and predicting the cladding tube modes, although other cladding modes must be taken into consideration. This is discussed next.

Although inconsequential in low-loss NANFs, the cladding mode propagating in the air cavity between capillaries and the jacket, OC_1, typically becomes significant in multi-mode DNANFs. In Fig. 4.9 the OC_1 mode is the closest to phase matching to core modes and the phase constant is more than 1×10^{-4} higher than any of the tube cladding modes. To understand this behaviour, the area in which the mode is confined is once again considered. In Fig. 4.10(a) a circle is defined, the perimeter of which touches the inner jacket wall and the outer wall of the capillaries. The diameter of this circle, $Z_1^{(\mathrm{gap})}$, is described by:

$$Z_1^{(\mathrm{gap})} = \frac{2\big(R^2 + 2(R_n+t)^2 + 3R(R_n+t)\big)(1-\cos(\pi/T))}{3(R_n+t) + R - \cos(\pi/T)(R+R_n+t)} \tag{4.3}$$

where R is the core radius, T is the number of outer cladding tubes and R_n is the inner radius of the outermost cladding tube as defined in Eq. (4.2). Although $Z_1^{(\mathrm{gap})}$ approximately describes the area in which the OC_1 mode field is confined, similarly to the ellipses used to approximate the IC_2 modes, $Z_1^{(\mathrm{gap})}$ with Eq. (3.6) cannot be used to accurately predict the phase constant of the OC_1 mode. For example, in the geometry of the fibre in Fig. 4.9, Z_1 and $Z_1^{(\mathrm{gap})}$ are approximately equal yet the OC_1 mode has a significantly higher phase constant, around 1×10^{-4} similar to the difference between the LP_{11} and LP_{21} core modes. This suggests that the surrounding layers of anti-resonant walls provide the OC_1 mode with an extra degree of confinement compared to the IC_1 mode. Despite this, comparing the sizes of the air regions remains a useful tool to gain insight.

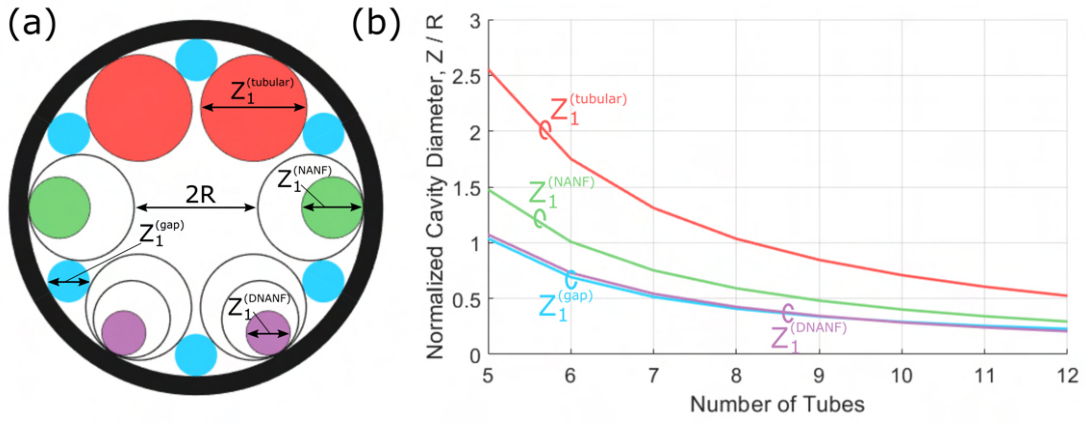

FIGURE 4.10: (a) The geometry of a tubular, NANF and DNANF fibre, superimposed together. The coloured circles denote the significant cladding air regions, under the model described in the text, for (red) the tubular, (green) the NANF, (purple) the DNANF and (blue) all structures. (b) The size of the significant cladding air regions for different number of tubes, relative to the core radius, assuming the tube ratios described by the model in the text.

When Eq. (4.2) is applied, the cladding tube modes are approximately phase matched and can be described using the air Z_1 region. The other potentially significant air regions are described by $Z_1^{(\mathrm{gap})}$. Figure 4.10(b) shows the sizes of these cavities relative

to the core radius in tubular, NANF and DNANF geometries as the number of tubes is varied and the core kept constant. Clearly, moving to NANF and DNANF structures brings significant reductions in the cavity sizes: $Z_1^{(\mathrm{DNANF})} \approx Z_1^{(\mathrm{tubular})}/(1+x_2+x_3) = 0.43 \cdot Z_1^{(\mathrm{tubular})}$. However, this also makes the size of the air cavity between tubes, $Z_1^{(\mathrm{gap})}$, comparable to those inside the tubes and the OC_1 cladding mode becomes significant for multi-mode guidance as observed in Fig. 4.9. Figure 4.10 demonstrates that increasing the number of outer tubes, T, can effectively reduce the size of these air gaps: $Z_1^{(\mathrm{gap})}$ is reduced by a factor of 3.5x in a 12 tube DNANF compared to 6 tubes. Without increasing the size of the core however, this results in the jacket being closer to the core. For the same comparison the jacket is 5x closer to the core, which will increase leakage loss. It should also be noted that this does not change the relationship between the size of the air cavities in and outside the cladding tubes, with $Z_1^{(\mathrm{DNANF})}$ demonstrating a commensurate decrease. The size of $Z_1^{(\mathrm{gap})}$, relative to the core, is insensitive to the absolute dimensions of the core and the inter-tube gap distance, d. For large values of d however, the circle model described by Eq. (4.3) may become a poor approximation of the region in which the OC_1 mode is confined.

Whilst DNANFs are a promising geometry for low-loss operation, when used for multi-mode operation, air-guided cladding modes both inside and outside the cladding tubes must be considered. Modes inside the tubes can be well controlled by selection of the sizes of the nested tubes. There is no clear method for controlling the air modes guided in the cavities between tubes without increasing the size of the core or potentially incurring higher losses. A potential solution which is not investigated in this thesis is the addition of smaller tubes between the outer tubes which could subdivide those cavities without reducing the distance between core and jacket glass. Similar techniques have been suggested, for example to achieve better single-mode operation [135] or highly bi-refringent fibres [136], although to date no attempt to fabricate such a fibre has been reported. Such a significant modification to the fibre geometry would be a large undertaking to understand theoretically and fabricate practically. In the remainder of this chapter alternative geometries are studied based on nested tubes which are promising for multi-mode guidance.

4.3 Additional Nested Elements

The approach investigated here is to increase the number of nested elements inside the outer capillary tubes. Intuitively this allows the size of the air cavities in the cladding to be subdivided into more, smaller areas which can be controlled by both the size and position of the nested element. For example a DNANF has each outer-tube divided into three air regions whereas a structure with 2 nested adjacent elements has up to 4 significant air regions in each outer tube: inside each nested element and the outer

region divided by the small gap between the nested tubes. More attention is given to the cladding modes in such a structure in Section 4.4.1. In this section the focus is on the general properties of geometries with multiple adjacent nested tubes.

The structure with two nested elements is an ALIF which has been studied by Jasion *et al.* [85]. Single-mode ALIF designs have been shown to achieve over two orders of magnitude reduction in confinement loss versus NANFs [85]. The 3-nested structure has also already been studied in detail by Habib *et al.* where, again, leakage loss was shown to be reduced by roughly 2 orders of magnitude compared to a similar single-mode NANF [137]. In studying the 3-nested structure, however, it was found that achieving a large HOM extinction ratio required sacrificing the low-loss of the fundamental mode. This suggests that these structures are promising for low-loss multi-mode operation.

The investigation begins by considering adding additional nested elements into the cladding tubes. For this initial speculative study, a smaller core radius of 13 µm was chosen to reduce the computational time required to complete simulations. The wall thickness is chosen to be 300 nm for which an 850 nm operating wavelength corresponds to a normalized frequency, $F = 0.74$. The size of the inter-tube gap is 2 µm. The insets of Fig. 4.11 shows the geometries of 6-tube fibres with 2, 3, 4 and 5 nested tubes. The nested tubes are located at equally spaced positions around the inner circumference of the outer tube and alignment is such that the tubes are symmetric about a radial line from the core whilst ensuring the weld points between outer and nested tubes are as far removed from the core as possible.

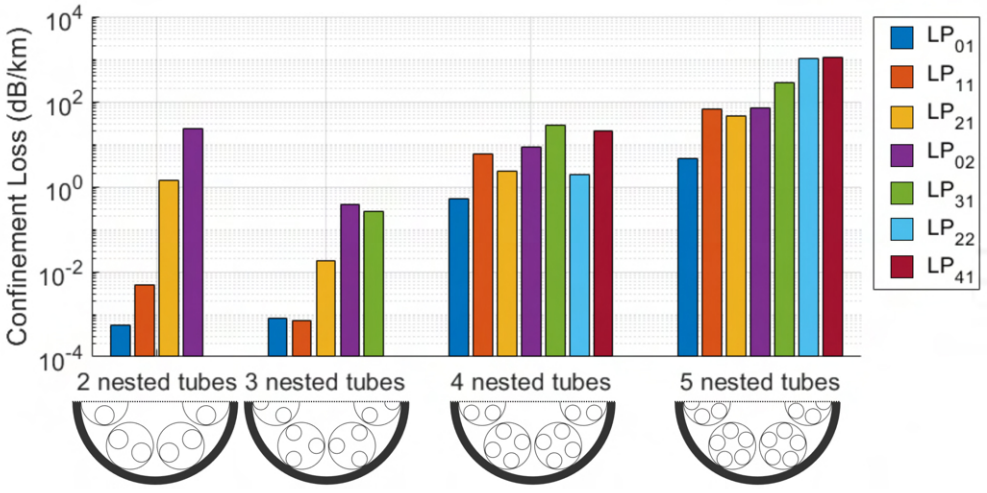

FIGURE 4.11: The modal confinement loss at 850 nm of 6-tube fibres with between 2 and 5 nested elements equally spaced around the outer tube. The insets below the labels show the simulated geometries.

Figure 4.11 shows the leakage loss of the described multiple-nested geometries at a wavelength of 850 nm. For simplicity the average loss across each mode group is shown. Despite the smaller core size compared to the NANF designs discussed in the

previous section, the 2-nested and 3-nested structures here have substantially reduced loss in the fundamental and HOMs; the leakage loss of the fundamental is more than halved in both designs and the 3-nested structure guides 5 mode groups with less than 1 dB/km leakage loss. As additional nested elements are added, however, whilst the loss of higher-order modes is reduced and more modes are guided low-loss, the loss of lower-order modes is increased. The 4-nested structure guides 7 mode groups with less than 30 dB/km leakage loss. In both the 4-nested and 5-nested structures the higher-order modes are limited by coupling to OC_1 cladding mode, with core modes above the LP_{31} mode guided in the second phase-mismatch window. If these fibres were to be considered practically for multi-mode operation, they should be designed with more outer tubes as discussed in Section 4.2.3. The high leakage loss in low-order modes however, makes this unappealing. The increased leakage loss in low-order modes is next explained by examining the loss across wavelength.

Figure 4.12(a-c) shows the modal loss of the 2-nested, 3-nested and 4-nested structures as a function of wavelength in the fundamental anti-resonant window. For the 2-nested structure in Fig. 4.12(a) the loss spectrum is relatively flat; on the short wavelength edge there is a slight increase in loss as the edge of the anti-resonant window is approached; less than 0.02 dB/km additional leakage loss at 750 nm compared to 850 nm for the LP_{11} mode group. At longer wavelengths of the 2-nested structure there are small peaks, for example at 905 nm and 930 nm in the LP_{11} mode group. They are small in magnitude however: the worst example incurs an additional 0.03 dB/km loss. The cause of these spurious peaks is the glass nodes that occur where nested elements attach to capillaries or capillaries attach to the outer jacket, a well documented effect [10, 85].

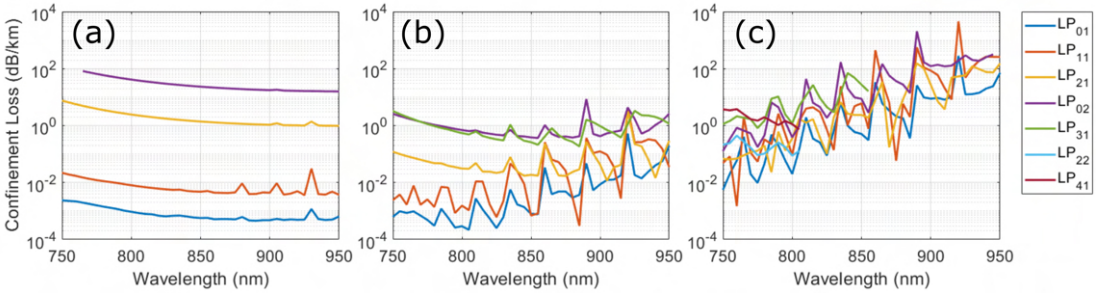

FIGURE 4.12: The leakage loss as a function of wavelength for 6-tube fibres with (a) 2-nested tubes (an ALIF), (b) 3-nested tubes and (c) 4-nested tubes.

As more nodes are introduced and they are brought closer to the core the effect of glass nodes becomes more pronounced. In the 3-nested structure in Fig. 4.12(b) they are visible in the LP_{01} and LP_{11} mode group across the entire simulated spectrum from 750 nm to 950 nm. For additional nested elements, such as the 4-nested structure of Fig. 4.12(c), these peaks are the dominant loss contribution and appear to increase the leakage loss by multiple orders of magnitude. Practically, these nodes have been found to be problematic in ARFs design based on Kagomé lattice [68] or tubular

designs with touching capillaries [71] but are largely eliminated in most NANFs. During fabrication, nodes will grow due to surface tension to be even larger than the ideal case in these simulations. This effect can, to some extent, be included in simulation but their behaviour is highly dependent on the exact geometry and dimensions fabricated and beyond predicting their presence it is very difficult to manage. The deleterious effects of glass nodes tend to be worse in fabricated fibres than simulations would predict and without eliminating the glass nodes there is no effective way to mitigate the additional glass resonances.

Tubular fibre with 2 or more adjacent, nested elements are promising options for multi-mode guidance due to their increased confinement and, intuitively, the potential for greater control of the cladding air regions, compared to a NANF or DNANF. The problem of glass resonances due to increased glass nodes close to the core unfortunately is severely limiting. For this reason, designs with 3 or more nested elements are discounted in the remainder of this thesis. Structures with 2-nested tubes, ALIFs, still demonstrate low-loss however, and are the focus of further study in the next section.

4.4 Few-mode anti-resonant leakage inhibited fibres

4.4.1 Engineering multi-mode ALIF cladding

Greater ability to predict the phase constant of the cladding modes in an ALIF without time-consuming numerical simulation would be highly beneficial to understand their behaviour and to engineer their cladding for particular requirements. The modes guided within the nested tube, IC_1, behave very similarly to those of a NANF or tubular fibre as does the mode in the interstitial gap between outer tubes, OC_1. The mode propagating in the air region of the outer cladding tube, however, is unlike other modes previously considered. Despite the different behaviour this mode propagates in the same region as the IC_2 cladding mode of a NANF and the same notation is adopted. This section investigates techniques that can be used to engineer the cladding modes of an ALIF, similar to those for NANFs and DNANFs presented in Section 4.2.3.

Figure 4.13(a) shows the geometric parameters that describe the cladding. As in a NANF, Z_1 describes the inner diameter of the nested capillary whilst the radius of the outer capillary is given by R_2. The position of the nested tubes are determined by the minimum separation, or gap, between them, d_2, with the assumption that each outer capillary is symmetric about a radial line from the core. Under this definition the greatest separation between the core and nested tubes occurs for $d_2 = 0$, which describes touching nested tubes. The maximum value of nested-tube gap,

$d_2 = 2(R_2 - Z_2 - 2t)$, occurs when the nested tubes are equidistant between the core and the jacket. In this work the situation of nested tubes closer to the core than the jacket is ignored since this would result in equally sized air cavities but reduce the separation between the glass nodes (at the weld points between the nested and outer capillaries) and the core modes.

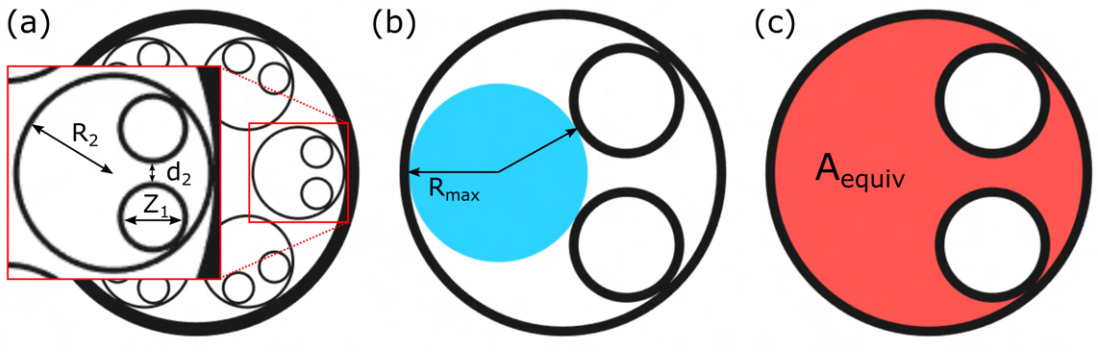

FIGURE 4.13: (a) The geometric parameters of the cladding of an ALIF. (b) The maximum circle which can fit in the outer cladding region which touches the inner circumference of the outer tube and the outer circumference of the inner tubes. (c) The area of the outer cladding region which is considered in the equivalent area model described in the text.

It can be observed that the mode field of the IC_2 mode of an ALIF is bounded in a specific area of the air cavity and a simple primitive can be determined to approximate this area. This is similar to the technique used to determine the IC_2 of a NANF in Section 4.2.3. Figure 4.13(b) shows a circle bounded by the inner circumference of the outer capillary and the outer circumference of the nested capillaries. This is the largest circle that can fit completely inside this air cavity and so the model based on this is denoted "maximum circle". The radius of this maximum circle can be determined from the geometry of the cladding as:

$$R_{\max} = \frac{R_2^2 + 2R_2 p\cos(v) + p^2 - (t + R_1)^2}{2(R_1 + t + R_2 + p\cos(v))} \tag{4.4}$$

$$\text{using} \quad p = R_2 - t - R_1 \quad \text{and} \quad \cos(v) = \sqrt{1 - \left(\frac{Z_1 + 2t + d_2}{2p}\right)^2}$$

By approximating the cavity as a circular region in which the IC_2 mode is guided an estimate for the phase constant of the mode is obtained by using e.g. Eq. (3.6). A comparison with the results of numerical simulation will be used to improve the accuracy of the model. A simulation of a full ALIF structure is computationally expensive compared to that of a tubular or NANF fibre as more mesh elements are required in the more complex cladding micro-structure to produce a mesh that can accurately describe the solution. In addition, a greater variety of cladding modes leads to more discrete solutions within the bands of cladding modes. Generally, therefore, more solutions must be solved in finite-element simulation to obtain information

about the cladding modes of interest and this also increases computation time and requires additional time to identify and label solutions. The approach employed here to mitigate these problems and enable detailed simulation of cladding modes in a wide variety of ALIF geometries is to simulate the ALIF cladding structure in isolation. The simulated geometry is an isolated outer capillary with nested capillaries (e.g. Fig. 4.13(b)) without jacket glass and surrounded by infinite air (achieved by the use of a suitable PML, see Section 2.3.2). Clearly, this is an approximation which discounts the impact of the jacket glass and the aforementioned interaction between the modes of different capillaries [134]. The same approximation, however, is used in Eq. (3.6) (which describes the effective index of a floating, isolated capillary [115]) and therefore for determining the IC_1 and IC_2 modes of a NANF in Section 4.2.3. In that section, excellent agreement to the results of numerical simulation of the full structure was demonstrated.

The capillaries of a wide variety of ALIF geometries have been numerically simulated. Figure 4.14 shows the phase constant of the IC_2 ALIF mode as a function of the normalized nested gap, d_2/R_2, for an outer capillary radius, $R_2 = 17\,\mu\text{m}$ and normalized nested tube diameter, $Z_1/R_2 = 0.7$. The wavelength is 850 nm and the capillary wall thickness is 330 nm, a normalized frequency of $F = 0.82$. The solutions plotted in Fig. 4.14 are for the fundamental, HE_{11}-like (LP_{01} group) for which there are two polarizations that are plotted with upward- and downward-pointing triangles respectively. The two polarizations are approximately degenerate and will not affect the model. The effective index of the IC_2 is maximised for small nested-capillary gap and decreases as d_2 increases to its maximum value. The dependency is not linear, with the sensitivity to change in d_2 increasing for larger value of d_2. The effective index predicted by the maximum circle model is shown in Fig. 4.14 with a dashed line. The general trend in the numerical results described above, is well captured by the maximum circle model. The phase constant is underestimated, however, across the entire range of possible value of d_2. For near touching tubes, $d_2/R_2 = 0.03$ the maximum circle underestimates by 1×10^{-4} and near the maximum gap, $d_2/R_2 = 0.51$, the error is almost 3×10^{-4}. In the insets of Fig. 4.14 the mode fields at selected points are plotted and overlaid with the maximum circle described by Eq. (4.4). The area of the maximum circle contracts with increasing d_2 at a commensurate rate to the IC_2 mode field, yielding the same trend in phase constant. The mode field, however, is more expansive than predicted across the range which leads to the underestimate of phase constant.

To improve the estimate, a second model was developed based on the total area of the outer cladding region which is highlighted in Fig. 4.13(c). The area of this region is $A_{\text{equiv}} = \pi\left[R_2^2 - 2(Z_1/2 + t)^2\right]$ and corresponds to a circle of equivalent area with radius:

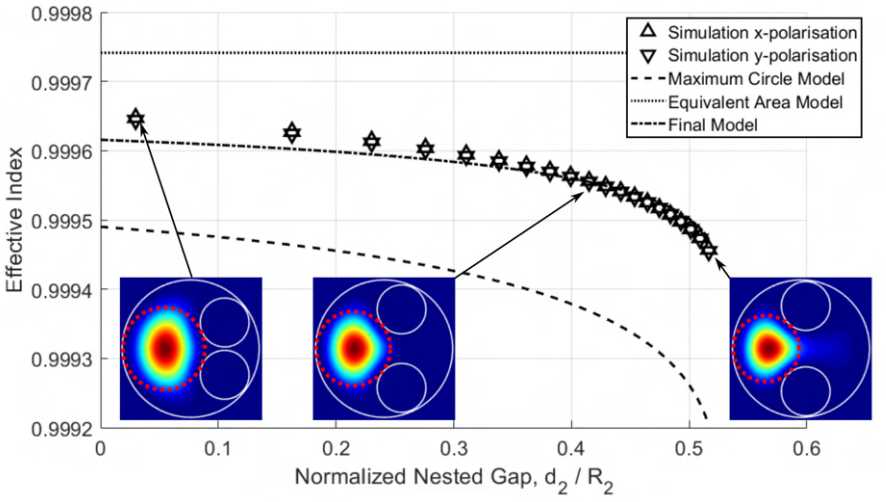

FIGURE 4.14: The effective index of the IC_2 cladding mode for different ALIF cladding designs (triangle markers) found by numerical simulation and predicted by (dashed line) the maximum-circle model, (dotted line) the equivalent area model and (dot-dash line) the final model. For each design the outer tube's inner radius is $R_2 = 17\,\mu\text{m}$. The insets show the mode field of the IC_2 cladding mode for a representative range of geometries in this figure and have the area predicted by Eq. (4.4) superimposed.

$$R_{\text{equiv}} = \sqrt{R_2^2 - 2\left(\frac{Z_1}{2} + t\right)^2} \tag{4.5}$$

which can again be used to determine an approximate effective index by substituting into e.g. Eq. (3.6). This is described as the "equivalent area" model and is shown with a dotted line in Fig. 4.14. Clearly the equivalent area does not depend on the position of the nested tubes, only their size, and therefore takes a constant value in this case. As might be expected this model over-estimates the effective index, particularly for large values of d_2 where the outer region is effectively divided in two. It does, however, incorporate the effect of the more expansive mode-field (this is made more clear in subsequent figures). The final model therefore is taken by averaging the value of the two previous maximum-circle and equivalent-area models. This final model is shown as the dot-dashed line in Fig. 4.14 and gives excellent agreement in this data set; the maximum error is less than a hundredth of a percent. Next, the accuracy is assessed more rigorously across a wider range of geometries.

In Fig. 4.15 the results of more numerical simulations, for a range of nested capillary size $Z_1/R = 0.45$ - 0.78, are shown. The simulation techniques are the same as those previously described and the numerical effective index is compared to the final model; the average effective index of the maximum-circle and equivalent-area model. For all results shown the outer capillary radius, $R_2 = 17\,\mu\text{m}$, although similar agreement is found in a range of other tube sizes. Five nested tube sizes are plotted between $Z_1/R_2 = 0.45$ and $Z_1/R_2 = 0.78$. For small nested tubes, $Z_1/R_2 < 0.61$, and nested gap size near the maximum, the final model underestimates the effective index. This

can be understood by considering the mode fields of the IC_2 shown in the insets of Fig. 4.15. For $Z_1/R_2 = 0.78$, even at the maximum gap size the mode is well confined in the region near the core and described by Eq. (4.4). As the size of the nested tube decreases, the maximum gap increases and the mode field can expand into the interstitial region between nested tubes. For the smallest nested tube here considered, $Z_1/R_2 = 0.45$, the mode field occupies the entire outer air cavity and the maximum-circle model is therefore no longer valid. The final model also underestimates the effective index for very small, near-touching nested tubes. All instances of highest error correspond to designs where the phase constant of the IC_2 is largest. These are unlikely for multi-mode guidance since the phase constant is generally desired to be reduced in order to reduce phase matching to core modes in the fundamental phase-mismatch window. Nevertheless, the largest error is of the order of 5×10^{-5} and the agreement with numerical simulation is generally significantly better.

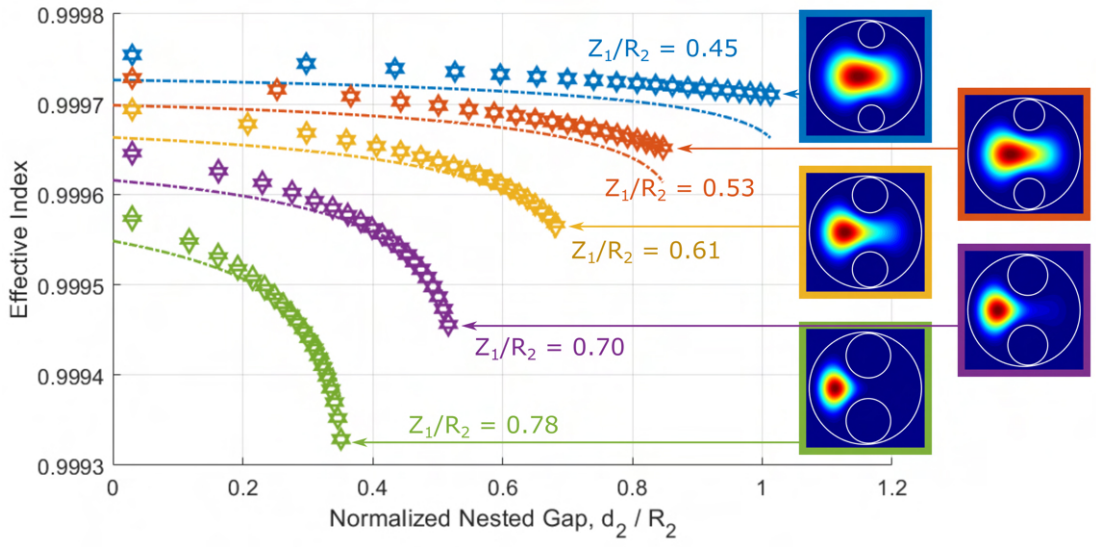

FIGURE 4.15: The effective index of the IC_{21} cladding mode for different ALIF cladding designs (triangle markers) found by numerical simulation and (dot-dash line) predicted by the final model described in the text. For each design the outer tube's inner radius is $R_2 = 17\,\mu m$. The insets show the mode field of the IC_2 cladding mode for geometries which have maximum nested-tube gap for the given size of nested tube.

The final model presented uses the geometry of the ALIF cladding tube to effectively predict the phase constant of the IC_2 cladding mode of ALIFs. There is no need for time-consuming numerical simulation and for designs of interest for multi-mode guidance excellent accuracy is achieved. The IC_2 cladding mode is predicted using the model described in this section and the IC_1 cladding mode by Eq. (3.6) with the size of the nested capillary tube, Z_1. With this knowledge designs that would incur strong coupling between desired core modes and cladding air modes can be discounted without the need for numerical simulation and methods for reducing coupling are indicated by plots such as Fig. 4.15. For example, in that plot, coupling between core

modes and the IC_2 cladding mode would be minimised for the geometry with Z_1/R_2 (green curve) but the larger nested capillary would incur stronger coupling to the IC_1 cladding mode and so geometries with smaller nested tubes are suggested to balance the effect of coupling to all the cladding tube modes. Larger gaps between the nested tubes can effectively reduce the IC_2 effective index without significant modification of the IC_1 cladding mode but this also reduces the separation between the glass nodes and the core and may lead to problematic resonances with the dielectric modes guided within, an effect that must be studied by numerical simulation. The techniques here discussed can provide insight into the behaviour of ALIFs and in the next section is used to aid the development of few-moded ALIF designs.

4.4.2 ALIF Design

To further investigate the potential for few-mode guidance in ALIFs, numerical simulations were conducted for ALIFs with between 6 and 12 tubes. To target the VCSEL-based short-haul telecomms application, the core radius is $R = 25\,\mu m$ and the wall thickness is 330 nm, which places the operating bandwidth, 850 - 950 nm, near the minimum loss point of the fundamental anti-resonant window (at 950 nm the normalized frequency, $F = 0.73$). The inter-tube gap is 2 µm and the nested tube size and position are chosen using the technique described in Section 4.4.1 to maximise multi-mode operation. Figure 4.16 shows the modal loss (here taken to be the sum of leakage and scattering losses) for the described ALIF geometries at 850 nm. The 6-tube ALIF design guides 4 mode groups, up to the LP_{02} group, below 2 dB/km. Increasing the number of tubes reduces the loss of HOMs as the phase constant of the cladding modes is reduced; the 8-tube structure guides 7 mode groups below 1 dB/km. A similar trend was observed in Fig. 4.3 for few-moded NANFs however in that instance an increase in loss of the low-order modes as the jacket glass was brought closer to the core. The additional confinement provided by the ALIF structure means that in this case the additional loss in low-order modes for additional tubes is negligible [85]. Additionally, due to the greater segmentation of the cladding region all modes shown in Fig. 4.16 are guided in the fundamental phase-mismatch window.

The trend of HOM loss reduction continues as further tubes are added. The trade-off however, was the reduction in bandwidth induced by the spurious resonances caused by glass nodes, as described in Section 4.3. Figure 4.17 shows the loss bandwidth of the first 7 mode groups of the 10-tube ALIF design. Between 850 - 1050 nm all mode groups have less than 0.6 dB/km loss and the loss spectrum is relatively flat with no spurious resonances. At shorter wavelengths loss increases as the edge of the anti-resonant window is approached. At wavelengths beyond 1100 nm there are glass resonances that cause local peaks in loss up to 1 dB/km in magnitude. In simulation the effect of glass resonances can be mitigated by moving the nodes further away from

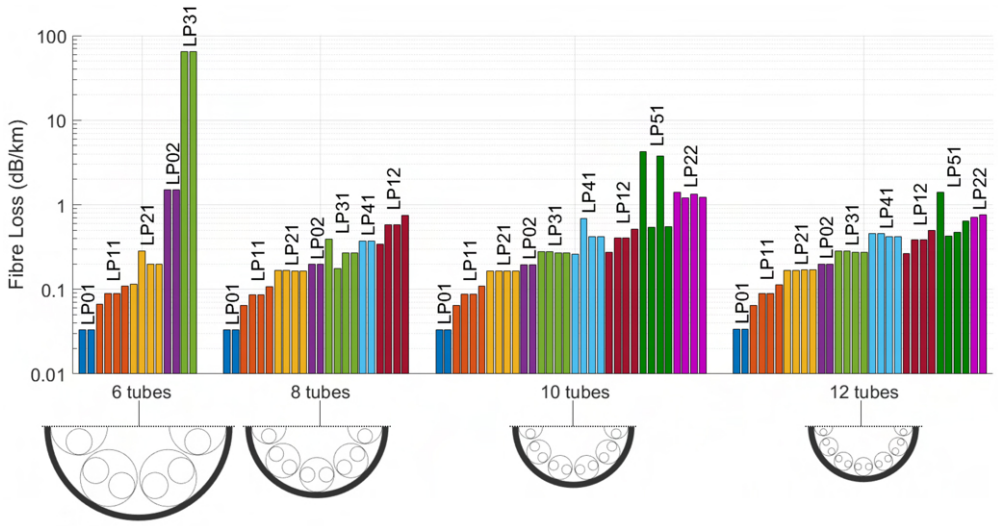

FIGURE 4.16: Losses of the core guided modes of the indicated ALIF geometries. The core diameter and tube wall thickness of each design is 50 µm and 330 nm.

the core. This strategy becomes relatively ineffective when the design featured more than 10 elements. Additionally, this will increase the phase constant of the IC_2 cladding mode (see e.g. Figure 4.15) and generally results in increased loss of HOMs as the strength of phase matching to cladding modes increases.

For the 10-element fibre, the glass resonances limit the usable bandwidth to 1050 nm. For the 12 tube fibre the effect is more pronounced and appears at shorter wavelengths. The 10-element geometry is therefore chosen as the best trade-off between few-moded operation and bandwidth. It supports 7 mode groups all with a loss (scattering + leakage) under 0.6 dB/km over a bandwidth of 200 nm. This is almost 4x lower loss that the specification of the OM standards and over twice the bandwidth of the OM5 specification. In the next section the dispersion properties of the fibre are briefly discussed.

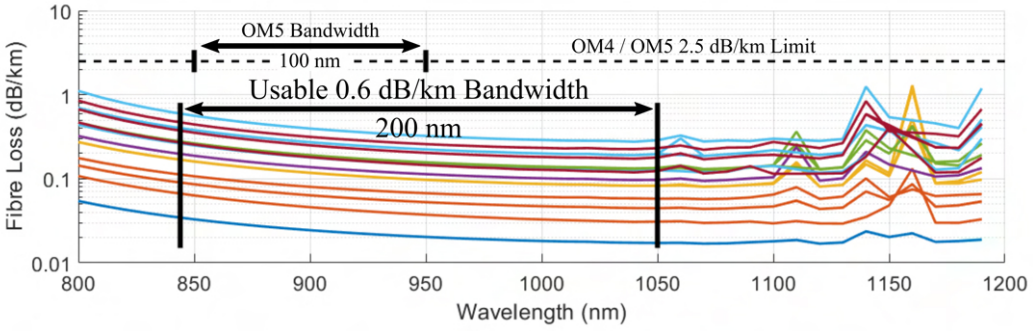

FIGURE 4.17: The modal loss spectrum, including leakage and scattering loss, of the 10-tube ALIF geometry shown in Fig. 4.16.

4.4.3 Dispersion in few-mode ALIFs

The single channel data rate in fibre links is often limited by the dispersive properties of the fibre. Single-mode ARFs offer a significant advantage over solid-core fibres in terms of latency and chromatic dispersion [24]. In multi-mode fibres however, chromatic dispersion and latency generally increase for higher order modes and the effects of inter-modal dispersion must also be considered. Indeed, this is typically the limiting factor of bandwidth-distance product in solid-core GI fibres for short-haul links.

The chromatic dispersion of the first seven mode groups of the optimised 10-tube ALIF, described in the previous section, is plotted in Fig. 4.18(a) (see Eq. (2.20)). In the low-loss bandwidth between 850 - 1050 nm, the dispersion of the fundamental mode is less than 1 ps/nm·km. Dispersion increases with mode order but all modes considered here have lower than 8 ps/nm·km across the bandwidth of interest, an order of magnitude lower than what is typical in GI fibres [138]. At shorter wavelengths the dispersion of all modes cross zero as the edge of the fundamental window is approached.

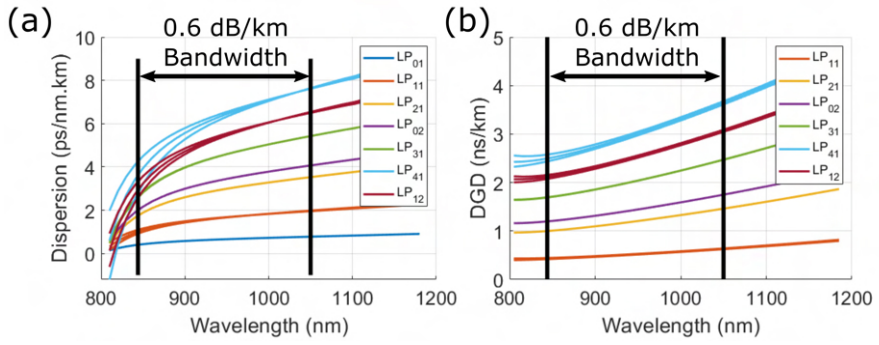

FIGURE 4.18: The (a) chromatic dispersion and (b) differential group delay of the 10 tube fibre shown in Fig. 4.16 as a function of wavelength.

Multi-mode ARFs may suffer from larger DGD than typical OM fibres. In Fig. 4.18(b) the DGD for the 10-tube ALIF design is shown. DGD is calculated as the difference in group delay (see Eq. (2.19)) between a HOM and the fundamental mode. The DGD of the fundamental mode is therefore zero by definition and is omitted from Fig. 4.18(b). As with chromatic dispersion, DGD increases with mode order. For the LP_{41} mode group, DGD is as high as 3 ns/km at 950 nm, compared to OM3 in the order of 0.22 ns/km [138]. This makes DGD a potentially limiting factor for data rate in single wavelength transmission in these hollow-core designs, if they are to be used with multi-mode sources such as the VCSEL. In Section 5.1.1 dispersion in multi-mode ARFs is investigated in more detail and strategies are tested to reduce DGD. This section is concluded with a brief discussion of the potential uses of ARF in short-haul telecomms, suggested by these results.

The large bandwidth of the ALIF design, double that of the OM5 specification, suggests that WDM can be deployed at lower single wavelength channel data rates. The impediments induced by inter-modal dispersion can be further mitigated by launching light into only a subset of the modes, a technique employed by the OM specifications in their encircled flux requirements. Digital equalisation methods exist to reverse the effects of DGD and would permit higher single wavelength channel data rates, but the computational complexity, and therefore power requirements and hardware expense, increase with higher DGD and as such may be unappealing for large scale deployment with ARFs.

A final clear approach to reducing DGD is to reduce the number of modes guided in ARF. This could result in higher single-channel data rates but may also reduce the coupling efficiency from a multi-mode VCSEL. Whilst single-mode VCSELs exist they typically have lower output power than their multi-mode counterparts [139]. Therefore in selecting the number of modes guided in the fibre there would have to be a tradeoff between the power coupled into the fibre and the single-channel data rate, limited by inter-modal dispersion. The DGD of the LP_{11} mode group in Fig. 4.18(b) is 0.5 ns/km at 950 nm suggesting a dual-mode ALIF could have as little as double the DGD of GI fibre [138]. In combination with the lower loss, wider bandwidth and other dispersion compensation techniques, few-moded ARFs could be a promising option to achieving 100 Gb/s data rates over longer distances than is possible in GI fibres. While encouraging, investigation of this option would require significant experimental work and is beyond the scope of this thesis.

4.5 Conclusions

In this chapter several ARF designs have been investigated by numerical simulation to achieve low-loss, few-moded guidance. With a fixed core size of 25 µm, to target existing multi-mode short-haul telecomms links, the behaviour and effects of different cladding designs were studied.

In NANFs, at a fixed core size, the number of guided modes can be increased by increasing the number of tubes which reduces the size of the air regions in the cladding and phase constants of the cladding modes guided within. This also reduces the separation between the jacket glass and the core, increasing the loss of all core modes. For a small number of tubes, the loss of higher order modes is limited by coupling to cladding modes. The various cladding modes in both NANFs and DNANFs were identified and studied and a technique was developed for designing the cladding of these structures to maximise multi-mode performance. This technique requires no time-consuming numerical simulation and allows the phase constants of different modes propagating in the cladding modes to be matched together and

predicted with a high degree of accuracy, greatly aiding the design of multi-mode NANFs and DNANFs. The behaviour of cladding modes in NANFs under bending was also studied. Although higher-order core-modes guided in the second phase-mismatch window can exhibit low-loss operation in a straight fibre, the effect of bending on cladding modes leads to high loss in these core modes. The insight gained may also be applied to the design of single-mode fibres.

Beyond NANFs and DNANFs, the multi-mode performance of ARF geometries based on outer tubes with 2 or more adjacent, nested capillaries was assessed. Whilst impressive HOM loss reduction was possible, the effect of additional glass nodes close to the core caused significant glass resonances which would likely make these fibres impossible to fabricate with low leakage loss practically. The structures with two nested, adjacent capillaries, the ALIF design, showed promising results and was studied in greater detail.

The unique cladding modes of an ALIF were investigated and a model was developed for predicting the effective index of these modes. As for NANFs, the ability to predict the effective index of cladding modes without time-consuming numerical simulation is very useful for designing multi-mode fibres and indeed can provide insight into improving the performance of single-mode fibres. Numerical studies show that it is possible to achieve low-loss, few-moded guidance in hollow-core fibre designs based on the ALIF. An ALIF was designed that was capable of guiding 7 mode groups, compared to the current OM5 standard for solid-core multi-mode graded-index fibres, with lower loss and over more than double the bandwidth. It is indicated, however, that DGD will strongly limit the achievable single-channel data rates. Inter-modal dispersion compensation technologies would benefit from the higher signal power arising from lower loss in ARFs and in combination with WDM could exploit their wider usable bandwidth.

In the next chapter the techniques developed here for designing the cladding of multi-mode ARFs are used to investigate more practical considerations beyond low loss in several applications that require or benefit from multi-mode operation in ARFs. Their potential in short-haul telecomms is examined in more detail by considering the dispersion of multi-mode ARFs and techniques are investigated to reduce DGD.

Chapter 5

Designing Multi-mode Anti-resonant Fibres for Practical Applications

In Chapter 3 of this thesis, the theory underlying differential modal loss in anti-resonant fibre was studied. Then, in Chapter 4, using that theory, various designs of ARF were investigated to achieve low-loss multi-mode operation. Few-mode and multi-mode ARFs can potentially be used in a wide range of applications however, for which there are many more considerations than low-loss guidance. In Chapter 4 for example, a cursory examination of inter-modal dispersion identified differential group delay between modes as a likely limiting factor for the short pulse delivery, as in telecommunications. In this chapter, the advantages and challenges of designing multi-mode ARF are investigated for a selection of the most promising applications.

The chapter is organised as follows. Section 5.1 studies the chromatic and inter-modal dispersion of MM ARF and how the geometric parameters of the fibre impacts these properties. The question of whether there is a practical method of reducing them is addressed. Both bending and twisting of the fibre is studied by numerical simulation to determine whether these techniques allow the differential group delay to be controlled. The section concludes with a discussion on the significance of the outcomes for MM ARF in short-haul telecommunications. In Section 5.2 the possibility of using MM ARF for high-power laser fibre delivery is investigated. This is an area where the solid-core delivery typically used are often multi-mode but are limited by the nonlinearity and damage threshold of silica. Hollow-core guidance is therefore a very promising alternative. Section 5.3 begins with an overview on the wide variety of uses for multi-mode ARFs in sensing applications, typically exploiting the possibility of very long gas-light interaction in low-loss hollow-core. Aside from existing applications, a novel use of MM ARF investigated here is their usage in spontaneous

Raman scattering for trace gas detection. Section 5.3 studies theoretically the possibility for markedly increased detection of Raman scattered light in multi-mode fibre and therefore increased sensitivity in such fibre sensors.

Some of the work described in Section 5.2 has been published in Ref [140].

5.1 Short haul datacomms

5.1.1 Dispersion

In the previous chapter DGD was identified as a limiting factor for the use of multi-mode ARF fibres in practical applications, particularly in short-haul datacomms. Chromatic dispersion is also increased for higher-order modes. In this section, how the geometry of a fibre affects the group delay and dispersion of high-order modes is investigated, and how they are impacted by bending and twisting.

The effective index of the modes of a hole-in-bulk-silica fibre was determined by Marcatili and Schmeltzer [18]:

$$\beta_{nm} = k_0 n_{\text{eff}}^{(nm)} = \frac{2\pi}{\lambda}\left[1 - \frac{1}{2}\left(\frac{u_{nm}\lambda}{2\pi R}\right)^2\right] \tag{5.1}$$

where λ is the wavelength and R the core radius and u_{nm} is the Bessel zero characterising the mode (see Section 3.1). This structure is not anti-resonant and therefore only approximates the behaviour of anti-resonant fibres in the centre of the anti-resonant window, away from glass resonances which do not exist in the structure described by Marcatili *et al.* By substituting Eq. (5.1) into Eq. (2.19) the group delay can be derived:

$$\frac{1}{v_g} = \frac{1}{c_0}\left[1 + \frac{1}{2}\left(\frac{u_{\text{nm}}\lambda}{2\pi R}\right)^2\right] \tag{5.2}$$

where c_0 is the vacuum speed of light. Similarly Eq. (5.2) can be substituted into Eq. (2.20) to determine the GVD:

$$D_\lambda = \frac{\lambda}{c_0}\left(\frac{u_{\text{nm}}}{2\pi R}\right)^2 \tag{5.3}$$

To test the accuracy of these equations for ARFs, numerical simulations were conducted of a range of tubular fibres. Figure 5.1 shows the modal effective index, group delay and GVD in the first anti-resonant window for two such fibres that respectively guide 5 and 13 mode groups. In Fig. 5.1(a,b) the effective index predicted

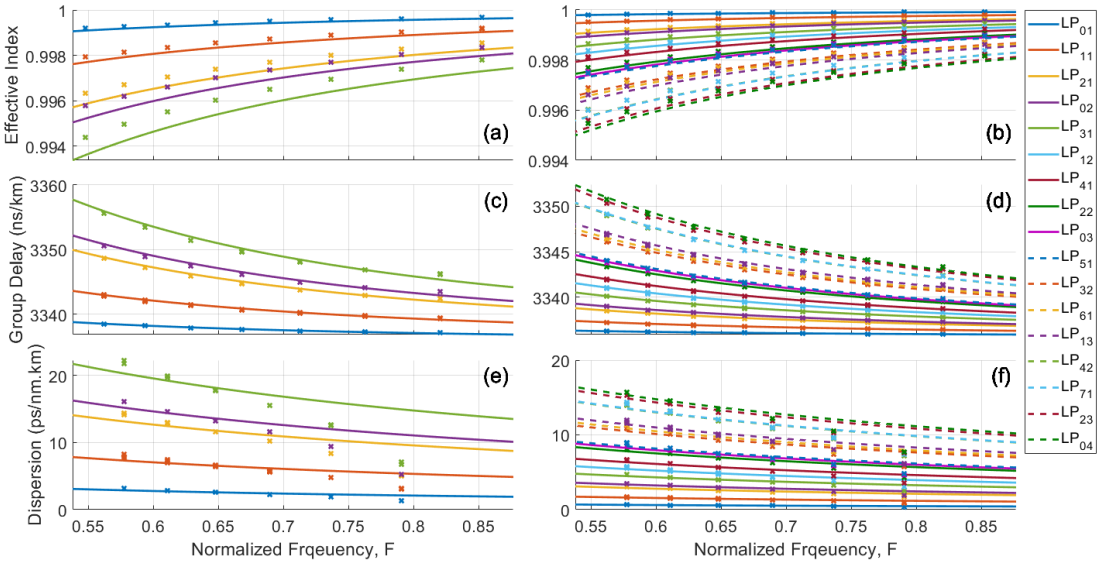

FIGURE 5.1: The (a,b) effective index, (c,d) group delay and (e,f) chromatic dispersion of two tubular fibres. In (a,c,e) the fibre has $R = 18\mu m$ and in (b,d,f) the fibre has $R = 38\mu m$. The results of numerical simulation are marked with crosses. Lines are generated with (a,b) Eq. (5.1), (c,d) Eq. (5.2) and (e,f) Eq. (5.3).

by Eq. (5.1) is always less than the true value, with error increasing with mode order. The approximation shows excellent agreement however, with error consistently within 0.1 % of the true value. The group delay calculated by Eq. (5.2) compared to the numerical values is shown in Fig. 5.1(c,d). There is excellent agreement across the wavelengths shown. The GVD is shown in Fig. 5.1(e,f). Since Eq. (5.1) does not include the effects of glass resonances, at the long wavelength edge of the anti-resonant window Eq. (5.3) underestimates the GVD. For the same reason, at the short wavelength edge there is a significant overestimate. In Fig. 5.1(e) the predicted GVD of the LP_{31} mode group is approximately double the true value at $F = 0.8$ where the maximum error is observed. Near the centre of the anti-resonant window, $F = 0.65$, where leakage loss is lowest, the effects of anti-resonance are minimised and Eq. (5.3) shows excellent agreement to the true value. Other analytical expressions exist for the phase constant of the modes guided in anti-resonant structures, such as Eq. (3.6) for a floating capillary. Using Eq. (3.6) does not, however, improve the fit to GVD values compared to Eq. (5.3).

Figure 5.2(a) shows how the characteristic Bessel zero, u_{nm}, depends on mode order. The Bessel zero is proportional to the square root of mode order and applying a linear best fit to the first 50 mode groups yields the expression $u_n^2 = 8.37n - 4.26$. Figure 5.2(b,c) shows the group delay and GVD at a normalized frequency, $F = 0.65$, as a function of mode order for tubular fibres with a range of core sizes between 7x and 25x the wavelength. The data is described very well by Eq. (5.2) and Eq. (5.3). Both group delay and GVD increase approximately linearly with mode order and decrease with the square of the core radius. This is significant for applications

involving transmission of short pulses: guiding more modes in the fibre will result in increased inter-modal and chromatic dispersion and therefore increased temporal spreading of the pulses. In data transmission, dispersion will limit the maximum rate at which pulses, which carry modulated data as symbols, can be transmitted before inter-symbol interference makes recovering the data with acceptable error rates impossible. Unlike in solid-core fibres, ARF can with careful design of the cladding (see Chapter 4) be fabricated with larger cores without guiding more modes and this powerfully reduces both chromatic and inter-modal dispersion. Some applications may not permit larger cores however, e.g. direct coupling to a laser source without a focusing setup, and additionally larger cores in ARF will generally lead to increased losses due to macro- and micro-bending [84]. In the next section, alternative techniques are investigated for reducing inter-modal dispersion by bending or twisting the fibre.

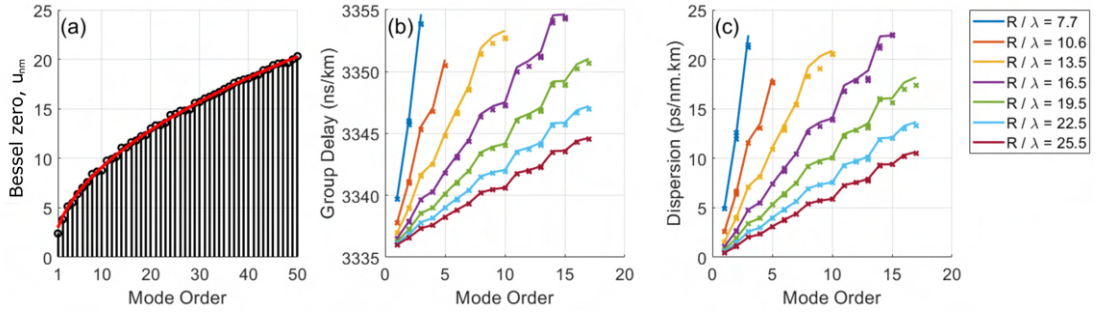

FIGURE 5.2: (a) The first 50 zeros, when taken in order of numerical value, of the Bessel functions. Black stems denote the true value. The red line is a curve of best fit described by $u_n^2 = 8.37n - 4.26$. (b) Group delay and (c) dispersion as a function of mode order for tubular geometries with a range of core sizes at a normalized frequency $F = 0.65$.

5.1.2 Effects of bending

In solid-core graded-index fibres, a variable refractive index profile in the core is well known to reduce DGD. An equivalent approach is not practically possible in hollow-core fibres but there are physical manipulations that could conceivably modify the DGD of anti-resonant fibres. A curved optical fibre can be modelled as a straight fibre with a conformal transformation of the refractive index [103].

To investigate the effects of bending on DGD, the tubular fibres described in the previous section were simulated for a range of bends. Figure 5.3(a,b) shows the delay of the first 5 mode groups of two fibres as a function of the bend radius, relative to the core diameter, R_b/D. All modes have increased delay for smaller bends and this effect is increased for lower order modes. Compared to straight, for the fibre in Fig. 5.3(a) the LP_{01} group has 2 ns/km increased delay at $R_b/D = 500$ whereas the LP_{31} group is slowed by less than 0.1 ns/km. DGD for the same fibre is shown in Fig. 5.3(c). The

increased retardation of the fundamental mode leads to a reduction in DGD which is similar in absolute magnitude for all modes, approximately 2 ns/km.

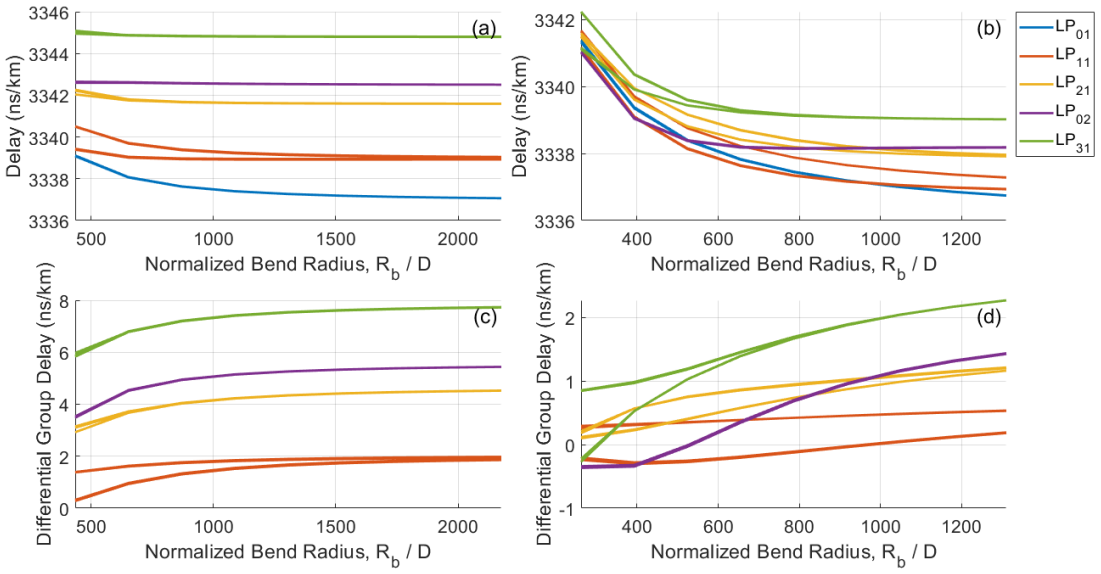

FIGURE 5.3: The (a,c) group delay and (b,d) DGD of two tubular fibres as a function of normalized bend radius. In (a,c) the fibre has $R = 23\,\mu m$ and in (b,d) the fibre has $R = 38\,\mu m$.

The fibre in Fig. 5.3(b,d) has a larger core that reduces both the delay and the DGD, Eq. (5.2). The DGD of the LP_{31} mode group when the fibre is straight is 3 ns/km, less than half that of the previously described fibre. Due to the larger core, the fibre is also more sensitive to bending; at normalized bend $R_b/D = 500$ all modes shown are retarded by 0.5 ns/km at minimum. The group delay of the fundamental mode is most affected by bending and the result is a reduction in DGD of the HOMs. The DGD of the larger fibre is shown in Fig. 5.3(d). At a normalized bend $R_b/D = 400$ the DGD of all modes is less than 1 ns/km. For the LP_{31} mode group this is a reduction of 1/3 compared to the straight fibre, showing compellingly that bending a fibre can reduce the effect of temporal pulse spreading and therefore improve the performance for multi-mode pulse delivery.

Although bending can reduce DGD, this comes at the expense of increased loss. The loss increase is greater when the DGD reduction is larger. Reducing the DGD of the LP_{31} mode group in Fig. 5.3(d) by bending also doubles the leakage loss to 0.5 dB/m compared to 0.25 dB/m when straight. If a maximum bend-radius were to be enforced as a method to reduce DGD, routing - the process of physically positioning a optical fibre to connect two points - would be significantly more complex and the effective length over which light could be transmitted would also be reduced; longer fibre lengths would be necessary to cover a distance while maintaining a constant bend. These problems make enforced bending an impractical solution to large DGD for conventional short-haul telecomms applications. Bending due to routing however will not increase the DGD. Other applications, such as non-distributed sensing, typically

employ coiled fibre to increase light-matter interaction without increasing device footprint. Where these applications employ few- or multi-moded fibre e.g. dual-mode interferometry [37], the dependence of group delay and DGD on the coil radius must be considered. Further few-mode ARF sensing applications are described in Section 5.3.

5.1.3 Twisting

Optical fibres can be given a permanent twist either during the draw down process or using post-processing techniques. In circularly symmetric fibres such as the step-index fibre this can impact the optical properties due to the photoelastic effect of silica [141]. In micro-structured, hollow-core the geometry of the fibre itself is modified. Tubular fibres like the NANF or ALIF become helicoidal, giving rise to novel optical properties. Research into such fibres is ongoing and has already found application, for example in enhancing the HOM stripping of a tubular fibre [142]. The majority of interest however is focused on the potential of data transmission using orbital angular momentum [141, 143].

When considering twisted fibres it is necessary to work with circularly polarised modes. For linearly polarised modes the field lines of the electric field are always aligned in one direction. There are two orthogonal polarisations x and y. Since the system is linear, any linear combination of two degenerate modes is also a mode. A different basis can therefore be formed from the x and y polarised modes, $\mathbf{E}_{RC} = \frac{1}{\sqrt{2}}(\mathbf{E}_{x-pol} + i\mathbf{E}_{y-pol})$ and $\mathbf{E}_{LC} = \frac{1}{\sqrt{2}}(\mathbf{E}_{x-pol} - i\mathbf{E}_{y-pol})$. In these new modes the x and y polarised light are $\pi/2$ out of phase. Hence the polarisation angle rotates as the wave propagates and the modes are called left and right circularly polarised modes, depending on the direction of rotation. The factor $\frac{1}{\sqrt{2}}$ ensures that the circularly polarised modes carry equal power to the linearly polarised modes, that is if $\mathbf{E}_{x-pol}$ and $\mathbf{E}_{y-pol}$ are normalized according to Eq. (2.16) then so too will be $\mathbf{E}_{RC}$ and $\mathbf{E}_{LC}$.

In this work, of interest is the capacity for twisting to affect the HOM properties, similar to the effects of bending described in the previous section. Twisting can be made permanent in the fibre without imposing extra difficulties in the cable or routing and could present a more practical method of reducing DGD between modes. Intuitively, the effects of twisting stems from the increase in optical path length experienced by modes propagating further from the centre of a twisted fibre. This topological effect leads to an effective refractive index change [144]:

$$\frac{\Delta n_{topological}}{n_0} = \sqrt{1 + \alpha^2 r^2} - 1 \approx \frac{1}{2}\alpha^2 r^2 \tag{5.4}$$

where α is the rate of twist, n_0 is the original refractive index and r is the distance from the centre of twist.

5.1.3.1 Transformation optics

In finite-element simulation the problem of simulating an optical fibre is significantly reduced if it is possible to simulate only a 2-dimensional cross section of the fibre. This however, relies on translation invariance in the axial direction; the cross section must not change along the length of the fibre. Translational invariance does not hold true if the fibre is twisted and so a different approach is required.

In this work, a technique based on transformation optics is employed. Transformation optics encapsulates a geometric change of coordinates into a material transform. By describing the geometry of a fibre in a twisted Cartesian space (for which the geometry at $z = 0$ is identical to the untwisted fibre) the fibre becomes invariant in the longitudinal direction. Transformation optics permits the transform into regular Cartesian coordinates to be implemented by using a complex, anisotropic material and therefore to be numerically simulated using the finite-element method in the *COMSOL* software. The details of this technique are described in detail in Appendix B.

5.1.3.2 Effects of twisting

In order to assess the effects of twisting on the properties of HOMs in ARF, numerical simulations were conducted of twisted fibre. Since the primary purpose of this section is to determine the potential for twisting to be used practically, the ALIF design previously developed in Section 4.4 for few-moded guidance in short-haul telecomms applications is studied. The geometry of this design is shown in Fig. 5.4(a) and the fibre is simulated for a range of twists up to 0.5 rad/mm. This maximum twist corresponds to full 2π radian twist every 12.5 cm and is similar to previously fabricated twisted ARFs [142, 143].

Figure 5.4(b) shows the confinement loss, at a wavelength of 850 nm, of the first two mode groups, LP_{01} and LP_{11}, as a function of the rate of twist. Modes within these mode groups are labelled with the suffixes a-d for simplicity since they represent both linearly (for the untwisted fibre) and circularly polarised modes. Loss increases for most modes as the rate of twist increases whilst other modes in the same group have the same or marginally decreased loss. The leakage loss of the LP_{01-b} mode at a twist rate of 0.5 rad/mm is approximately 3x higher than for the untwisted fibre whilst the LP_{01-a} mode shows negligible change. This circular dichroism emerges since twisting results in cladding modes carrying orbital angular momentum and therefore coupling between the core and cladding is only possible for particular circular polarisation states [143]. Core modes with stronger coupling to the cladding experience higher leakage losses.

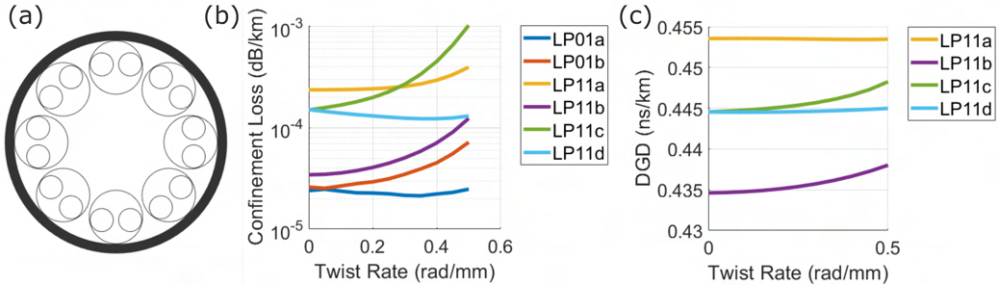

FIGURE 5.4: (a) The geometry of a 7-mode group ALIF previously designed in Section 4.4. The (b) confinement loss and (c) differential group delay of the first two mode groups of the shown fibre as a function of twist rate.

The DGD, at a wavelength of 850 nm, between the LP_{11} and LP_{01} mode group as a function of the rate of twist is shown in Fig. 5.4(c). DGD of the LP_{11-b} and LP_{11-c} modes increases with twist whilst the remaining modes in this group are approximately unchanged. The magnitude of the change in DGD is however extremely small: at 0.5 rad/mm twist the LP_{11-b} mode is retarded by 4 ps/km whereas the range of DGD values between the approximately degenerate modes of the LP_{11} group is 20 ps/km, 5x larger. Since the change in DGD is so small, only the results of the first two modes are shown in order to demonstrate the effects of twisting. Higher-order modes were considered and other ARFs simulated with similar twist rates and found similar results: DGD increases or remains constant with increasing twist but the effects are negligible. Greater rates of twist can have a greater impact but this also results in significantly increased leakage loss and is not a positive change for reducing inter-modal dispersion.

It is apparent from these results that twisting is not a useful tool for current multi-moded, short-haul telecomms. It remains of interest for other applications however such as SDM using modes carrying orbital angular momentum [144] or for the filtering or generation of circularly polarised light [143].

5.1.4 Discussion

Chromatic dispersion and inter-modal DGD of anti-resonant fibres have been investigated. Despite the complexity of their guidance mechanism, a model based on the simple hole-in-bulk silica fibre well describes the DGD. In the centre of the anti-resonant window the GVD is also well described by this model. Practically this is a very useful determination since the fibres are typically operated near the centre of the anti-resonant window where loss is minimised.

It was shown analytically and confirmed with numerical simulations that both GVD and DGD increase linearly with the mode group order and decrease with the square of the core radius. Chromatic dispersion, even for HOMs, is low compared to similar

solid-core fibres and, further, will be negligible compared to the effects of DGD for most practical applications utilising very short pulses e.g. datacomms. Chapter 4 showed that, compared to an equivalent graded-index solid-core fibre, DGD is approximately an order of magnitude larger. The effects of DGD in ARF could be reduced by increasing the core size or reducing the number of guided modes but this would come at the expense of signal power since these parameters were chosen to achieve high coupling efficiency and mimic the standards of solid-core multi-mode datacomms fibre.

The methods of reducing DGD in solid-core fibre are not possible in ARF but alternatives were investigated. Bending can powerfully reduce the DGD: the fibres considered in this section show reduction by up to a factor 2x. There is a trade-off of increased loss due to bending as the DGD decreases but this could be tolerated over short distances (e.g. < 500 m) typically considered if the straight loss of the fibre is low. However, the practical considerations of enforcing a fibre bend whilst routing cables make this unfeasible. As a possible alternative the impact of twisting, a modification which can be relatively easily built into the fibre during or after the draw, was studied. This did not have the desired effect. Instead, marginal increases in DGD were observed.

For the purposes of existing VCSEL-based short-haul datacomms I find that despite large bandwidth, low loss and low latency, prohibitively high DGD make MM ARF unsuitable as an improvement or even replacement of current graded-index solid-core fibres. This does not altogether preclude MM ARF from telecomms applications however. A simple, but computationally expensive for large DGD, mitigation strategy would be to employ digital equalisation methods. In addition WDM at lower single channel data rates can also be implemented by exploiting the wide optical bandwidth and low chromatic dispersion of the fibres.

Employing higher order modulation techniques can address the limitations of DGD whilst embracing the strengths of hollow-core fibres. Orthogonal Frequency Division Multiplexing (OFDM) is a a modulation format known for its resilience to multipath interference such as that caused by inter-modal dispersion [145]. Many (100+) orthogonal carrier frequencies (in the time domain) are modulated with very low data rates and multiplexed together. A cyclic prefix is also typically employed which acts as a temporal guard band. The combination of orthogonal carriers, individually low symbol rates and the cyclic prefix, mitigate the effects of inter-symbol interference introduced by multiple propagation paths. The implementation is usually via the Fast Fourier Transform, making OFDM far more computationally simple compared to other digital-equalisation-based DGD compensation methods. OFDM has already been demonstrated in optical links including multi-mode VCSEL/OM fibre links. Kao *et al.* achieved 64 Gb/s over 100 m of OM4 fibre [146]. OFDM is one of the schemes under consideration for future 200 and 400 Gb/s standards. The cost of OFDM is the

requirement for higher power or more expensive modulation electronics to compensate for the higher peak to average power ratio. The low-loss of ARFs however, should reduce the required power budget of the link and help to reduce the impact of any higher power electronics.

5.2 High power delivery in multi-mode ARF

High-power fibre delivery typically employs solid-core large-mode-area or large-core multi-mode fibres, primarily limited by the onset of nonlinear processes [147]. The maximum power distance product, before stimulated Raman scattering significantly modifies the signal, is given by $P \cdot L_{\text{eff}} = 16A_{\text{eff}}/g_r$, where P is the laser power, L_{eff} is the effective interaction length of the fibre, A_{eff} is the effective interaction area and g_r is the Raman gain coefficient (for a large core, multi-mode silica fibre $L_{\text{eff}} \approx L$ when $L < 100\,\text{m}$, $A_{\text{eff}} \approx \pi(0.8R)^2$ and $g_r = 1 \times 10^{-13}\,\text{m}\,\text{W}^{-1}$) [148]. Higher powers delivered over a short distance experience the same nonlinear behaviour as low power delivered over long distances. In solid-core fibres, transmission of 1 kW of power over 100 m has been reported in a highly multi-mode (˜750 modes) step-index fibre [149] and 10 kW over 30 m has been demonstrated in a three-mode photonic crystal fibre [150]. Commercially available solutions are typically limited to a few 10s of metres e.g. a commercial multi-mode 10 kW fibre laser has a 100 µm delivery fibre up to 30 m long [151]. ARFs by contrast intrinsically possess greatly reduced optical nonlinearity compared to silica fibres since the overlap between the silica and propagating light is less than 1×10^{-4} [10] and the nonlinear coefficient of air is almost three orders of magnitude lower than silica [152]. The unique properties of ARFs raise the potential for significant improvements in reach, flexibility and power handling capabilities of their solid-core counterparts.

Practical demonstrations of laser power delivery through hollow-core fibres have greatly progressed over the past two decades [38, 153–155], culminating in the recent remarkable demonstration of 1 kW continuous-wave (CW) power transmitted over 1 km of single-mode NANF [26]. This body of work has so far focused on the transmission of high quality, single-mode laser beams with low M^2. Greater laser power still is available from few-mode and multi-mode lasers [156], and there are a broad range of applications which would benefit from the ability to deliver such lasers across long distances using fibres.

The performance of such few-mode/multi-mode high-power laser sources has also seen great progress in recent years [156]; the markers in the plot shown in Fig. 5.5 represent a selection of commercially available or research grade lasers of various architectures, both pulsed or cw, emitting near 1030 nm. Higher power lasers in general are effectively few-moded or multi-moded, exhibiting larger M^2 values. To

efficiently couple light from these sources into a fibre requires a similarly few-mode or MM fibre. To illustrate this, the same plot shows the calculated approximate number of mode groups a hollow-core fibre must guide to achieve at least 95 % coupling efficiency to a laser source with a given M^2 value (details of the calculation are given in Section 5.2.1). It is clear therefore that to meet the needs of applications requiring the flexible delivery of optical power from such lasers over some distance, low-loss multi-mode hollow-core fibres must be designed.

In this section, the range of sources targeted for ARF delivery (highlighted in Fig. 5.5), comprises lasers with output powers ranging from 1 to 30 kW with reported M^2 values from 1.5 to 15. For M^2 values below the region of interest, i.e., $M^2 < 1.5$, the near diffraction-limited, approximately single-mode lasers emitting up to several kW average power can be delivered, as shown by the results of Mulvad *et al.* [26], through single-mode NANFs over several kilometres (e.g. Mulvad *et al.* predict the delivery of 5 kW over more than 2 km with an air-filled core). Above the region of interest, $M^2 > 15$ laser sources can emit more than 100 kW average power [151]. These lasers are highly multi-mode (i.e. more than 100 mode groups) and fibre delivery is typically through highly multi-mode solid-core fibres with core diameters as large as 800 µm [151]. It is conceivable that ARFs might one day be designed to guide the several 100s of mode groups required to efficiently couple light from these sources, however, it is not the subject of this work. Instead the focus is on the intermediate range $1.5 < M^2 < 15$ where MM ARFs can offer significant improvements on the performance of solid-core fibres.

In the following section, calculations are presented determining the required modality of an ARF to achieve a high coupling efficiency with multi-mode lasers with a given M^2. Next, a procedure is described to design multi-mode NANFs to guide the required number of modes with low leakage loss and high bend resilience. Finally, the performance of NANFs for high power delivery is examined and discussed by designing and simulating two example designs.

5.2.1 Coupling of multi-mode laser beams into ARFs

The quality of a beam is often characterised by the M^2 factor, defined as the ratio of the beam parameter product to that of an ideal, diffraction-limited Gaussian beam [172]. The highest possible beam quality is achieved with $M^2 = 1$ and the power is fully transmitted in the lowest divergence fundamental mode. Greater M^2 values correspond to beams with larger divergence angles caused by a fraction of the total power being transmitted by higher-order and higher divergence modes. Since the transverse profile of these modes differs from that of the near-Gaussian fundamental mode, beams with a larger M^2 will not couple efficiently into single-mode fibre and MM delivery fibres are required for adequate coupling efficiency.

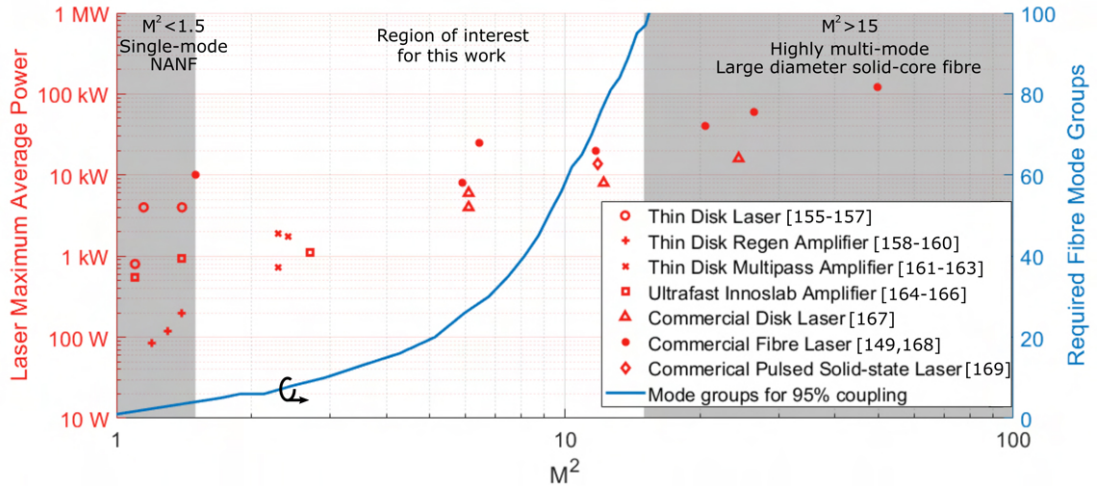

FIGURE 5.5: (red markers, left axis) The maximum average power output of high power laser sources and their reported M^2 values [151, 157–171]. (blue line, right axis) the number of mode groups required to be guided in a hollow-core fibre to achieve 95% coupling efficiency for an incident laser beam of a given M^2. The laser described by [170] is characterized only as single-mode and $M^2 = 1.5$ is assumed.

For example, a MM step-index fibre with numerical aperture 0.22 and core diameter 50 µm will guide several 100s of modes and the larger cores typically used for high power delivery can guide many times more. The highly multi-mode nature of these fibres mean they are easily capable of efficient coupling with large M^2 beams. Due to the strong differential properties between modes in ARF (see Section 3.1), knowledge of the number of modes required to accommodate a beam with a given M^2 is crucial in designing a fibre with the best performance possible.

In high-power delivery through fibre, high input coupling efficiency is necessary both to achieve high throughput and to avoid thermal damage to the input facet of the fibre since the laser energy that is not coupled into the core may be absorbed by the coating near the fibre end face and damage it. In this work, the target is the design of fibres enabling at least 95 % coupling efficiency to a given MM laser source. This is the highest efficiency I am aware of being practically reported in ARF [173]. Such high coupling efficiency should reduce the requirement for active cooling at the fibre coupling and enable further power upscaling. Investigating this target begins by considering how the modes of an ARF are excited by an incident field.

In order to describe the transverse field of a high M^2 laser beam, the Laguerre-Gaussian formulation is employed which describes a free space laser mode as:

$$\mathbf{E}_l^{(\mathrm{LG})}(\rho,\phi) = \vec{\mathbf{t}} \cdot \left(\frac{\rho\sqrt{2}}{w_0}\right)^{|m_l|} \exp\left(-\frac{\rho^2}{w_0^2}\right) L_{n_l}^{|m_l|}\left(\frac{2\rho^2}{w_0^2}\right) \exp(-im_l\phi) \tag{5.5}$$

where $\vec{\mathbf{t}}$ is the electric field polarisation vector, w_0 is the beam waist, m_l and n_l are the radial and azimuthal mode indices respectively of the l^{th} Laguerre-Gaussian mode and $L_n^m(x)$ is the Laguerre polynomial. The Laguerre-Gaussian modes form a complete, orthogonal set and, given normalization according to Eq. (2.16), the emitted laser beam can be described as a linear sum of those modes.

$$\mathbf{E}^{(\mathrm{i})} = \sum_l c_l \mathbf{E}_l^{(\mathrm{LG})}, \quad \mathbf{H}^{(\mathrm{i})} = \sum_l c_l \mathbf{H}_l^{(\mathrm{LG})} \tag{5.6}$$

This description has the advantage that the M^2 value of a laser beam is obtained from its modal decomposition as [174]:

$$M^2 = \sum_l (1 + m_l + 2n_l)|c_l|^2 \tag{5.7}$$

For Eq. (5.7) to hold, the beam must be propagating unit power, i.e. $\sum_l |c_l|^2 = 1$.

Figure 5.5 shows the number of mode groups required to be guided in a fibre to achieve the target of 95 % coupling efficiency for a given incident beam, characterised by its M^2 value. A beam with $M^2 = 15$ requires almost 100 mode groups. For this calculation the modes of the fibre are taken to be those of a hollow, circular fibre (a circular air hole in bulk silica, see the $N = 0$ structure in Fig. 5.8) as determined by Marcatili and Schmeltzer [18]. Coupling efficiency is calculated using Eq. (2.18). Numerical simulations were conducted of a range of ARF geometries including tubular, NANF and DNANF and, although the transverse mode profiles are different for the same mode order in each of these structures, they all exhibited nearly identical requirements on the number of mode groups as that of the hollow circular fibre shown in Fig. 5.5. An $M^2 = 3$ beam would require approximately 10 mode groups but the number of mode groups required to achieve the 95% coupling efficiency increases rapidly with M^2; an $M^2 = 10$ beam requires around 60 mode groups and $M^2 > 15$ requires more than 100 groups. In the next section it is discussed how these requirements relate to ARF design.

It is clear from Eq. (5.7) that different combinations of the same modes, i.e. beams with different transverse fields, can result in equal M^2. Indeed, M^2 alone does not capture the richness of the corresponding mode field distributions. Figure 5.6(a-c) shows three different possible modal distributions of an $M^2 = 3$ laser beam and the distribution in the modes of a fibre after coupling. The laser distributions are distinct and result in the excitation of different fibre modes. In Distributions 1 and 3 there is negligible power outside of the first 5 mode groups of the laser but for both distributions, more than 10 % of the power is captured by mode group 6 and above in the fibre. Distribution 2 has the most evenly distributed power initially and is the most similar to the final distribution in the fibre. Shown in Fig. 5.6(d) is how the different laser beam

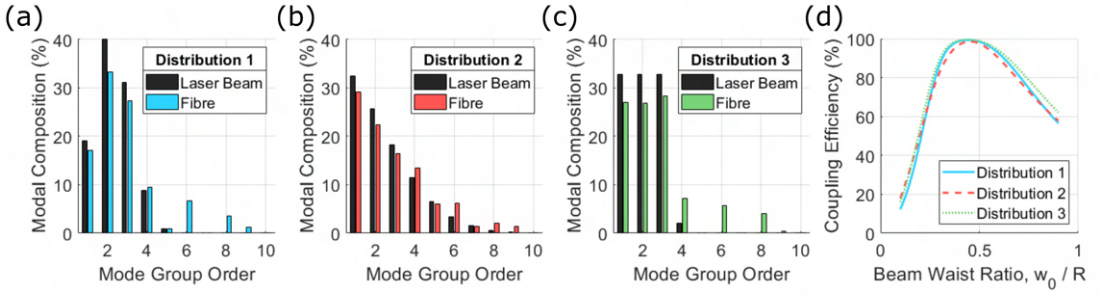

FIGURE 5.6: (a-c) Several different modal distributions of (black bars) laser beams with $M^2 = 3$ before and (coloured bars) after coupling into a fibre. (a) Distribution 1 and (b) Distribution 2 are described by discrete Gaussian functions with standard deviation 1 and 3 respectively and mean chosen to achieve the target M^2. (c) Distribution 3 is flat across lower order modes with the power of the highest order mode chosen to achieve the target M^2. (d) The total coupling efficiency of the beams described by (a-c) incident on a 10 mode fibre as a function of the beam waist ratio.

distributions affect the coupling efficiency into the fibre as a function of the beam waist ratio, defined as the ratio between the laser beam waist and the fibre core radius, w_0/R. Regardless of the exact modal distribution, the same number of fibre modes is capable of capturing $> 95\%$ of the beam. The maximum difference between the distributions shown here is 5 % but, at the optimum beam waist ratio, the discrepancy is less than 1 % and generally the results are nearly identical across the entire range. Note that beams with increased higher-order mode content are optimally coupled at smaller values of beam waist to core radius ratio, w_0/R. Coupling to single-mode beams is known to be maximised near $w_0/R = 0.7$ [73] whereas this $M^2 = 3$ beam has a maximum coupling at $w_0/R = 0.45$.

Throughout the research for this work, a range of input beams were investigated and, for all metrics explored, M^2 was found to be a robust measurement with beams of diverse modal composition but equal M^2 achieving similar coupling efficiency into the fibres. Given the similarity between results, for the remainder of the chapter the modal decomposition described by the parameters of Distribution 2 in Fig. 5.6(b) is used.

5.2.1.1 Coupling efficiency of HOMs in second anti-resonant window

In high-performance applications, when coupling power into an optical fibre, even a subtle increase in coupling efficiency can make a significant difference to the performance of that system. This is even more valid in high-power systems, such as those discussed in this section, where high coupling efficiency improves not only the power performance but also the safety of the system. Fokoua *et al.* demonstrated that in single-mode ARFs, coupling efficiency could be improved by almost 2% by operating the fibre in the second anti-resonant window rather than the fundamental window [73]. Although the available optical bandwidth is reduced in the second

anti-resonant, an improvement to coupling efficiency is more important in this application.

To investigate the possibility of improved coupling efficiency in the second anti-resonant window, two 10-tube NANFs, with core radius core radius $R = 35\,\mu m$ and inter-tube gap $d = 4\,\mu m$, guiding 12 mode groups at $\lambda = 1030\,nm$ were simulated. The wall thickness of the NANFs was 350 nm and 700 nm respectively corresponding to a normalized frequency $F = 0.71$ in the fundamental window and $F = 1.42$ in the second window. The coupling efficiency was calculated between the fibre modes and their equivalent Laguerre-Gaussian laser modes, e.g. the LP_{01} fibre mode and the LP_{01} Laguerre-Gaussian mode. Figure 5.7 shows this like-like modal coupling efficiency for the first and second window NANFs when the laser beam is focused to the optimal value for that mode. Both fibres have highest coupling efficiency in the fundamental LP_{01} mode group, approximately 98%, which decreases for higher-order modes. The lowest coupling efficiency amongst the first 12 guided mode groups is, for both fibres, less than 78% in the LP_{32} mode group. Coupling efficiency decreases more rapidly with increasing radial mode order than azimuthal mode order. There is more than a 10% drop between the LP_{01} and LP_{02} mode groups and between the LP_{11} and LP_{12} groups, whereas between the LP_{01}, LP_{11} and LP_{21} mode groups the total drop in coupling efficiency is less than 3%. This suggests that the number of modes required in an optical fibre to achieve high coupling efficiency increases more rapidly than the number of modes in the incident laser beam. It should be stressed that a real multi-mode laser beam carries power in a some or all of these modes and optimal focusing will not be possible for all modes simultaneously.

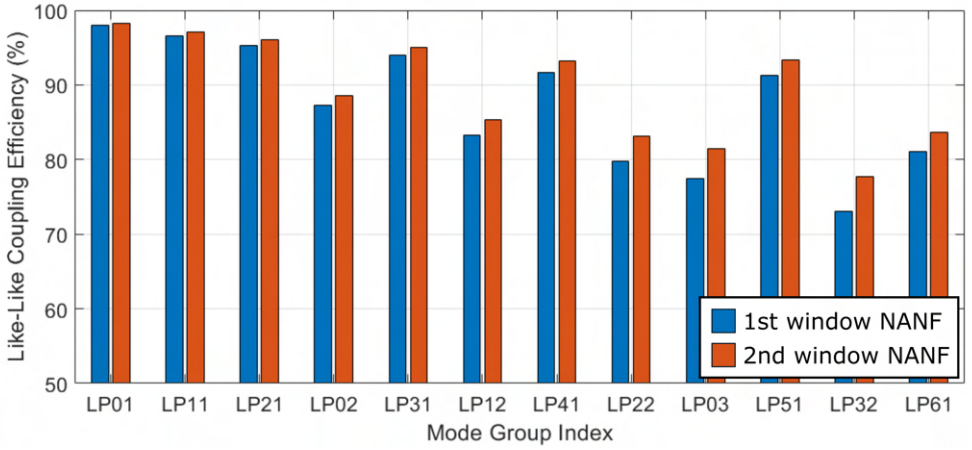

FIGURE 5.7: The modal coupling efficiency of Laguerre-Gaussian laser modes into the same mode of a multi-mode NANF operating in either the fundamental or second anti-resonant window.

When comparing the first and second window NANFs, higher coupling efficiencies are found in the second window NANF. Coupling efficiency in the highest order, LP_{61}, mode group is 2.5% greater in the second window NANF and the improvement is

more than 4% in the lowest efficiency, LP_{32}, mode group. The increase in the fundamental mode however is less than 0.25%. In general, the improvements found by operating the fibre in the second anti-resonant window are minimal for the lowest-order modes and increase with mode order. This is understood by considering the mechanism for the increase in coupling efficiency. The electric field of a mode operating in the fundamental window changes sign as it crosses the thin capillary separating the core and the cladding, i.e. it is positive in the core and negative (but with small magnitude) in the cladding. The mode field of a Gaussian beam is always positive and so the overlap integral (Eq. (2.18)) is reduced by the contribution of the cladding regions. See ref [73] for a detailed description. By contrast, in the second anti-resonant window, the sign of the fibre mode changes twice when crossing the capillary wall and is therefore positive in the core and cladding. The overlap integral in a second-window NANF is increased by the cladding contribution. Evidently, not only is the sign of the fibre mode electric field in the cladding but also the magnitude relative to in the core since this determines how large the effect on the overlap integral is.

In Chapter 3 the fraction of power guided in the cladding regions in different modes was studied. Figure 3.6 shows that the amount of power in the cladding tubes is proportional to the degree of coupling to the cladding tube modes. In an anti-resonant fibre with all core modes guided in the fundamental phase-mismatch window, the highest order core mode always exhibits the strongest coupling to cladding modes and this decreases for lower-order modes. This agrees with the results shown in Fig. 5.7; highest-order core modes have the strongest coupling to cladding tube modes, therefore have the highest fraction of power in the cladding tubes and as a result have the largest increase in coupling efficiency when operating in the second anti-resonant window. In a single-mode fibre, as in Ref [73], the fundamental mode is the highest order mode and has similar coupling strength to cladding tube modes as the highest order core modes in a multi-mode fibre. The increase in coupling efficiency in both cases is therefore similar.

For the multi-mode laser beams considered in this section, a significant fraction of power is coupled into low-order fibre modes, which exhibit marginal increase in coupling efficiency in the second anti-resonant window. When calculating the modal requirements of NANFs operating in the second anti-resonant window, therefore, there was a negligible improvement over NANFs operating in the fundamental anti-resonant window. For the remainder of this work, only fundamental-window NANFs are considered since these exhibit larger optical bandwidths.

5.2.2 Designing MM ARF for high power laser delivery

Previously in this thesis, in Chapter 3, the theory underlying differential modal loss was discussed and in Chapter 4 various designs of ARF were investigated to achieve an optimised, few-moded ARF with low loss given a strict core size requirement. In this section the goal is to to investigate the potential of ARFs for high-power delivery and towards this, a simple yet robust design process is presented for NANFs to guide the number of modes required to effectively capture and guide radiation from a multi-mode, high power laser. A minimum core size requirement is derived and the technique described in Section 4.2.3 is used to design the cladding of a NANF to achieve multi-mode guidance. The fibres resulting from this process could be further optimised if they were to be used practically.

5.2.2.1 Minimum core size

To determine the core size of the fibre, the starting point is to define the maximum acceptable loss coefficient suitable for the intended application. In this work only losses due to leakage are considered. Because of the larger cores, surface scattering remains negligible [10] and whilst micro-bending increases rapidly with core size [84], it is speculated that these fibres could be packaged in such a way that its contribution is also negligible. For MM guidance the fibre must be designed such that all modes have losses below the loss threshold. Since, generally, the highest order mode will have the highest loss and knowing the highest order mode from the coupling requirements (Fig. 5.5) one need only design the fibre such that the highest-order mode is below the loss threshold.

As previously described in Section 3.1.1 the leakage loss of an ARF geometry which consists of concentric rings of air and glass has been determined in closed form by Bird [95]. Since ARFs of interest cannot be modelled analytically, the closed form expression for the leakage loss of concentric ring fibres is used as a basis for the following analysis. In Eq. (3.1) the geometry is characterised by N which is the integer number of finite concentric rings (including both air and glass regions) which make up the cladding (see Fig. 5.8 for examples). For the hollow circular fibre considered in the previous section $N = 0$, whilst for tubular, NANF and DNANF structures N most closely resembles 3, 5 and 7 respectively [10, 49] (note that N is independent of the number of sets of nested capillaries surrounding the core). For the analysis in this work $\phi_{\text{glass}} = 2\pi t\sqrt{\epsilon_r - 1}/\lambda$ and $\phi_{\text{air}} = \pi/2$. To target an operating wavelength of 1030 nm, a membrane thickness is chosen, $t = 350\,\text{nm}$, that corresponds to a normalised frequency, $F = 0.71$ (see Eq. (2.25)) placing 1030 nm near the expected minimum loss of the fundamental anti-resonant window [68]. The choice of ϕ_{air} corresponds to an "optimal" width of the air regions in the concentric ring structure.

Whilst there is no simple equivalent concept of an optimal width of air regions in NANF (see discussion in Section 3.1.1), they have been demonstrated to have lower losses for the same core size than even the most optimal concentric ring structure [10].

Figure 5.8 shows for a range of geometries the minimum core diameter, determined by Eq. (3.1), to guide 10, 30, 60 and 100 mode groups below a threshold of 10 dB/km. The 10 dB/km threshold is chosen such that these fibres will be capable of delivering power over 100 m with lower than 1 dB leakage loss. In reality practical fibres are expected to have lower confinement loss since tubular, NANF and DNANF structures generally have reduced leakage compared to the most similar concentric ring structures. Equation (3.1) suggests that tubular fibres with core diameters of 140 µm can support up to 10 mode groups and hence could be made to efficiently capture light from $M^2 \leq 3$ sources. As with solid-core fibres however, the additional loss due to bending increases with the size of the core in ARFs [82]. Such large core tubular fibres suffer from very severe bend loss.

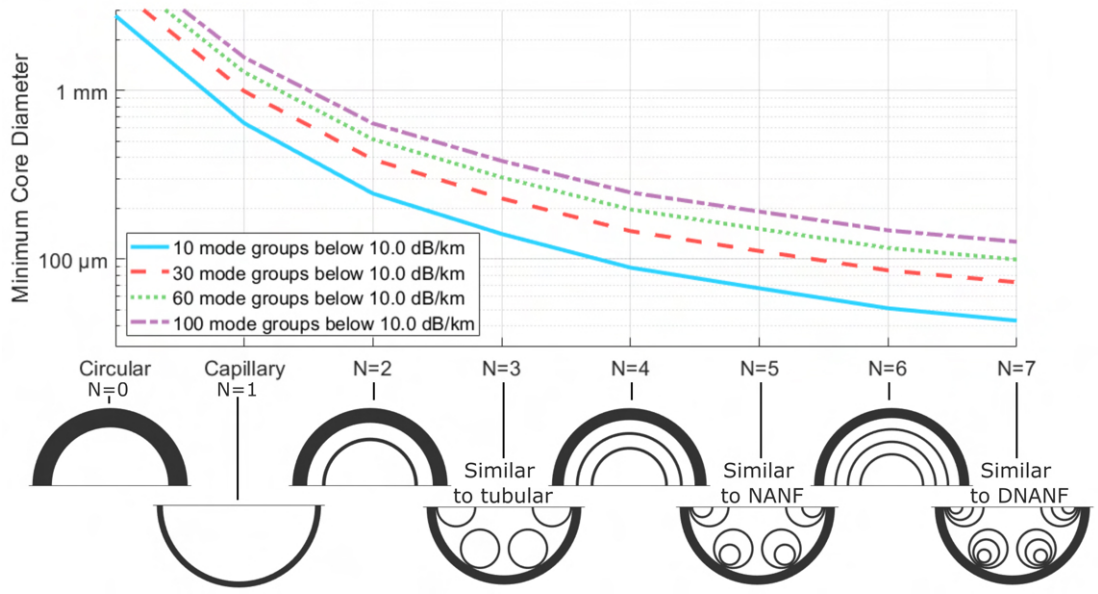

FIGURE 5.8: The predicted minimum core size, according to Eq. (3.1), in order to guide 10, 30, 60 or 100 mode groups with a maximum loss less than 10 dB/km at 1030 nm for different ARF structures.

A NANF with a core diameter of 150 µm is predicted to guide at least 60 mode groups, whilst 10 mode groups can be guided with a core diameter of around 70 µm. In addition to the smaller core size, NANFs are well known to have significantly improved bending resilience compared to tubular fibre (eg more than 4 orders of magnitude lower losses for 80 µm core diameter at 8 cm bend radius [10, 82]). Figure 5.8 shows that to guide 100+ mode groups a NANF would require a core diameter of approximately 300 µm. Such large core NANFs have higher bend loss and are not capable of low-loss, multi-mode operation with a 35 cm bend radius. If it is desired to guide a few 100 mode groups in an ARF, Eq. (3.1) suggests that DNANF

might be the structure of choice, with smaller core requirements and even better resilience to bending compared to the NANF [22]. This solution may be capable of guiding similar number of modes to MM solid-core fibre and be suitable for delivering laser light from highly multi-mode, $M^2 > 15$ sources. The task of investigating this prospect is left for future work. Here, laser sources with $M^2 < 15$ are targeted and therefore the analysis is limited to studying NANFs with fewer than 100 mode groups.

5.2.2.2 Cladding design

To make a MM NANF, coupling between core and cladding modes must be avoided. In Chapter 3 a technique was developed to design the cladding of NANFs to predict the cladding tube mode effective indices and maximise multi-mode performance. When the size of the nested tube relative to the outer tube is such that $Z_2/Z_1 \approx 0.7$, the IC_1 and IC_2 cladding modes guided in the tube air regions are approximately phase matched. When using this technique the effective index of both the core modes and cladding tube modes can be approximated using Eq. (3.6) with the radius of the core for the core modes and of the nested cladding tube for the cladding tube modes.

Figure 5.9(a) shows the geometry of a NANF with $Z_2/Z_1 = 0.7$ and a core radius of 35 µm. The core size is chosen using Fig. 5.8 to meet the loss requirements previously discussed for a 10 mode group fibre. The size of the nested capillary tube, Z_1 can then be chosen such that phase matching is avoided between the cladding modes and the desired first 10 core modes. The number of outer tubes and inter-tube gap is selected to maintain the core radius without introducing too large gaps, which incur high leakage loss, or too small gaps, which are difficult to fabricate. The fibre in Fig. 5.9(a) has 10 outer tubes, a gap $d = 4$ µm and the nested tube diameter is $Z_1 = 14$ µm. For this geometry, Fig. 5.9(b) shows the effective index, calculated using Eq. (3.6), of the first 10 core mode groups (coloured solid lines) from the LP_{01} to LP_{51} and of the fundamental cladding tube mode (black dotted line). The effective index decreases for increasing core mode group index. A phase mismatch of 2×10^{-4} between the core and cladding modes is found to be sufficient to avoid strong coupling.

It is desirable to ensure in the design phase that bending will not introduce significant losses. This can be also be approximated, without numerical simulation, using the techniques described in Section 4.2.2. For tolerable bends that do not introduce significantly higher losses, the effective index of the core modes will be approximately unchanged compared to the straight fibre. The effective index of cladding tubes is modified: it is elevated for modes guided in tubes on the outside of the bend (where the optical path length is increased) and reduced for those on the inside. Substituting Eq. (4.1) into Eq. (3.6) yields an expression for the modified cladding mode effective index. The important value is the largest cladding mode effective on the outside of the bend, which has the smallest phase mismatch with core modes and therefore the

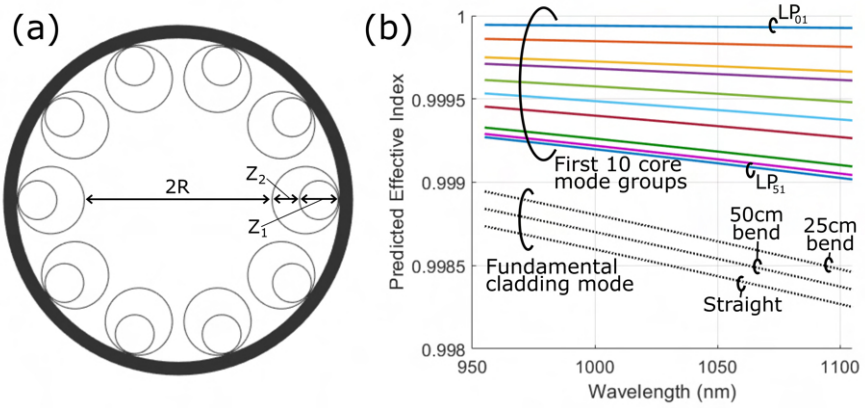

FIGURE 5.9: (a) The geometry of a 10-tube NANF with core radius $R = 35\,\mu m$ and (b) the predicted effective index of the first 10 core mode groups using Eq. (3.6) and the fundamental cladding tube mode when straight and bent using Eq. (3.6) and Eq. (4.1).

strongest coupling. Figure 5.9(b) shows the calculated effective index for this cladding tube mode when straight and under a 25 and 50 cm bend radius. The effective index is increased for a smaller bend radius. This allows the fibre to be designed such that strong phase-mismatch and low-loss operation is achieved for the bends required by the targeted application.

5.2.3 Performance of Multi-mode NANF for laser delivery

To assess the performance of MM NANFs for laser delivery two fibres are designed at the extremes of the M^2 range of interest. Figure 5.10 shows the cross sections of Design 1 and Design 2, chosen using the techniques of Section 5.2.2 to deliver power from a laser with $M^2 = 3$ and $M^2 = 13$, respectively. To efficiently guide light from lasers with such parameters the fibres are required to guide 10 and 62 mode groups, respectively (see Fig. 5.5). Using Eq. (3.6) to avoid coupling to cladding modes, Z_1 is set to 7 µm and 6 µm, respectively and $Z_2/Z_1 = 0.7$. A gap size, $d = 4\,\mu m$, is chosen comparable to recently fabricated NANFs [21]. With these parameters the minimum core diameter requirement can be met with 10 and 24 tubes for Design 1 and 2, resulting in core diameters of 69 and 176 µm, respectively. To check if fibres designed with the proposed method exhibit the desired properties, numerical simulations of Design 1 and 2 were conducted.

5.2.3.1 Propagation and bending loss

Figure 5.11(a) shows the loss spectrum of the highest loss modes of the fibres when straight. Minimum leakage loss is 1.4 dB/km at 1050 nm for Design 1 and 0.8 dB/km at 1030 nm for Design 2. Loss increases at shorter wavelengths, as the edge of fundamental anti-resonant window is approached. At 970 nm, the increase in loss is

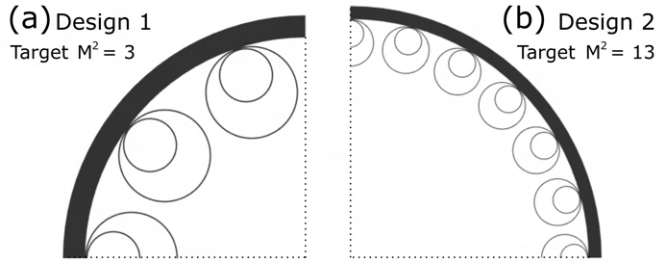

FIGURE 5.10: Geometry of (a) design 1, a 10 mode group fibre and (b) design 2, a 62 mode group fibre.

less than 0.3 dB/km for both designs. The available bandwidth is suitable not only for CW lasers, but also for ultrashort pulsed lasers operating between 1030 and 1064 nm (a 100 fs Gaussian pulse at 1064 nm has a bandwidth of less than 20 nm, see Eq. (2.21)). Figure 5.11(b) shows the maximum loss across all modes of the fibres for a range of bend radii. The critical bend radius, at which the loss is doubled compared to the straight fibre, for Design 2 is 35 cm and for Design 1 is less than 25 cm. The similarity between Design 1 and 2 in the dependence of loss with bend radius suggests that the additional loss experienced when bending the fibre is primarily due to phase matching to cladding modes. When the fibre is bent to a smaller radius, the real component of the effective index of the cladding modes in the tubes on the outside of the bend increases (Eq. (3.6)) whereas the effective index of the core modes is approximately unchanged (smaller bends than those considered here may also modify the effective index of the core modes) [82]. Consequently the core and cladding modes have increased phase matching and the loss of the core modes increases [107]. Both designs demonstrate strong resilience to bending and are below the design threshold of 10 dB/km for bend radii as small as 25 cm radius. This is below the expected minimum bend radius in practical situations where the fibre is deployed in a protective cable and bend loss is not expected to be a limitation.

To better capture the throughput capability of the fibre when used in laser delivery, Fig. 5.11(c) shows the delivered output power after coupling and propagation for a $M^2 = 3$ beam incident on Design 1 and a $M^2 = 13$ beam incident on Design 2. The loss values shown here are calculated for a fibre coiled at a constant 35 cm radius bend. In both cases the initial power loss value at the propagation distance $L = 0$ is due to input coupling and will be discussed later. In these calculations the effects of power coupling between the modes of the fibre are not included. Under these assumptions, in both designs, after 2 km of propagation the total loss is predicted to be less than 0.5 dB and the leakage loss is less than 0.14 dB/km. Given such low leakage loss it is reasonable to assume that micro-bending, which increases rapidly with core size [84], will become the dominant source of propagation loss. Although the impact of micro-bending can be reduced or mitigated with choice of fibre packaging, given the lack of relevant experimental or theoretical data on large core, multi-mode ARF, the

work is restricted to studying the effects of differential leakage loss and multi-mode guidance. The effective leakage loss is predicted almost an order of magnitude less than the loss of the highest order mode. This result is understood by considering Fig. 5.11(d), that shows the confinement losses of the 10 mode groups of Design 1 at 1030 nm. The loss of lower order modes is significantly less than the highest order mode. Indeed, the loss of the fundamental mode of Design 1 is nearly 3 orders of magnitude lower than the highest order mode. When launching power into MM fibre the low order fibre modes capture a significant fraction of the laser power (see Fig. 2.18) and so the total loss is consequently lower than that of the highest order mode. The fraction of power that propagates in the glass is shown in the right axis of Fig. 5.11(d) and increases with mode order. The glass fraction for the highest order modes is less than 4×10^{-5}, similar to the fundamental mode in single-mode NANFs [10], and the nonlinear contribution from silica is not expected to increase in multi-mode ARFs. Increased glass overlap has an effect on dispersion which is discussed in Section 5.1.1.

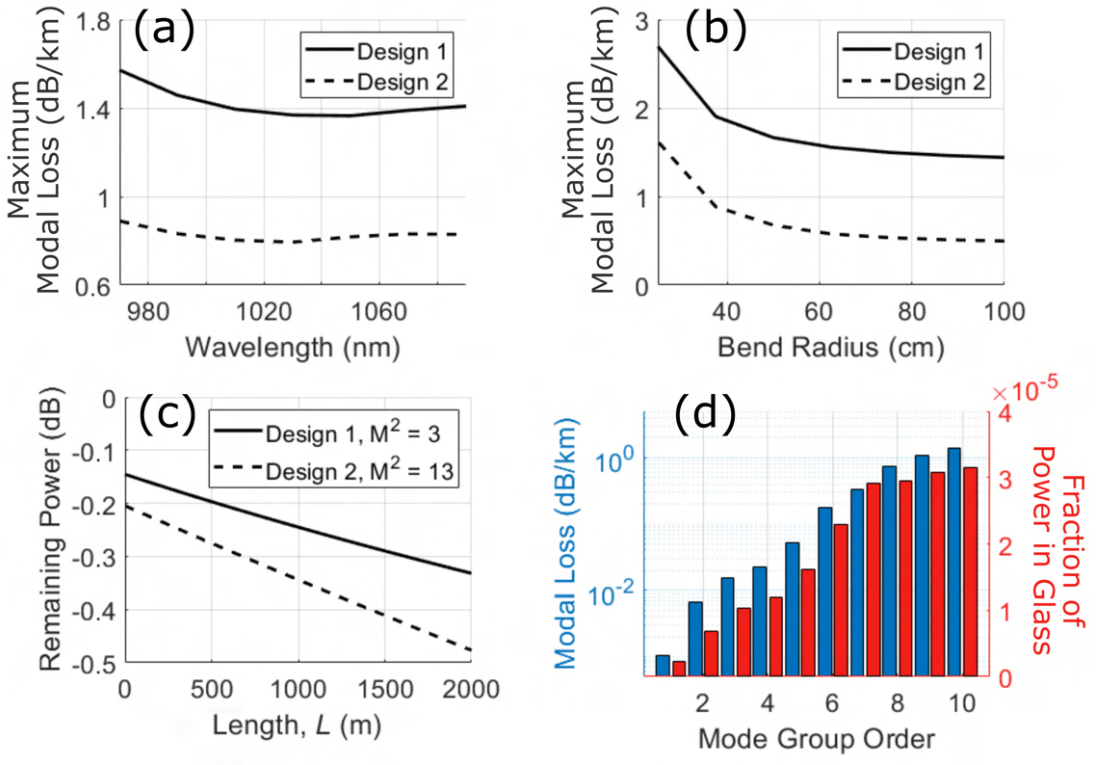

FIGURE 5.11: (a) The maximum modal loss across all modes of Design 1 and 2 when straight. (b) The maximum modal bending loss at 1030 nm across all modes of Designs 1 and 2. (c) Delivered power after coupling and propagation for a $M^2 = 3$ beam incident on Design 1 and a $M^2 = 13$ beam incident on Design 2. Loss values consider a constant 35 cm bend. (d) The maximum leakage loss (blue bar, left axis) and the fraction of power in the glass (red bar, right axis) of all mode groups of Design 1 at 1030 nm when straight.

Considering the M^2 of the laser beam at the output of the fibre, there was a negligible

change compared to the incident beam, due to the extremely low, < 0.5 dB, losses. The effects of power coupling between the modes of the fibre may modify the output M^2 [48]. Most applications using these large M^2 sources will be tolerant to small changes in beam quality as measured by M^2. If necessary, the guidance mechanism of ARF does suggest a means of limiting the maximum output M^2 by designing the fibre such that any undesired modes, those with higher order than the initial design, have high enough losses that any power in those modes will be lost after propagation through the length of the fibre. The output M^2 would therefore be effectively limited by the highest order, low-loss fibre mode. This technique could be used to counter the effects of inter-modal coupling or indeed to spatially filter the laser source, improving its M^2. Although this would incur additional power loss, it might be more desirable to develop longitudinal cooling techniques to dissipate power over the length of the fibre rather than at the fibre coupling where it can result in dangerous heat build-up. Investigating this possibility could be useful future research.

5.2.3.2 Coupling efficiency

In an industrial environment the coupling between the laser and fibre will generally experience variations in focus and alignment due to e.g. thermal fluctuations and mechanical vibration. Maintaining coupling in these conditions is important if the fibre is to avoid thermal buildup due to lost power at the coupling and maintain the throughput power delivered to the workstation. The behaviour of the fibre when the incident beam is perturbed from optimal focus and alignment is now described. The coupling efficiency of Design 1 for a $M^2 = 3$ beam at different values of beam waist ratio, w_0/R, is shown in Fig. 5.12(a). The coupling efficiency decreases as beam waist departs from the optimum, $w_0/R = 0.48$, where it reaches 96 %. For Design 1, a change in beam waist of $\pm 7\%$ still results in 95 % coupling or above. Figure 5.12(c) shows the coupling efficiency for Design 1 as an incident $M^2 = 3$, $w_0/R = 0.48$ beam is offset transversely. The coupling efficiency at zero offset, 96 % (the optimum described above), decreases as alignment offset increases. There is moderate tolerance to misalignment: a beam with a transverse offset of 10 % of the core radius still achieves 95 % coupling efficiency. The offset beam excites the fibre modes differently, with more power coupled into the higher order modes which increases the effective loss of the fibre. Input coupling remains the dominant source of loss, however, and the total loss over 2 km with 10 % transverse offset is less than 0.2 dB greater than an ideal launch with no offset.

Figure 5.12(b) and Fig. 5.12(d) show, for Design 2 and a $M^2 = 13$ beam, the behaviour of coupling efficiency with variation in focus and misalignment respectively. The results are qualitatively similar to that of Design 1; there is an optimal beam waist and the coupling efficiency decreases with detuning from optimum focus or increasing

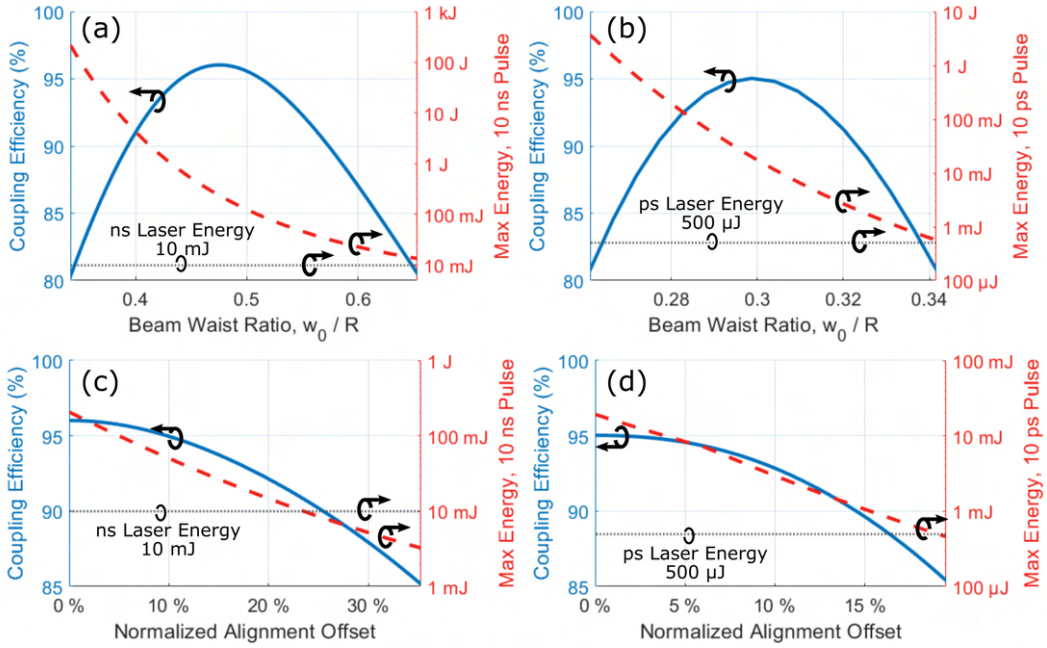

FIGURE 5.12: The coupling efficiency (blue solid) and maximum pulse energy (red dashed) before damage for (a,c) a 10 ns, $M^2 = 3$ pulse incident on Design 1 and (b,d) a 10 ps, $M^2 = 13$ pulse incident on Design 2. The beam is modified by varying (a,b) the beam waist ratio at zero alignment offset or (c,d) the alignment offset at optimal beam waist. Alignment offset is normalized relative to the fibre core radius. The horizontal dotted line indicates the maximum pulse energies of high-energy, commercial nanosecond and picosecond lasers. [175, 176].

transverse offset. The maximum coupling efficiency is 95 %. When the transverse misalignment is 10 % of the core radius or the focus is ±5% from optimal, coupling efficiency is 2.5 % lower than maximum. The increased higher order mode content of the $M^2 = 13$ beam results in a smaller optimal beam waist ratio, $w_0/R = 0.30$ compared to the $M^2 = 3$ beam used with Design 1. The maximum coupling efficiency and tolerance to misalignment and focus is improved by guiding more modes in the fibre.

5.2.3.3 Damage threshold for pulsed lasers

The light induced damage threshold (LIDT) of an ARF is the maximum power it can withstand before the intensity on the glass micro-structure exceeds the LIDT of bulk silica. The LIDT of bulk silica is taken to be 100 J/cm^2 at 1030 nm for a 8 ns pulse [177]. Experimental work on micro-structured hollow-core fibres suggests that this is a conservative limit, with up to 3x higher values being reported in experimental work [154].

The dashed red lines in Fig. 5.12 show the LIDT of Designs 1 and 2 as the focus and alignment is modified with nanosecond and picosecond pulses, respectively. The maximum 10 ns pulse energy for Design 1 at optimal coupling is 230 mJ, a peak power

of more than 20 MW. Due to the low glass overlap, the LIDT of the NANFs is well above the achievable power from CW lasers. Therefore, the case of pulsed lasers, that produce significantly higher peak powers, is studied here. The LIDT behaves significantly differently to what might be expected in solid-core fibres since the peak optical intensity in the core does not damage the micro-structure. In Fig. 5.12(a,b) the damage threshold increases dramatically as the laser is more tightly focused since the intensity is reduced at the core/cladding interface. For Design 1 the maximum 10 ns pulse energy at $w_0/R = 0.5$ is 100 mJ, at $w_0/R = 0.45$ it is 500 mJ and at $w_0/R = 0.4$ it is more than 4 J. Additionally, there was little improvement from higher M^2 beams that have a more flat-top profile since by far the dominant effect was that of focus. This means that the practical damage threshold can be significantly increased in MM ARF compared to few-mode or single-mode fibres since with more modes, tighter laser focus is possible while maintaining high coupling efficiency. This is evident in Fig. 5.12(a) which shows that the maximum pulse energy for 10 ns pulses at optimal coupling is 230 mJ but by decreasing the laser focus by just 7 %, the coupling is still above 95 %, but the maximum pulse energy before damage increases by almost a factor 3x to 650 mJ. For comparison, a very high-energy nanosecond laser is chosen emitting at 1060 nm wavelength with a reported beam M^2 suitable for coupling to this fibre. The commercially available IPG Photonics YLPN has a maximum pulse energy of 10 mJ with a duration of 30 ns and requires a solid-core delivery fibre with a core diameter of 400 µm (more than 5x larger than that of Design 1) [175]. Even at optimal coupling the maximum pulse energy is already more than an order of magnitude higher than the YLPN and other typical nanosecond pulse lasers [147].

Figure 5.12(b) shows the LIDT of Design 2 when delivering 10 ps pulses. The maximum pulse energy before damage of Design 2 at optimal coupling is almost 20 mJ. The high energy, commercially available, Trumpf TruMicro 2070 picosecond laser has a maximum pulse energy of 500 µJ [176]. From this data it is indicated that suitably designed MM ARF fibres would be capable of handling the typical powers used in most applications and laser sources currently available, with considerable margins for further laser power up-scale.

Finally, as one might expect, Fig. 5.12(c,d) show that the damage threshold decreases as alignment offset increases; for Design 1 a misalignment of 15 % of the core radius results in almost an order of magnitude decrease in damage threshold. If large misalignment tolerances are required it may be therefore necessary to tighten the laser focus to maintain the damage thresholds.

5.2.3.4 Impact of dispersion on short pulse delivery

The delivery of nanosecond and picosecond pulses requires that the dispersive properties of the fibre are considered, as these may induce significant pulse

broadening, thus lowering the output peak power and distorting the temporal profile of the pulses. Both dispersion and DGD increase approximately linearly with mode order (see Section 5.1.1). Figure 5.13 shows the chromatic dispersion and DGD of the highest order modes of Designs 1 and 2. Design 2 guides more modes than Design 1, and this would increase both its maximum DGD and dispersion. This is however offset by the larger core which commensurately decreases both values. It follows therefore that both designs offer similar values of maximum DGD and dispersion for the high order mode with the highest loss.

The two cases described in the previous section are considered: 10 ns pulses propagating in Design 1 and 10 ps pulses propagating in Design 2. When calculating dispersion, it is assumed that all power is propagating in the highest order mode which constitutes the worst possible case. The dispersion experienced by a short pulse will depend on the precise coupling conditions and, if present, inter-modal power coupling along the length of the fibre. However, the case of uncoupled modes with the greatest DGD which is considered here represents again a worst-case scenario.

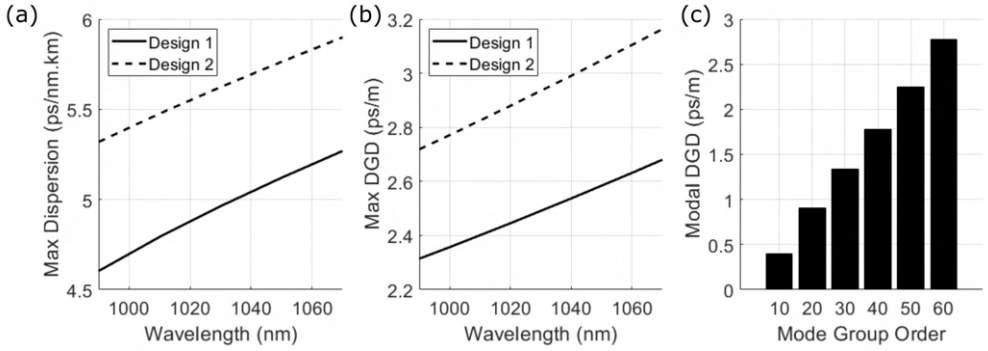

FIGURE 5.13: For the highest order modes of Design 1 and 2 (a) the dispersion parameter, D, and (b) the differential group delay as a function of wavelength. (c) the DGD of every tenth mode group in Design 2 at 1030 nm.

The dispersion length, Eq. (2.22), is defined as the distance over which the duration of that pulse increases by a factor of $\sqrt{2}$. For a 10 ps pulse in Design 2 the dispersion length is over 3 km for the highest order mode whilst for a 10 ns pulse the value is 6 orders of magnitude larger. Clearly chromatic dispersion will not have a significant impact on propagation.

Considering DGD, the dispersion length, $L_{DGD} = \frac{\tau_0(\sqrt{2}-1)}{|DGD|}$ is defined for a square wave of duration τ_0 with 50 % of power in the fundamental fibre mode and 50 % power in the highest order mode as the distance over which the duration of that pulse increases by a factor $\sqrt{2}$. For Design 1 a 10 ns pulse has $L_{DGD} = 1.7$ km. A 10 ps pulse propagating in Design 2 has $L_{DGD} = 1.4$ m. Although this is a worst-case scenario estimation, the DGD will clearly be the limiting factor for delivering high-power, low beam quality pulses of picosecond duration in MM ARFs. The DGD can be reduced in ARF by increasing the size of the core or by reducing the number of modes in which

power is guided. Figure 5.13(c) shows the DGD in Design 2 of every tenth mode group relative to the fundamental mode (other groups are omitted for clarity of reading). The dependence on mode order is approximately linear. Picosecond duration pulsed lasers generally have lower M^2 values than what has so far been assumed. Therefore, considering instead a 10 ps pulse with $M^2 = 3$, very similar to [164], then more than 95 % of the power is coupled into the first 10 mode groups. Taking the DGD as that of the tenth mode group then $L_{DGD} = 10.5$ m, comparable to the maximum lengths of typical solid-core power-delivery fibre. Despite the high DGD compared to solid-core fibres, MM ARF permits order of magnitude higher damage thresholds and more flexible fibres due to the low bending loss, < 2.5 dB/km at 35 cm bend radius, and smaller core size, eg Design 1 has a 5x smaller core than comparable fibres for nanosecond delivery [175].

5.2.4 Discussion

In this section the potential of MM ARFs for high-power fibre-delivery of few- and multi-moded laser sources has been investigated. As an example, two MM NANFs were designed for use with beams of $M^2 = 3$ and 13. Both fibres can provide $> 95\%$ coupling efficiency to their multi-mode laser inputs. Besides, both can deliver power with negligible leakage loss whilst tolerating bends with radii under 35 cm and seem capable of multi-km flexible laser delivery with little loss. Delivery of 10s of kW power over multi-km distances presents several opportunities in novel and existing applications. Examples of these include: subsurface rock drilling for the extraction of gas and oil [178] or situations, such as nuclear decommissioning, where the laser processing target is difficult or hazardous to access [179]. Equally, in existing factory machining applications, such long distance delivery offers greater flexibility; high-power lasers, and their associated power and cooling requirements, could be physically removed from the production line. In applications demanding shorter distances, the size of the core can be reduced without sacrificing coupling efficiency. For example if Design 1 were modified to have a 60 µm core diameter it would still be capable of delivering an $M^2 = 3$ beam with < 0.5 dB loss over at least 100 m whilst also increasing the flexibility of the fibre.

The damage threshold of the fibres considered here are between 20x and 40x greater than current typical requirements of nanosecond and picosecond pulses and can be increased significantly further if the fibres are designed to guide more modes. The DGD of the highest order modes is likely to limit the reach of picosecond pulses to 10 m but this can be mitigated by increasing the core size (see Section 5.1.1), although this may reduce the degree of bending the fibre can tolerate.

This work demonstrates that MM ARFs are capable of delivering radiation from high-power laser sources with large M^2 beams over significantly larger distances and

with greater power damage thresholds than current solid-core fibres and do so with similar or improved flexibility.

5.3 Multi-mode ARF sensing applications

The interaction between light and gas or liquid provides a variety of tools, e.g. absorption spectroscopy, photothermal effect or Raman scattering, by which it is possible to analyse the composition of that matter. Gas detection systems based on these effects have become widespread in a wide variety of applications such as environmental monitoring, and industrial processes. The sensitivity of these systems relies on strong light-gas interaction but free space systems are severely limited in interaction length whilst also suffering from stability issues [180]. Hollow-core fibres allow very-long interaction lengths with $> 99\%$ of light propagating in the gas medium. Further, fibre based systems permit distributed sensing over the long fibre length or very compact systems with long fibre lengths packaged in small coils. A significant limitation to the maximum interaction length and minimum system size is the straight and bending loss of the fibre. ARFs are therefore promising due to the very low losses that are possible.

The majority of research into sensing applications using ARFs has used single-mode fibre e.g. [181–183], indeed the high modal purity and low dispersion possible in single-mode ARF are often highly beneficial. There are however several uses for multi-mode fibre in sensing. Few-mode ARFs have, for example, been investigated for distributed stress sensing [48]: the perturbation caused by external stress causes inter-modal coupling that is measured by performing a modal decomposition of the light at the end of the fibre. In addition, the most sensitive photothermal gas sensors are based on inter-modal interferometry in dual-mode ARFs [46] with such systems demonstrated with parts per trillion trace gas sensitivity [47]. This list is not intended as an exhaustive review but to indicate some of the possibilities with MM ARFs.

In this section a novel use of MM ARF is chosen to study: gas detection by spontaneous Raman scattering. Light scattering originates from small-scale, random density variations which lead to local changes in the permittivity distribution. In Rayleigh scattering the interaction with the medium is elastic and therefore the incident and scattered light are the same wavelength. Raman scattering is inelastic and results in a frequency shift characteristic of the chemical structure of the medium. By collecting the light scattered from a pump beam, information can be discerned about the presence and abundance of Raman-active materials [184] or to perform distributed temperature sensing [185]. Stimulated Raman scattering is a technique that can result in strong signal power but requires a more complex setup with multiple laser sources depending on the number of gas species interrogated.

Spontaneous Raman scattering, by contrast, allows a simpler setup with a single pump laser able to perform multiple gas species detection. The signal power is typically very weak, however, which limits the detection threshold. The long gas-light interaction length possible in hollow-core fibres makes them a natural choice for this application e.g. [184, 186, 187] but longer fibre lengths result in other limitations such as longer gas filling times [188]. In this section, it is investigated how multi-mode guidance can increase the Raman signal without increasing the fibre length.

5.3.1 Increased Raman scattering in multi-mode ARF

Multi-mode fibres have a larger numerical aperture than single-mode fibres which suggests the capability to capture a larger fraction of scattered light and improve the Raman signal. Numerical aperture is not well defined for anti-resonant fibres and instead, it is considered how the modes of ARF are excited by the scattering of light. The volume-current method has previously been used to study Rayleigh scattering by Numkam Fokoua *et al.* [189]. If the modes of a fibre, described by their electric field profile **E**, are normalised according to Eq. (2.16), then the fibre scattering coefficient per unit length from mode k into mode l is given by:

$$B_{\mathrm{kl}} = \frac{6\pi}{k_0^4}\omega^2\epsilon_0^2\alpha_R \iint |\mathbf{E}_k \cdot \mathbf{E}_l^*|^2 dA \tag{5.8}$$

where α_R is the bulk Rayleigh scattering coefficient. The fraction of scattered light that is captured depends on the overlap integral between the modes in which the incident and scattered light propagates. The magnitude of the Raman scattering coefficient will be different and specifically will depend on the gas species, pressure and temperature, otherwise however, the behaviour is very similar [185]. In this work the same theory is employed to determine the scattering coefficient of Raman scattering.

A multi-mode tubular fibre is chosen to study similar to multi-mode fibres previously reported in literature [49]. A cross section of the design is shown in Fig. 5.14(a) which has a core diameter 56 µm, wall thickness 530 nm and gap size 5 µm. The modes of the fibre were calculated by numerical simulation. The bandwidth of the fundamental window in ARFs is typically wide enough to accommodate detection of multiple gas species [184]. The modes of interest will therefore not behave significantly differently at the wavelengths of the pump and signal and without loss of generality only a single operational wavelength is considered: near the centre of the fundamental anti-resonant window, with normalized frequency $F = 0.61$, where the fibre guides 5 low-loss mode groups.

In Fig. 5.14(b) the Raman scattering coefficient is calculated for the first 5 mode groups using Eq. (5.8). The calculation is performed assuming pump light is launched into

either the LP_{01} or LP_{11} mode group. Since the scattering coefficient depends on the gas species and pressure via α_R, the plot is relative to B_{00}, the scattering per unit length of the fundamental mode into the fundamental mode. Thereby the potential for HOMs to be excited by Raman scattered light is compared to a single-mode fibre for any gas species and pressure. Considering a fundamental mode launch, the LP_{11} mode group captures 1.3x the power compared to the LP_{01} mode group whilst the LP_{21} captures approximately equal power and the LP_{02} and LP_{31} mode groups capture approximately 0.8x. This suggests that multi-mode guidance can significantly increase the detectable Raman signal. The case of 100% pump power launched into the LP_{11} mode is also considered. This is not a common scenario but is used to understand the behaviour if there is transverse offset in the pump laser launch alignment which would cause excitation of the LP_{11} mode group. In Fig. 5.14(b) the fibre scattering coefficient of the HOMs for LP_{11} launch is comparable to a LP_{01} launch when taken as an average although the power captured by the LP_{01} mode is less than 0.7x that of a LP_{01} launch. This suggests that there is a high tolerance for transverse offset in the launch conditions.

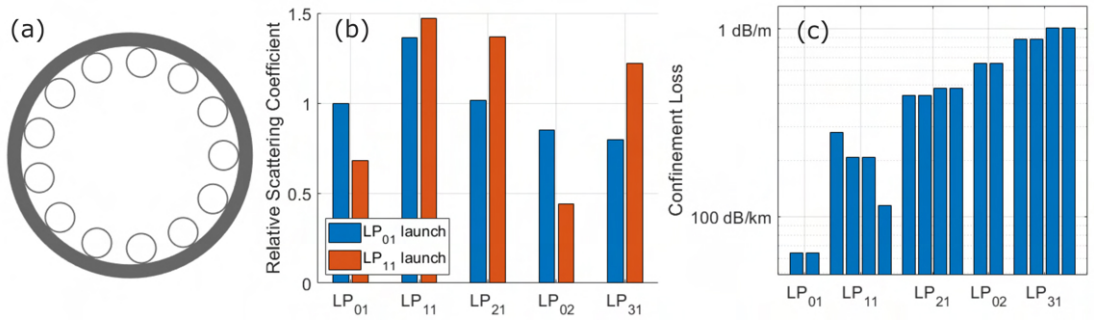

FIGURE 5.14: (a) The cross section of a the 5-mode group tubular fibre considered for Raman sensing. (b) The Raman modal scattering coefficients of the first 5 mode groups of the fibre with either LP_{01} or LP_{11} pump launch. Scattering coefficients are relative to the LP_{01} mode group. (c) The modal leakage loss of the fibre.

Although HOMs capture a significant fraction of the scattered Raman light, they also suffer from increased attenuation compared to the fundamental mode. Shown in Fig. 5.14(c) is the modal confinement loss of the fibre. The 5 mode groups of interest are guided with less than 1 dB/m loss. The loss of the fundamental mode is over an order of magnitude less, 64 dB/km. The average loss of the LP_{11} mode is three times that of the fundamental, 200 dB/km.

5.3.2 Detection of Raman signal

To understand how increased attenuation affects the detection of Raman signal from the HOMs an expression is determined for the received Raman signal power in both backscatter (with the detector at the same end of the fibre as the pump light launch) and forward-scatter (the detector at the opposite end of the fibre) configurations. In a

backscatter configuration, for an infinitesimal length dz of fibre at a distance z from the launch end of the fibre, the returned power from mode l when the pump is launched into mode k is given by $P_0 \exp(-2\alpha_k z) B_{\mathrm{kl}} \exp(-2\alpha_l z)\mathrm{d}z$. In this expression P_0 is the pump power at launch and α_k is the field attenuation of mode k. In this analysis Raman scattering is assumed to be negligible compared to confinement loss: $\sum_l B_{\mathrm{kl}} \ll \alpha_k$ where the sum extends over all fibre modes. Integrating this expression over the length of the fibre, L, yields the power returned over the length of the fibre:

$$P_b^{(\mathrm{kl})} = \frac{P_0 B_{\mathrm{kl}}}{2(\alpha_k + \alpha_l)} \Big[1 - \exp(-2(\alpha_k + \alpha_l)L)\Big] \tag{5.9}$$

In a backscatter configuration the returned power increases with the length of the fibre, tending towards an asymptotic maximum proportional to the pump power and modal scattering coefficient and inversely proportional to the sum of the attenuation of the pump and signal modes. In Fig. 5.15(a), Eq. (5.9) is used to calculate the returned Raman signal power of the previously described fibre given a LP_{01} pump launch. The resulting power is shown when the contributions of different modes are included. Signal power is measured relative to the asymptotic maximum of a single-mode fibre, $P_0 B_{00}/4\alpha_0$ to compare performance of single-mode and multi-mode fibre. For long lengths, i.e. $L \gg 1/4\alpha_0$, including the LP_{11} mode group results in 1.6x greater signal power. With the 4$^{\mathrm{th}}$ mode group signal power is improved 2x compared to the single-mode case but the 5$^{\mathrm{th}}$ mode group only results in a 2.1x increase. Extra signal power in HOMs is more significant for shorter fibre lengths. Over 10 m, compared to single-mode, the signal from 2 mode groups is doubled and including all 5 mode groups the increase is almost 4x. Also considered is the power returned given a LP_{11} pump launch. Again, this is an unlikely scenario but is used to demonstrate the effects of transverse misalignment in the pump launch. Although the modal scattering coefficients for an LP_{11} launch are comparable to a fundamental mode launch, Fig. 5.14(b), due to the higher losses of the LP_{11} mode group the returned signal power is capped to roughly half the power of a fundamental mode launch. If the length of the fibre is short, misalignment in the launch will not have a significant impact but will limit the maximum signal power for longer fibre lengths.

The Raman signal in a forward-scatter configuration was also determined. Having the detector at the opposite end of the fibre to the pump launch hardware can reduce the complexity of the setup. Similarly to the backscatter case, the power from an infinitesimal length of fibre is $P_0 \exp(-2\alpha_k z) B_{\mathrm{kl}} \exp(-2\alpha_l (L - z))\mathrm{d}z$ and integrating over the length of the fibre, the modal signal power in a forward-scatter configuration is derived:

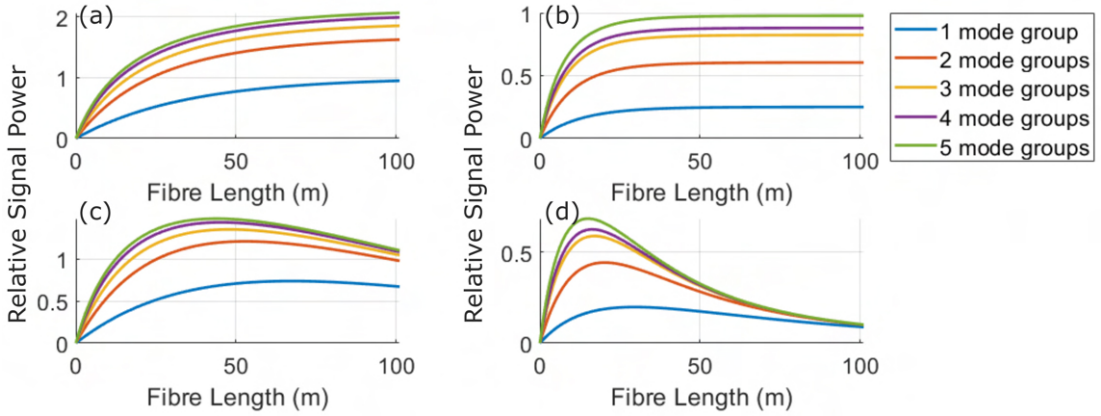

FIGURE 5.15: Returned Raman signal power as a function of fibre length. In (a,b) consider backscatter configurations and (c,d) consider forward-scatter configurations. (a,c) assume pump light launched into the LP_{01} mode and (b,d) assume 100% LP_{11} mode launch.

$$P_f^{(\mathrm{kl})} = P_0 B_{\mathrm{kl}} \exp(-2\alpha_l L) \cdot \begin{cases} L & \text{if} \quad k = l \\ \frac{1}{2(\alpha_k - \alpha_l)} \left[1 - \exp(-2(\alpha_k - \alpha_l)L)\right] & \text{otherwise} \end{cases} \tag{5.10}$$

Unlike the backscatter configuration, when collecting forward scattered light the signal power increases to a maximum with increasing length and decreases as length is further increased. For the fundamental mode the maximum occurs when $L = 1/2\alpha_0$. The captured forward-scatter Raman light as a function of fibre length is shown Fig. 5.15. To maintain the comparison, power is again plotted relative to the maximum of a single-mode fibre in a backscatter configuration. Whilst signal powers are comparable to the backscatter case for very short fibre lengths, $L < 20$ m, the peak power is lower and longer fibre lengths return even smaller signal powers. The relative improvement from including higher-order modes is similar to the backscatter case: 4 mode groups results in approximately double the peak Raman signal of a single-mode fibre. The peak in multi-mode guidance occurs at shorter fibre lengths due to the higher losses e.g. the maximum for 4 mode groups is at 44 m compared to 62 m in a single-mode fibre. When launching pump power into the LP_{11} mode group the behaviour is similar to the backscatter configuration: similar signal power for short lengths but maximum power is limited to approximately half that of a fundamental mode launch.

5.3.3 Discussion

Multi-mode ARF has the potential to significantly increase sensitivity of gas sensors based on spontaneous Raman scattering. The 5-mode group fibre studied,

geometrically similar to previously fabricated MM ARF, was capable of more than doubling the signal strength of a comparable single-mode ARF. This increase was limited by the increased attenuation of the HOMs so by reducing the differential loss, e.g. by using a NANF structure, significantly higher signal powers would be achievable.

No modification to the pump launch is necessary, with single-mode launch still optimal, although excitation of HOMs due to transverse offset in the launch will not have a significant impact on performance. Likewise, if signal light is delivered to the detector directly from the ARF or via a MM patch cord, no modification to the detector setup is required. The benefits of MM guidance are achieved purely by design of the fibre with no additional complexity in the system. Some limitations may arise due to the DGD inherent in MM ARFs if, for example, short pulses are employed in the pump laser but due to the relatively short lengths typically employed (typically 10s of metres [184]) this is not expected to have a significant impact. This work suggests that multi-mode ARFs are ideal for spontaneous Raman scattering based gas detection.

5.4 Summary

The potential of anti-resonant multi-mode fibre for applications in short-reach datacomms, high-power laser delivery and spontaneous-Raman based fibre gas sensors, has been investigated. Whilst differential group delay is very limiting for data transmission, the fibres show great promise for power delivery and gas sensing owing to their ultra-low nonlinearity, high damage threshold and low-loss multi-mode guidance. The evidence presented in this chapter compellingly shows the potential of multi-mode guidance in anti-resonant fibre in real-world applications and further applications are expected to be found in the future.

Chapter 6

Conclusions

The work presented in this thesis has produced a greater understanding of the behaviour and potential applications of multi-mode anti-resonant fibres. The conclusions of this work are summarised in Section 6.1. A proposal for future work indicated by this research is given in Section 6.2. Finally, some concluding remarks are given in Section 6.3.

6.1 Summary of the chapters

In Chapter 3 the origins of differential modal leakage loss were investigated in tubular multi-mode ARF using numerical simulations. It was shown, for low-loss fibres, that the leakage loss for the core modes can be strongly linked to the cladding tubes themselves. In fact, quantifying the coupling between core modes and cladding air modes guided in the cladding tubes showed a strong correlation with leakage loss. Other air-guided cladding modes, as well as dielectric cladding modes, had a negligible impact on the loss in low-loss regimes.

Understanding leakage loss in terms of out-coupling power to cladding modes allowed the loss to be described approximately in terms of the strength of coupling between core and cladding modes. The crucial quantity that drives the strength of coupling from core modes to tube modes and thus loss, is the separation between the propagation constants of the core and cladding tube modes which can be readily determined from the geometry. When exactly phase matched, core modes suffer leakage loss as high as that of the cladding modes themselves. From this, a model for leakage loss was developed based on resonant coupling to tube modes; by considering only the contributions of the first three cladding tube modes the model showed good agreement to numerical simulation. With this knowledge, the concept of phase-mismatch windows, analogous to anti-resonant windows, was devised. This

concept was used throughout the thesis to design and understand the behaviour of ARFs.

Next, in Chapter 4, several different ARF designs were investigated using numerical simulation with the aim of achieving low-loss, few-moded guidance. A fixed core radius of 25 µm was chosen to target existing multi-mode short-haul telecomms link standards and to better understand the behaviour of different cladding designs. In NANFs the number of low-loss modes is increased by increasing the number of cladding tubes. This, however, also reduces the separation between the jacket glass and the core, increasing the loss of all core modes. The various cladding modes in both NANFs and DNANFs, which govern the loss of HOMs, were identified. By studying the behaviour of these modes using numerical simulation, a technique was developed for designing the cladding of NANFs and DNANFs to maximise multi-mode performance. Importantly, this technique does not require time-consuming numerical simulation and demonstrates a high degree of accuracy, greatly aiding the design of multi-mode NANFs and DNANFs.

Looking beyond NANFs and DNANFs, the multi-mode performance of ARFs geometries with 2 or more adjacent, nested capillaries in the ALIF configuration was assessed. These structures were capable of impressive HOM loss reduction. The effect of additional glass nodes in close proximity to the core, however, caused significant spurious glass resonances which would likely prevent low-loss operation. The ALIF design still showed promising results and was studied in greater detail. Using targeted numerical simulations, a model was developed for predicting the effective index of the unique cladding modes of an ALIF. This model, which does not require numerical simulation, showed good agreement with numerical simulations and was used to design ALIFs for multi-mode short-haul applications. Numerical studies showed that the designed ALIF is capable of guiding 7 mode groups with lower loss than the current OM5 solid-core standard fibre with more than double the bandwidth. Further studies, however, indicated that differential group delay could severely limit the achievable single-channel data rates.

This is investigated further in Chapter 5. It is shown analytically, and confirmed with numerical simulation, that whilst both GVD and DGD can be reduced with a larger core, DGD remains significant for practical fibres. Although the methods of reducing DGD in solid-core fibre are not possible in ARF, alternatives were investigated. It is shown by numerical simulation that bending can powerfully reduce the DGD: the fibres considered showed up to a factor 2 reduction. Increased attenuation from bending can be tolerable but more important are the practical considerations of enforcing a fibre bend whilst routing cables which would seem to greatly impair the purpose of optical fibre and make this approach unfeasible. As a possible alternative in-built twisting was investigated. This is a modification that can readily be incorporated into the fabrication process and was studied as a possible means of

reducing DGD. A method was developed for simulating ARFs with a constant rate of twist but numerical studies indicated this technique did not have the desired effect; instead a small increase in DGD was exhibited. The conclusion drawn is that, for the purposes of existing VCSEL-based short-haul datacomms, despite large bandwidth, low loss and low latency, prohibitively high DGD make MM ARF unsuitable as an improvement of current graded-index solid-core fibres. This does not altogether preclude MM ARF from datacomms applications, with inter-modal dispersion resistant modulation formats and digital compensation methods a possibility over the larger bandwidth available in ARF. Single-mode laser sources have been adopted in many data centre applications and, for those sources, single-mode ARFs remain a very promising option.

Next, another potential application of MM ARFs is investigated in high-power fibre-delivery of few- and multi-moded laser sources for industrial machining. The number of modes required to be guided for efficient coupling to multi-mode lasers of a given M^2 beam quality was determined. Lasers with M^2 up to 15 are considered; current commercial lasers with similar beam qualities are capable of producing up to 10 kW. As an example, two MM NANFs for use with beams of $M^2 = 3$ and 13 were designed. By numerical simulation it was shown that both fibres are capable of delivering power with negligible leakage loss whilst tolerating bends with radii under 35 cm and seem capable of multi-km flexible laser delivery with little loss. Maximum power in ARFs with ultra-low nonlinearity will likely be dictated by the threshold of optical damage to the micro-structure cladding. In ARFs it is shown that the most significant factor in determining damage threshold is the focus of the incident laser beam. The damage threshold of the fibres considered in this thesis are between 20x and 40x greater than current typical requirements of nanosecond and picosecond pulses and can be increased significantly further if the fibres are designed to guide more modes.

Finally, a theoretical investigation was presented aimed at increasing the signal power in gas sensors based on spontaneous Raman scattering. It is shown that multi-mode ARF have the potential to significantly increase sensitivity of such systems. A 5-mode group fibre, geometrically similar to previously fabricated MM ARF, was studied numerically and shown capable of more than doubling the detected signal strength of a comparable single-mode ARF. This increase was limited by the increased attenuation of the HOMs, so by reducing the differential loss, e.g. by using a NANF structure, significantly higher signal powers would be achievable. No modification to the pump launch is indicated and, if signal light is delivered to the detector directly from the ARF or via a MM patch cord, then likewise no modification to the detector setup is required. This work suggests that multi-mode ARFs are ideal for spontaneous Raman scattering based gas detection.

6.2 Future work

Several avenues for future work are indicated by the research presented in this thesis. Firstly, although I believe the analysis presented and model developed in Chapter 3 are a significant step towards a robust model of leakage loss in both single- and multi-mode ARF, there remains a great deal of work still to be done. One suggestion would be to incorporate the effects of, in addition to the cladding tube modes, other modes guided within the cladding. Prime examples are: the dielectric modes, as studied by Vincetti *et al.* [111], which become significant as the edges of the anti-resonant window are approached; and the air-modes guided in the interstitial region between tubes which Chapter 4 suggests are significant for multi-mode DNANFs. In addition, further study of the overlap integral between core and cladding modes as a function of phase mismatch, which itself follows a Lorentzian-like behaviour, would likely yield further insight and a simplification of the model. These improvements could also be applied to the study of loss in other ARF geometries of interest: namely the NANF and DNANF for which models of cladding tube modes were developed in Chapter 4.

As mentioned above, models for the cladding tube modes in NANFs, DNANFs and ALIFs were developed in Chapter 4, which proved invaluable for the task of designing multi-mode ARFs based on NANFs and ALIFs. I believe that the model for DNANFs could be improved further. Recent results suggest the DNANF will prove to be a significant ARF design and since this structure affords a great deal of control over the individual modes, a more nuanced model predicting individual tube modes would be very useful, particularly, for example when including the effects of bending.

The work presented in Chapter 5 involved large-core multi-mode NANFs which had a significant fraction of power coupled into low-order modes. In this regime the overall leakage loss was calculated to be nearly negligible which suggests that, for such large-core fibres, microbending would play a significant role in loss. To my knowledge, no research has been undertaken studying inter-modal coupling in multi-mode ARFs and in particular no experimental data exists with which to validate any theoretical work. Nevertheless, a theoretical analysis of the interaction between core modes would seem to be a very useful undertaking to better understand the behaviour of such multi-mode fibres, particularly if they are to be assessed for use in MDM telecommunications.

Finally, whilst the purely theoretical study of multi-mode ARFs permitted analysis of a wide range of topics and applications in the available time frame, experimental validation of the findings is clearly needed. The logical next step, building on promising results presented in this thesis, such as in power delivery and Raman sensing, is to fabricate multi-mode ARF designs and experimentally validate these results.

6.3 Concluding remarks

This project has resulted in new understanding and insight into the vast and hitherto largely unexplored topic of low-loss multi-mode anti-resonant fibres. With the huge potential of anti-resonant fibres now beginning to become apparent by the ground-breaking work of groups such as the Optoelectronics Research Centre, the University of Bath, the Limoges and CREOL groups, as well as other groups around the world active in this research field, it is apparent that multi-mode ARF, like single-mode ARF, is likely to have a decisive impact on the field of fibre optics in the decades to come. It is hoped that the reader has developed a greater understanding of the complex behaviour of multi-mode ARFs, has come to learn some of their myriad applications in varied fields and perhaps has been inspired to imagine some of their own.

Appendix A

An Overview of Simulation Work to Support Fabrication Efforts

One significant component of the work undertaken in the course of this doctoral project, not described in the body of this thesis, is that of supporting experimental work undertaken in the Optoelectronics Research Centre (ORC). In particular, several simulation studies were conducted of fabricated NANFs to aid their characterisation and to inform the design of future fibres. This involves unpublished experimental results gathered by colleagues at the ORC which cannot be shown. Nevertheless, a brief overview of some of the activities I have conducted during this project that, for example, supported the research published in Ref [59], will be presented here.

Despite remarkable progress both theoretically and practically [11, 22, 27–29], fabrication of anti-resonant fibre remains, so far, an imperfect process. Throughout this thesis, fibres have been modelled as ideal structures but real fabricated fibres will have variation in the thickness of the capillary walls and the position and size of capillary tubes. There may also be introduced enlarged glass nodes at the welding points between tubes and the jacket glass. All of these features can significantly impact the loss and understanding their impact is important to inform what modifications to the fabrication process should be made to best improve the fibre's performance. Numerical simulation provides a means of doing just this.

A scanning electron microscope (SEM) can be used to image the cross section of a fabricated optical fibre. Bespoke algorithms developed by Gregory Jasion, a researcher at the ORC and supervisor of this doctoral project, use this SEM image in combination with macroscopic measurements of the fibre preform (see Section 2.2.3 for an overview of the fabrication steps) to produce a geometric description that closely resembles the fabricated fibre. This was enhanced in the course of this project with a tool which can modify the size of glass nodes, allowing a better manual fit of the

geometry to the SEM image or providing the opportunity to test the effects of increased or decreased glass nodes.

The results of numerical simulations using these techniques is presented in the next section.

A.1 Determining contributions of different loss mechanisms

Figure A.1(a) shows the results of numerical simulation of a fabricated single-mode NANF. The geometry of this NANF is not shown for the reasons described above. This NANF targets the C and L telecommunication bands at 1550 nm in the second anti-resonant window and the 1 µm laser wavelength in the third anti-resonant window. Around 0.8 dB/km is predicted in the second window and 1 dB/km in the third. Using numerical simulation it is possible to separate the contributions of the different loss mechanisms (see Section 2.3.4). Figure A.1(a) shows leakage, surface scattering, micro- and macro-bending. In the fundamental and second anti-resonant window, leakage for this fibre is dominated by leakage loss. At the shorter wavelengths of the third anti-resonant window, loss is instead dominated by micro-bending losses.

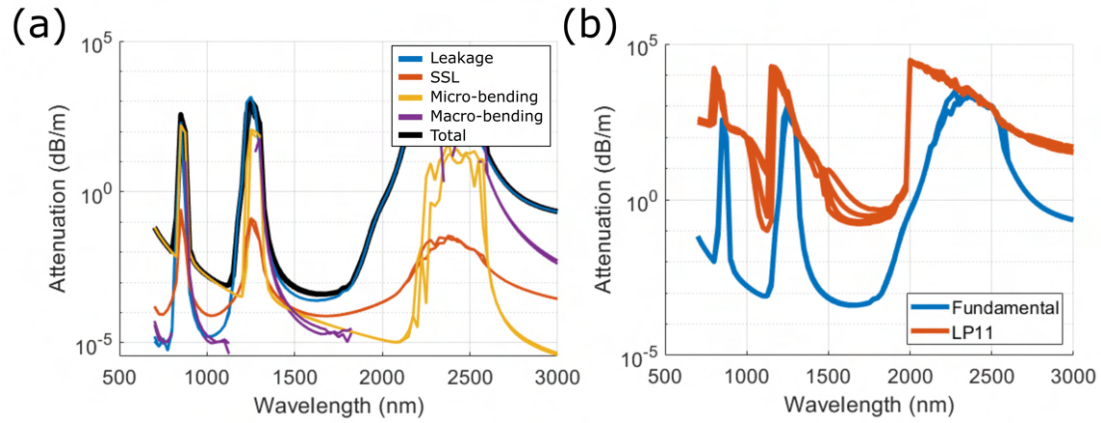

FIGURE A.1: Results of numerical simulations showing (a) the loss contributions from leakage, scattering, micro- and macro-bending and (b) the differential loss between the fundamental LP_{01} and LP_{11} mode groups in a fabricated single-mode NANF.

The numerical simulation for this fibre showed excellent agreement with experimental cutback measurements (once more, not shown here). The numerical simulation therefore indicates how the draw conditions can be modified to improve the fibre performance. To optimise for low-loss at 1550 nm, a larger core size is indicated which will reduce leakage loss [10]. At 1000 nm the opposite is required, with smaller cores leading to reduced micro-bending losses [84]. How targeting a smaller or larger core will affect the other geometric parameters (e.g. smaller/larger inter-tube gaps) when drawing from the same cane can also be determined from the drawing principles.

Since the effect on loss of changing multiple geometric parameters can be complex, further numerical simulations can be conducted of the projected, modified geometry.

In other cases the numerical simulation does not show good agreement with experimental results. Often this is the result of geometric defects or gradual geometric variation along the length of the fibre which cannot be determined from the SEM image alone. A comparison with the numerical simulation can again provide insight into the nature of these geometric defects or variations (other, more complex, experimental techniques can provide greater insight, e.g. optical time domain reflectometry). One example of this is where the edges of the anti-resonant windows found experimentally do not match those predicted by simulation which suggests that the thickness of the capillary walls varies along the length of the fibre. The extent of this effect can be estimated by comparing the two results using, e.g. Eq. (2.24).

Another useful facility of numerical simulation is to predict the loss of higher-order modes, and therefore the HOM extinction ratio, a crucial quantity in single-mode ARFs. This is a much more complex quantity to measure experimentally, compared to the loss of the fundamental mode. Figure A.1(b) shows the total loss predicted by numerical simulation of the fundamental and LP_{11} mode groups in the same fabricated fibre. The loss of the LP_{11} mode group is over 100x higher than that of the fundamental mode in the second anti-resonant window suggesting effective higher-order mode stripping in this fibre.

Appendix B

Finite-element Simulation of Twisted Fibres

This appendix describes a technique, using a transformation optics approach, to numerically simulate twisted optical fibres using the finite-element method in the *COMSOL* software. This technique is used in Chapter 5 to investigate the effect of a built-in twist on differential group delay between modes of multi-mode anti-resonant fibre. An introduction to the transformation optics approach is presented and the equations describing the transform between twisted and regular Cartesian coordinates are derived. Further considerations for understanding the results of this technique are presented. Finally, the implementation of a PML in the twisted frame is derived.

B.1 Transformation optics

Transformation optics is a technique that allows Maxwell's equations to be solved in a non-Cartesian coordinate system without changing their definition [190]. It entails encapsulating the change of coordinate into a material transform. In optics we are commonly working with isotropic materials for which the permittivity and permeability are scalars. For transparent materials they are also real. In general however they are complex tensors which allows them to encapsulate a change of coordinate. If that change of coordinate allows a fibre to be described in a translationally invariant way then transformation optics can be used to solve for that fibre in 2-dimensions. This works well for a Finite Element solver with support for anisotropic materials.

If a geometry is expressed in one coordinate system $\{u, v, w\}$ and we wish to transform that fibre into a second coordinate system $\{x, y, z\}$ then Jacobian matrix, $\mathbf{J}$, can be formed. Given $x(u, v, w)$, $y(u, v, w)$ and $z(u, v, w)$

$$\mathbf{J}_{xu} = \begin{bmatrix} \frac{\partial x}{\partial u} & \frac{\partial x}{\partial v} & \frac{\partial x}{\partial w} \\ \frac{\partial y}{\partial u} & \frac{\partial y}{\partial v} & \frac{\partial y}{\partial w} \\ \frac{\partial z}{\partial u} & \frac{\partial z}{\partial v} & \frac{\partial z}{\partial w} \end{bmatrix} \tag{B.1}$$

where the xu subscript denotes a change of coordinate from u to x, the reason for the change of order will become apparent shortly. Given the Jacobian the material equivalence becomes [191]:

$$\epsilon^{'} = \mathbf{J}^{-1}\epsilon\mathbf{J}^{-T}\det(\mathbf{J}) \tag{B.2}$$

$$\mu^{'} = \mathbf{J}^{-1}\mu\mathbf{J}^{-T}\det(\mathbf{J}) \tag{B.3}$$

where $^{'}$ denotes the new material tensor, $\mathbf{J}^{-1}$ is the inverse of the matrix and $\mathbf{J}^{-T}$ is the transpose of the inverse. In the case that the original ϵ and μ are scalars, Eq. (B.2) can be simplified to use a single transformation matrix, $\mathbf{T}$:

$$\epsilon^{'} = \epsilon\mathbf{T}^{-1} = \epsilon \cdot \left(\frac{\mathbf{J}^T\mathbf{J}}{\det(\mathbf{J})}\right)^{-1} = \epsilon \cdot \left(\mathbf{J}^T\mathbf{J}\right)^{-1}\det(\mathbf{J}) \tag{B.4}$$

and similarly for μ. A useful property of transformation optics is that multiple transformations can be concatenated together into a single transformation matrix. Given a series of coordinate systems: $\{u, v, w\}$, $\{X, Y, Z\}$, $\{x, y, z\}$ and the corresponding mapping functions: $x(X, Y, Z)$, $y(X, Y, Z)$, $z(X, Y, Z)$, $X(u, v, w)$, $Y(u, v, w)$, $Z(u, v, w)$ we can calculate two Jacobian matrices: $\mathbf{J}_{xX}$ and $\mathbf{J}_{Xu}$. The compound Jacobian becomes $\mathbf{J}_{xu} = \mathbf{J}_{xX}\mathbf{J}_{Xu}$ which can be determined using either Eq. (B.2) or Eq. (B.4). Note that the mapping functions are defined from the final coordinate system to the original whilst the Jacobian matrices are multiplied in the opposite order.

B.1.1 Twist transform

In order to simulate a twisted fibre we introduce a helicoidal coordinate system in which we can describe geometry in a twisted Cartesian frame. This system $\{\xi_1, \xi_2, \xi_3\}$ for a twist rate, α can be mapped to standard Cartesian coordinates by

$$\begin{aligned} x &= \xi_1\cos(\alpha\xi_3) + \xi_2\sin(\alpha\xi_3) \\ y &= -\xi_1\sin(\alpha\xi_3) + \xi_2\cos(\alpha\xi_3) \\ z &= \xi_3 \end{aligned} \tag{B.5}$$

Hence a geometry which is $2\pi/\alpha$ periodic in z becomes invariant in ξ_3. We must however be able to specify not only the geometry but also the material in a translationally invariant manner. We can derive the Jacobian for this transform

$$\mathbf{J}_{hel} = \begin{bmatrix} \cos(\alpha\xi_3) & \sin(\alpha\xi_3) & \alpha\xi_2\cos(\alpha\xi_3) - \alpha\xi_1\sin(\alpha\xi_3) \\ -\sin(\alpha\xi_3) & \cos(\alpha\xi_3) & -\alpha\xi_1\cos(\alpha\xi_3) - \alpha\xi_2\sin(\alpha\xi_3) \\ 0 & 0 & 1 \end{bmatrix} \tag{B.6}$$

which clearly does depend on ξ_3. However, given the rotation matrix $\mathbf{R}$

$$\mathbf{R}(\theta) = \begin{bmatrix} \cos\theta & \sin\theta & 0 \\ -\sin\theta & \cos\theta & 0 \\ 0 & 0 & 1 \end{bmatrix} \tag{B.7}$$

with the well known property that $\mathbf{R}^{-1}(\theta) = \mathbf{R}^T(\theta) = \mathbf{R}(-\theta)$, the Jacobian can instead be written as the product of a rotation and a translation

$$\mathbf{J}_{hel} = \mathbf{R}(\alpha\xi_3)\mathbf{M} = \mathbf{R}(\alpha\xi_3) \begin{bmatrix} 1 & 0 & -\alpha\xi_2 \\ 0 & 1 & \alpha\xi_1 \\ 0 & 0 & 1 \end{bmatrix} \tag{B.8}$$

from which the transform matrix from Eq. (B.4) becomes
$\mathbf{T}_{hel} = \mathbf{J}_{hel}^{-1}\mathbf{J}_{hel}^{-T}\det(\mathbf{J}_{hel}) = \mathbf{M}^{-1}\mathbf{R}(\alpha\xi_3)\mathbf{R}^{-1}(\alpha\xi_3)\mathbf{M}^{-T} = \mathbf{M}^{-1}\mathbf{M}^{-T}$ from which it can be shown that

$$\mathbf{T}_{hel}^{-1} = \begin{bmatrix} 1+\alpha^2\xi_2^2 & -\alpha^2\xi_1\xi_2 & -\alpha\xi_2 \\ -\alpha^2\xi_1\xi_2 & 1+\alpha^2\xi_1^2 & \alpha\xi_1 \\ -\alpha\xi_2 & \alpha\xi_1 & 1 \end{bmatrix} \tag{B.9}$$

which is clearly only dependent on ξ_1 and ξ_2. Hence transformation optics allows us to simulate a fibre with a constant rate of twist using only a 2-dimensional cross section and since the coordinate system is Cartesian we can describe the geometry exactly as in the untwisted case. Clearly if $\alpha = 0$ then T_{hel} becomes the identity matrix and our twisted frame becomes the regular Cartesian frame.

B.1.2 Post transform

It must be remembered when solving a twisted fibre using transformation optics that the solution is in helicoidal coordinates. A post-transform must be applied to return the results into regular Cartesian coordinates. For field quantities this is a simple matter of applying the inverse of the Jacobian [191]

$$\mathbf{E} = \begin{pmatrix} E_x \\ E_y \\ E_z \end{pmatrix} = \mathbf{J}^{-T} \begin{pmatrix} E_{\xi_1} \\ E_{\xi_2} \\ E_{\xi_3} \end{pmatrix} \tag{B.10}$$

and equivalently for the magnetic field, **H**. Considering the Jacobian for the helicoidal coordinates we can derive that

$$\begin{pmatrix} E_x \\ E_y \end{pmatrix} = \mathbf{R}(\alpha z) \begin{pmatrix} E_{\xi_1} \\ E_{\xi_2} \end{pmatrix} \tag{B.11}$$

At $z = 0$ the transverse components of the electric and magnetic fields in the untwisted frame are equal to those in the twisted frame. They then rotate at the rate of twist of the fibre as you move along the fibre axis. The longitudinal power flow, described by the Poynting vector, S_z, depends only on the transverse field components (Eq. (2.23)) and so also requires no post-transform at $z = 0$ [141].

Post-transforming the propagation constant and effective index is more complex. If we consider a wave in polar coordinates (r, θ, z) as in Eq. (2.13) and the same wave in twisted polar coordinates (r, ψ, z).

$$\mathbf{E}(r, \psi, z, t) = \mathbf{F}_l^{tw}(r) e^{-il\psi} e^{-i(\omega t - \beta^{tw} z)} \tag{B.12}$$

The field and propagation constant are different in the twisted frame, denoted by the ^{tw} superscript, but the azimuthal mode order l must be the same since in either coordinate system it is the same light propagating in the same fibre. The map from twisted to untwisted polar coordinates is simply $\psi = \theta - \alpha z$. Hence Eq. (B.12) can be rewritten

$$\mathbf{E}(r, \psi, z, t) = \mathbf{F}_l^{tw}(r) e^{-il\theta} e^{-i(\omega t - (\beta^{tw} + l\alpha) z)} \tag{B.13}$$

and by comparison with Eq. (2.13) the propagation constant in Cartesian coordinates is

$$\beta = \beta^{tw} + l\alpha \tag{B.14}$$

or for a full vectorial solution including the spin angular momentum, s, [141]

$$\beta = \beta^{tw} + (l + s)\alpha \tag{B.15}$$

Spin angular momentum, $s = +1$ and -1 for left and right circularly polarised modes respectively. Hence we can post-transform the propagation constant with knowledge of the azimuthal mode order and the polarisation of the solved mode.

B.1.3 Perfectly matched layer transform

A PML can be described as a map from the infinite, real-world domain to a finite one, the modelling space. It is therefore effectively a coordinate transform and can be implemented as such. Unfortunately this means additional care must be taken when applying a coordinate transform to a simulation which includes a PML. Transforms can be concatenated as described in Section 5.1.3.1 but in general this requires post- and pre-multiplication of the material tensor. The built-in PML of COMSOL cannot be extended to general coordinate transforms and therefore to use COMSOL for such simulations we designed and implemented our own helicoidal-coordinate, cylindrical PML.

With the theory of transformation optics the application of a PML becomes quite simple. Successive transforms can be used to move to cylindrical coordinates, apply a complex stretch factor to the radial coordinate and then return to Cartesian coordinates. The stretch factor, $s_r(r)$, must equal 1 in the simulation space and inside the PML generally takes on an increasing, complex value. We can then define the complex stretch coordinate transform from cylindrical coordinates (r, θ, z) to stretched cylindrical coordinates $(\tilde{r}, \theta, z)$

$$\tilde{r} = \int_0^r s_r(r')dr' \tag{B.16}$$

and the Jacobian for the complex stretch is

$$\mathbf{J}_{\tilde{r}r} = \begin{bmatrix} s_r & 0 & 0 \\ 0 & 1 & 0 \\ 0 & 0 & 1 \end{bmatrix} \tag{B.17}$$

Selection of a stretch function is a more nuanced question. For this work, several different functions were tested and evaluated by comparison with COMSOL's built in PML for well established simulation results. The final stretch function used was

$$s_r(r') = \begin{cases} 1 & r' < r_{\text{pmli}} \\ (1-i)\left(1 + a_s\left[\frac{r'-r_{\text{pmli}}}{r_{\text{pmlo}}-r_{\text{pmli}}}\right]^m\right) & otherwise \end{cases} \tag{B.18}$$

where r_{pmli} and r_{pmlo} are the inner and outer radii of the PML, a_s is a constant stretch coefficient and m is a constant stretch exponent. A coefficient of $a_s = 1.5$ and an exponent of $m = 2$ was found to produce very similar results to verified data.

References

[1] S. Abbott, "Review of 20 years of undersea optical fiber transmission system development and deployment since TAT-8," in *2008 34th European Conference on Optical Communication*, 2008, pp. 1–4. DOI: 10.1109/ECOC.2008.4729162.

[2] L. Galdino, A. Edwards, W. Yi, E. Sillekens, Y. Wakayama, T. Gerard, W. S. Pelouch, S. Barnes, T. Tsuritani, R. I. Killey, D. Lavery, and P. Bayvel, "Optical Fibre Capacity Optimisation via Continuous Bandwidth Amplification and Geometric Shaping," *IEEE Photonics Technology Letters*, vol. 32, no. 17, pp. 1021–1024, 2020, ISSN: 1941-0174. DOI: 10.1109/LPT.2020.3007591.

[3] K. C. Kao and G. A. Hockham, "Dielectric-fibre surface waveguides for optical frequencies," *Proceedings of the Institution of Electrical Engineers*, vol. 113, no. 7, pp. 1151–1158, 1966, ISSN: 0020-3270 VO - 113. DOI: 10.1049/piee.1966.0189.

[4] F. P. Kapron, D. B. Keck, and R. D. Maurer, "Radiation Losses in Glass Optical Waveguides," *Applied Physics Letters*, vol. 17, no. 10, pp. 423–425, Nov. 1970, ISSN: 0003-6951. DOI: 10.1063/1.1653255.

[5] T. Miya, Y. Terunuma, T. Hosaka, and T. Miyashita, "Ultimate low-loss single-mode fibre at 1.55 micron," *Electronics Letters*, vol. 4, no. 15, pp. 106–108, 1979, ISSN: 0013-5194.

[6] R.-J. Essiambre, G. Kramer, P. J. Winzer, G. J. Foschini, and B. Goebel, "Capacity Limits of Optical Fiber Networks," *Journal of Lightwave Technology*, vol. 28, no. 4, pp. 662–701, 2010.

[7] K. Saito, M. Yamaguchi, H. Kakiuchida, A. J. Ikushima, K. Ohsono, and Y. Kurosawa, "Limit of the Rayleigh scattering loss in silica fiber," *Applied Physics Letters*, vol. 83, no. 25, pp. 5175–5177, Dec. 2003, ISSN: 0003-6951. DOI: 10.1063/1.1635072.

[8] P. J. Winzer, "Modulation and Multiplexing in Optical Communications," in *Conference on Lasers and Electro-Optics/International Quantum Electronics Conference*, ser. OSA Technical Digest (CD), Baltimore, Maryland: Optica Publishing Group, 2009, CTuL3. DOI: 10.1364/CLEO.2009.CTuL3.

[9] D. J. Richardson, "New optical fibres for high-capacity optical communications," *Philosophical Transactions of the Royal Society A: Mathematical, Physical and Engineering Sciences*, vol. 374, no. 2062, p. 20 140 441, 2016, ISSN: 1364-503X.

[10] F. Poletti, "Nested antiresonant nodeless hollow core fiber," *Optics Express*, vol. 22, no. 20, p. 23 807, 2014. DOI: 10.1364/OE.22.023807.

[11] G. T. Jasion, T. Bradley, H. Sakr, J. R. Hayes, Y. Chen, A. Taranta, H. C. Mulvad, I. A. Davidson, N. V. Wheeler, E. N. Fokoua, W. Wang, D. J. Richardson, and F. Poletti, "Recent breakthroughs in hollow core fiber technology," in *Proc.SPIE*, vol. 11309, Jan. 2020. DOI: 10.1117/12.2548585.

[12] P. Poggiolini and F. Poletti, "Opportunities and Challenges for Long-Distance Transmission in Hollow-Core Fibres," in *Optical Fiber Communication Conference (OFC) 2021*, D. K. J. X. C. C. R. C. C. and P. Li M., Eds., ser. OSA Technical Digest, Washington, DC: Optica Publishing Group, 2021, F4C.1. DOI: 10.1364/OFC.2021.F4C.1.

[13] F. Poletti, N. V. Wheeler, M. N. Petrovich, N. Baddela, E. Numkam Fokoua, J. R. Hayes, D. R. Gray, Z. Li, R. Slavík, and D. J. Richardson, "Towards high-capacity fibre-optic communications at the speed of light in vacuum," *Nature Photonics*, vol. 7, p. 279, Mar. 2013.

[14] S. Coen, A. H. L. Chau, R. Leonhardt, J. D. Harvey, J. C. Knight, W. J. Wadsworth, and P. S. J. Russell, "Supercontinuum generation by stimulated Raman scattering and parametric four-wave mixing in photonic crystal fibers," *Journal of the Optical Society of America B*, vol. 19, no. 4, pp. 753–764, 2002. DOI: 10.1364/JOSAB.19.000753.

[15] A. M. Cubillas, S. Unterkofler, T. G. Euser, B. J. M. Etzold, A. C. Jones, P. J. Sadler, P. Wasserscheid, and P. S. J. Russell, "Photonic crystal fibres for chemical sensing and photochemistry," *Chemical Society Reviews*, vol. 42, no. 22, pp. 8629–8648, 2013.

[16] P. Russell, "Photonic Crystal Fibers," *Science*, vol. 299, no. 5605, pp. 358–362, Jan. 2003. DOI: 10.1126/science.1079280.

[17] D. S. Bykov, S. Xie, R. Zeltner, A. Machnev, G. K. L. Wong, T. G. Euser, and P. S. Russell, "Long-range optical trapping and binding of microparticles in hollow-core photonic crystal fibre," *Light: Science & Applications*, vol. 7, no. 1, p. 22, 2018, ISSN: 2047-7538. DOI: 10.1038/s41377-018-0015-z.

[18] E. A. J. Marcatili and R. A. Schmeltzer, "Hollow metallic and dielectric waveguides for long distance optical transmission and lasers," *Bell System Technical Journal*, vol. 43, no. 4, pp. 1783–1809, 1964, ISSN: 0005-8580.

[19] R. F. Cregan, B. J. Mangan, J. C. Knight, T. A. Birks, P. S. J. Russell, P. J. Roberts, and D. C. Allan, "Single-mode photonic band gap guidance of light in air," *science*, vol. 285, no. 5433, pp. 1537–1539, 1999, ISSN: 0036-8075.

[20] B. J. Mangan, L. Farr, A. Langford, P. J. Roberts, D. P. Williams, F. Couny, M. Lawman, M. Mason, S. Coupland, R. Flea, H. Sabert, T. A. Birks, J. C. Knight, and P. S. J. Russell, "Low loss (1.7 dB/km) hollow core photonic bandgap fiber," in *Optical Fiber Communication Conference*, ser. Technical Digest (CD), Los Angeles, California: Optical Society of America, 2004, PD24.

[21] G. T. Jasion, T. D. Bradley, K. Harrington, H. Sakr, Y. Chen, E. N. Fokoua, I. A. Davidson, A. Taranta, J. R. Hayes, D. J. Richardson, and F. Poletti, "Hollow Core NANF with 0.28 dB/km Attenuation in the C and L Bands," in *Optical Fiber Communication Conference Postdeadline Papers 2020*, San Diego, California: Optical Society of America, 2020, Th4B.4. DOI: 10.1364/OFC.2020.Th4B.4.

[22] G. T. Jasion, H. Sakr, J. R. Hayes, S. R. Sandoghchi, L. Hooper, E. N. Fokoua, A. Saljoghei, H. C. Mulvad, M. Alonso, A. Taranta, T. D. Bradley, I. A. Davidson, Y. Chen, D. J. Richardson, and F. Poletti, "0.174 dB/km Hollow Core Double Nested Antiresonant Nodeless Fiber (DNANF)," in *2022 Optical Fiber Communications Conference and Exhibition (OFC)*, 2022, pp. 1–3.

[23] M. Hirano, T. Haruna, Y. Tamura, T. Kawano, S. Ohnuki, Y. Yamamoto, Y. Koyano, and T. Sasaki, "Record low loss, record high FOM optical fiber with manufacturable process," in *2013 Optical Fiber Communication Conference and Exposition and the National Fiber Optic Engineers Conference (OFC/NFOEC)*, 2013, pp. 1–3.

[24] Y. Hong, K. R. H. Bottrill, T. D. Bradley, H. Sakr, G. T. Jasion, K. Harrington, F. Poletti, P. Petropoulos, and D. J. Richardson, "Low-Latency WDM Intensity-Modulation and Direct-Detection Transmission Over ¿100 km Distances in a Hollow Core Fiber," *Laser & Photonics Reviews*, vol. n/a, no. n/a, p. 2 100 102, Aug. 2021, ISSN: 1863-8880. DOI: 10.1002/lpor.202100102.

[25] A. Nespola, S. Straullu, T. D. Bradley, K. Harrington, H. Sakr, G. T. Jasion, E. N. Fokoua, Y. Jung, Y. Chen, J. R. Hayes, F. Forghieri, D. J. Richardson, F. Poletti, G. Bosco, and P. Poggiolini, "Transmission of 61 C-Band Channels Over Record Distance of Hollow-Core-Fiber With L-Band Interferers," *Journal of Lightwave Technology*, vol. 39, no. 3, pp. 813–820, 2021.

[26] H. C. H. Mulvad, S. Abokhamis Mousavi, V. Zuba, L. Xu, H. Sakr, T. D. Bradley, J. R. Hayes, G. T. Jasion, E. Numkam Fokoua, A. Taranta, S.-U. Alam, D. J. Richardson, and F. Poletti, "Kilowatt-average-power single-mode laser light transmission over kilometre-scale hollow-core fibre," *Nature Photonics*, vol. 16, no. 6, pp. 448–453, 2022, ISSN: 1749-4893. DOI: 10.1038/s41566-022-01000-3.

[27] G. T. Jasion, J. S. Shrimpton, Y. Chen, T. Bradley, D. J. Richardson, and F. Poletti, "MicroStructure Element Method (MSEM): viscous flow model for the virtual draw of microstructured optical fibers," *Optics Express*, vol. 23, no. 1, p. 312, 2015, ISSN: 1094-4087. DOI: 10.1364/OE.23.000312.

[28] G. Jackson, T. D. Bradley, G. T. Jasion, and F. Poletti, "Exploring Fabrication Limits for UV Guiding Hollow Core Anti-Resonant Fiber," in *Frontiers in Optics + Laser Science 2021*, M. (.-C. P. T. A. R. and C. Kaindl R., Eds., ser. Technical Digest Series, Washington, DC: Optica Publishing Group, 2021, FW1C.3. DOI: 10.1364/FIO.2021.FW1C.3.

[29] S. Rikimi, Y. Chen, T. W. Kelly, I. A. Davidson, G. T. Jasion, M. Partridge, K. Harrington, T. D. Bradley, A. A. Taranta, F. Poletti, M. N. Petrovich, D. J. Richardson, and N. V. Wheeler, "Internal Gas Composition and Pressure in As-drawn Hollow Core Optical Fibers," *Journal of Lightwave Technology*, vol. 40, no. 14, pp. 4776–4785, 2022.

[30] *Ecoc exhibition industry awards 2022*. [Online]. Available: https://www.ecocexhibition.com/industry-awards/ (visited on 01/31/2022).

[31] W. Belardi, "Design and Properties of Hollow Antiresonant Fibers for the Visible and Near Infrared Spectral Range," *Journal of Lightwave Technology*, vol. 33, no. 21, pp. 4497–4503, 2015. DOI: 10.1109/JLT.2015.2477775.

[32] A. F. Kosolapov, G. K. Alagashev, A. N. Kolyadin, A. D. Pryamikov, A. S. Biryukov, I. Bufetov, and E. M. Dianov, "Hollow-core revolver fibre with a double-capillary reflective cladding," *Quantum Electronics*, vol. 46, no. 3, p. 267, 2016, ISSN: 1063-7818.

[33] J. R. Hayes, S. R. Sandoghchi, T. D. Bradley, Z. Liu, R. Slavík, M. A. Gouveia, N. V. Wheeler, G. Jasion, Y. Chen, E. N. Fokoua, M. N. Petrovich, D. J. Richardson, and F. Poletti, "Antiresonant Hollow Core Fiber With an Octave Spanning Bandwidth for Short Haul Data Communications," *Journal of Lightwave Technology*, vol. 35, no. 3, pp. 437–442, 2017. DOI: 10.1109/JLT.2016.2638205.

[34] S. f. Gao, Y. y. Wang, W. Ding, D. l. Jiang, S. Gu, X. Zhang, and P. Wang, "Hollow-core conjoined-tube negative-curvature fibre with ultralow loss," *Nature Communications*, vol. 9, no. 1, 2018, ISSN: 20411723. DOI: 10.1038/s41467-018-05225-1.

[35] T. D. Bradley, J. R. Hayes, Y. Chen, G. T. Jasion, S. R. Sandoghchi, R. Slavik, E. N. Fokoua, S. Bawn, H. Sakr, I. A. Davidson, A. Taranta, J. P. Thomas, M. N. Petrovich, D. J. Richardson, and F. Poletti, "Record Low-Loss 1.3dB/km Data Transmitting Antiresonant Hollow Core Fibre," in *2018 European Conference on Optical Communication (ECOC)*, 2018, pp. 1–3. DOI: 10.1109/ECOC.2018.8535324.

[36] T. D. Bradley, G. T. Jasion, J. R. Hayes, Y. Chen, L. Hooper, H. Sakr, M. Alonso, A. Taranta, A. Saljoghei, H. Christian, M. Fake, I. A. K. Davidson, N. V. Wheeler, E. N. Fokoua, S. R. Sandoghchi, D. J. Richardson, and F. Poletti, "Antiresonant Hollow Core Fibre with 0 . 65 dB / km Attenuation across the C and L Telecommunication Bands," *European Conference on Optical Communication*, vol. 1, pp. 1–4, 2019.

[37] P. Zhao, H. L. Ho, W. Jin, S. Fan, S. Gao, Y. Wang, and P. Wang, "Gas sensing with mode-phase-difference photothermal spectroscopy assisted by a long period grating in a dual-mode negative-curvature hollow-core optical fiber," *Optics Letters*, vol. 45, no. 20, pp. 5660–5663, 2020. DOI: 10.1364/OL.404323.

[38] M. Michieletto, J. K. Lyngsø, C. Jakobsen, J. Lægsgaard, O. Bang, and T. T. Alkeskjold, "Hollow-core fibers for high power pulse delivery," *Optics Express*, vol. 24, no. 7, pp. 7103–7119, 2016. DOI: 10.1364/OE.24.007103.

[39] F. Benabid, F. Couny, J. C. Knight, T. A. Birks, and P. S. J. Russell, "Compact, stable and efficient all-fibre gas cells using hollow-core photonic crystal fibres," *Nature*, vol. 434, no. 7032, pp. 488–491, 2005, ISSN: 1476-4687. DOI: 10.1038/nature03349.

[40] R. Safaei, G. Fan, O. Kwon, K. Légaré, P. Lassonde, B. E. Schmidt, H. Ibrahim, and F. Légaré, "High-energy multidimensional solitary states in hollow-core fibres," *Nature Photonics*, vol. 14, no. 12, pp. 733–739, 2020, ISSN: 1749-4893. DOI: 10.1038/s41566-020-00699-2.

[41] F. Tani, J. C. Travers, and P. St.J. Russell, "Multimode ultrafast nonlinear optics in optical waveguides: numerical modeling and experiments in kagomé photonic-crystal fiber," *Journal of the Optical Society of America B*, vol. 31, no. 2, p. 311, 2014, ISSN: 0740-3224. DOI: 10.1364/josab.31.000311.

[42] J. Nold, P. Hölzer, N. Y. Joly, G. K. L. Wong, A. Nazarkin, A. Podlipensky, M. Scharrer, and P. S. Russell, "Pressure-controlled phase matching to third harmonic in Ar-filled hollow-core photonic crystal fiber," *Optics Letters*, vol. 35, no. 17, p. 2922, 2010, ISSN: 0146-9592. DOI: 10.1364/ol.35.002922.

[43] J. Yuan, Z. Kang, F. Li, X. Zhang, C. Mei, G. Zhou, X. Sang, Q. Wu, B. Yan, X. Zhou, K. Zhong, K. Wang, C. Yu, G. Farrell, C. Lu, H. Y. Tam, and P. K. A. Wai, "Experimental generation of discrete ultraviolet wavelength by cascaded intermodal four-wave mixing in a multimode photonic crystal fiber," *Optics Letters*, vol. 42, no. 18, p. 3537, 2017, ISSN: 0146-9592. DOI: 10.1364/ol.42.003537.

[44] L. G. Wright, W. H. Renninger, D. N. Christodoulides, and F. W. Wise, "Spatiotemporal dynamics of multimode optical solitons," *Optics Express*, vol. 23, no. 3, pp. 3492–3506, 2015. DOI: 10.1364/OE.23.003492.

[45] L. G. Wright, W. H. Renninger, D. N. Christodoulides, and F. W. Wise, "Nonlinear multimode photonics: nonlinear optics with many degrees of freedom," *Optica*, vol. 9, no. 7, pp. 824–841, 2022. DOI: 10.1364/OPTICA.461981.

[46] W. Jin, H. Bao, P. Zhao, Y. Zhao, Y. Qi, C. Wang, and H. L. Ho, "Recent Advances in Spectroscopic Gas Sensing With Micro/Nano-Structured Optical Fibers," *Photonic Sensors*, vol. 11, no. 2, pp. 141–157, 2021, ISSN: 2190-7439. DOI: 10.1007/s13320-021-0627-4.

[47] P. Zhao, Y. Zhao, H. Bao, H. L. Ho, W. Jin, S. Fan, S. Gao, Y. Wang, and P. Wang, "Mode-phase-difference photothermal spectroscopy for gas detection with an anti-resonant hollow-core optical fiber," *Nature Communications*, vol. 11, no. 1, p. 847, 2020, ISSN: 2041-1723. DOI: 10.1038/s41467-020-14707-0.

[48] M. A. Cooper, S. Wittek, D. Cruz-Delgado, J. Wahlen, J. M. Mercado, J. E. Antonio-Lopez, and R. A. Correa, "Higher order mode generation in an anti-resonant hollow-core fiber," in *Proc.SPIE*, vol. 11724, Apr. 2021. DOI: 10.1117/12.2587936.

[49] B. Winter, T. A. Birks, and W. J. Wadsworth, "Multimode Hollow-Core Anti-Resonant Optical Fibres," in *Frontiers in Optics + Laser Science APS/DLS*, ser. The Optical Society, Washington, DC: Optical Society of America, 2019, JTu4A.18.

[50] Z. Dong, X. Zhang, P. Yao, J. Yao, S. Wan, and P. Wang, "Development of multi-mode rod-type hollow-core antiresonant fiber," in *Proc.SPIE*, vol. 12280, Jul. 2022. DOI: 10.1117/12.2620490.

[51] J. C. Maxwell, "VIII. A dynamical theory of the electromagnetic field," *Philosophical Transactions of the Royal Society of London*, vol. 155, pp. 459–512, Jan. 1865. DOI: 10.1098/rstl.1865.0008.

[52] P. E. Ciddor, "Refractive index of air: new equations for the visible and near infrared," *Applied Optics*, vol. 35, no. 9, pp. 1566–1573, 1996. DOI: 10.1364/AO.35.001566.

[53] Sellmeier, "Zur Erklärung der abnormen Farbenfolge im Spectrum einiger Substanzen," *Annalen der Physik*, vol. 219, no. 6, pp. 272–282, Jan. 1871, ISSN: 0003-3804. DOI: 10.1002/andp.18712190612.

[54] I. H. Malitson, "Interspecimen Comparison of the Refractive Index of Fused Silica," *Journal of the Optical Society of America*, vol. 55, no. 10, pp. 1205–1209, 1965. DOI: 10.1364/JOSA.55.001205.

[55] N. Wong, "Characterisation of hollow-core photonic bandgap fibres and other multimode fibres for optical communications," Ph.D. dissertation, University of Southampton, Jun. 2017.

[56] D. Marcuse, *Theory of dielectric optical waveguides*. Academic Press, Inc., 1974, ISBN: 0323162363.

[57] P. R. McIsaac, "Mode orthogonality in reciprocal and nonreciprocal waveguides," *IEEE Transactions on Microwave Theory and Techniques*, vol. 39, no. 11, pp. 1808–1816, 1991. DOI: 10.1109/22.97481.

[58] J. K. Ranka and R. S. Windeler, "Nonlinear interactions in air-silica microstructure optical fibers," *Optics and Photonics News*, vol. 11, no. 8, pp. 20–25, 2000, ISSN: 1541-3721.

[59] H. Sakr, T. D. Bradley, G. T. Jasion, E. N. Fokoua, S. R. Sandoghchi, I. A. Davidson, A. Taranta, G. Guerra, W. Shere, Y. Chen, J. R. Hayes, D. J. Richardson, and F. Poletti, "Hollow Core NANFs with Five Nested Tubes and Record Low Loss at 850, 1060, 1300 and 1625nm," in *2021 Optical Fiber Communications Conference and Exhibition (OFC)*, 2021, pp. 1–3.

[60] J. C. Knight, T. A. Birks, P. S. J. Russell, and D. M. Atkin, "All-silica single-mode optical fiber with photonic crystal cladding," *Optics Letters*, vol. 21, no. 19, pp. 1547–1549, 1996. DOI: 10.1364/OL.21.001547.

[61] N. V. Wheeler, T. D. Bradley, J. R. Hayes, M. A. Gouveia, S. Liang, Y. Chen, S. R. Sandoghchi, S. M. Abokhamis Mousavi, F. Poletti, M. N. Petrovich, and D. J. Richardson, "Low-loss Kagome hollow-core fibers operating from the near- to the mid-IR," *Optics Letters*, vol. 42, no. 13, p. 2571, 2017, ISSN: 0146-9592. DOI: 10.1364/OL.42.002571.

[62] A. D. Pryamikov, A. S. Biriukov, A. F. Kosolapov, V. G. Plotnichenko, S. L. Semjonov, and E. M. Dianov, "Demonstration of a waveguide regime for a silica hollow - core microstructured optical fiber with a negative curvature of the core boundary in the spectral region > 3.5 μm," *Optics Express*, vol. 19, no. 2, pp. 1441–1448, 2011. DOI: 10.1364/OE.19.001441.

[63] E. Yablonovitch, "Photonic band-gap structures," *Journal of the Optical Society of America B*, vol. 10, no. 2, pp. 283–295, 1993. DOI: 10.1364/JOSAB.10.000283.

[64] J. A. Harrington, "A review of IR transmitting, hollow waveguides," *Fiber & Integrated Optics*, vol. 19, no. 3, pp. 211–227, 2000, ISSN: 0146-8030.

[65] B. Temelkuran, S. D. Hart, G. Benoit, J. D. Joannopoulos, and Y. Fink, "Wavelength-scalable hollow optical fibres with large photonic bandgaps for CO2 laser transmission," *Nature*, vol. 420, no. 6916, pp. 650–653, 2002, ISSN: 1476-4687. DOI: 10.1038/nature01275.

[66] F. Benabid, J. C. Knight, G. Antonopoulos, and P. S. J. Russell, "Stimulated Raman scattering in hydrogen-filled hollow-core photonic crystal fiber," *Science*, vol. 298, no. 5592, pp. 399–402, 2002, ISSN: 0036-8075.

[67] P. S. J. Russell, "Photonic-crystal fibers," *Journal of Lightwave Technology*, vol. 24, no. 12, pp. 4729–4749, 2006, ISSN: 07338724. DOI: 10.1109/JLT.2006.885258.

[68] J. R. Hayes, F. Poletti, M. S. Abokhamis, N. V. Wheeler, N. K. Baddela, and D. J. Richardson, "Anti-resonant hexagram hollow core fibers," *Optics Express*, vol. 23, no. 2, p. 1289, 2015, ISSN: 1094-4087. DOI: 10.1364/OE.23.001289.

[69] F. Yu and J. C. Knight, "Negative Curvature Hollow-Core Optical Fiber," *IEEE Journal of Selected Topics in Quantum Electronics*, vol. 22, no. 2, 2016, ISSN: 21910359. DOI: 10.1109/JSTQE.2015.2473140.

[70] N. M. Litchinitser, A. K. Abeeluck, C. Headley, and B. J. Eggleton, "Antiresonant reflecting photonic crystal optical waveguides," *Optics Letters*, vol. 27, no. 18, p. 1592, 2002, ISSN: 0146-9592. DOI: 10.1364/OL.27.001592.

[71] A. N. Kolyadin, A. F. Kosolapov, A. D. Pryamikov, A. S. Biriukov, V. G. Plotnichenko, and E. M. Dianov, "Light transmission in negative curvature hollow core fiber in extremely high material loss region," *Optics Express*, vol. 21, no. 8, pp. 9514–9519, 2013. DOI: 10.1364/OE.21.009514.

[72] A. Argyros and J. Pla, "Hollow-core polymer fibres with a kagome lattice: potential for transmission in the infrared," *Optics Express*, vol. 15, no. 12, pp. 7713–7719, 2007. DOI: 10.1364/OE.15.007713.

[73] E. N. Fokoua, R. Slavik, D. J. Richardson, and F. Poletti, "Limits of Coupling Efficiency into Hollow-Core Antiresonant Fibers," in *2021 Conference on Lasers and Electro-Optics (CLEO)*, 2021, pp. 1–2.

[74] L. G. Cohen, D. Marcuse, and W. L. Mammel, "Radiating Leaky-Mode Losses in Single-Mode Lightguides with Depressed-Index Claddings," *IEEE Transactions on Microwave Theory and Techniques*, vol. 30, no. 10, pp. 1455–1460, 1982, ISSN: 15579670. DOI: 10.1109/TMTT.1982.1131277.

[75] J. Hu and C. R. Menyuk, "Understanding leaky modes: slab waveguide revisited," *Advances in Optics and Photonics*, vol. 1, no. 1, pp. 58–106, 2009, ISSN: 1943-8206.

[76] B. Debord, F. Amrani, L. Vincetti, F. Gérôme, and F. Benabid, "Hollow-Core Fiber Technology: The Rising of "Gas Photonics"," *Fibers*, vol. 7, no. 2, p. 16, 2019.

[77] P. Uebel, M. C. Günendi, M. H. Frosz, G. Ahmed, N. N. Edavalath, J.-M. Ménard, and P. S. Russell, "Broadband robustly single-mode hollow-core PCF by resonant filtering of higher-order modes," *Optics Letters*, vol. 41, no. 9, pp. 1961–1964, 2016. DOI: 10.1364/OL.41.001961.

[78] V. Michaud-Belleau, E. Numkam Fokoua, T. D. Bradley, J. R. Hayes, Y. Chen, F. Poletti, D. J. Richardson, J. Genest, and R. Slavík, "Backscattering in antiresonant hollow-core fibers: over 40 dB lower than in standard optical fibers," *Optica*, vol. 8, no. 2, pp. 216–219, 2021. DOI: 10.1364/OPTICA.403087.

[79] P. J. Roberts, F. Couny, H. Sabert, B. J. Mangan, D. P. Williams, L. Farr, M. W. Mason, A. Tomlinson, T. A. Birks, and J. C. Knight, "Ultimate low loss of hollow-core photonic crystal fibres," *Optics express*, vol. 13, no. 1, pp. 236–244, 2005, ISSN: 1094-4087.

[80] M. Miyagi, "Bending losses in hollow and dielectric tube leaky waveguides," *Applied Optics*, vol. 20, no. 7, pp. 1221–1229, 1981. DOI: 10.1364/AO.20.001221.

[81] G. C. Balvedi and M. A. R. Franco, "Effect of coupling between fundamental and cladding modes on bending losses in single-polarization single-mode photonic crystal fiber," in *AIP Conference Proceedings*, vol. 1055, 2008, pp. 137–140, ISBN: 9780735405851. DOI: 10.1063/1.3002522.

[82] M. H. Frosz, P. Roth, M. C. Günendi, and P. S. Russell, "Analytical formulation for the bend loss in single-ring hollow-core photonic crystal fibers," *Photonics Research*, vol. 5, no. 2, pp. 88–91, 2017. DOI: 10.1364/PRJ.5.000088.

[83] H. Taylor, "Bending effects in optical fibers," *Journal of Lightwave Technology*, vol. 2, no. 5, pp. 617–628, 1984, ISSN: 1558-2213 VO - 2. DOI: 10.1109/JLT.1984.1073659.

[84] E. N. Fokoua, Y. Chen, D. J. Richardson, and F. Poletti, "Microbending effects in hollow-core photonic bandgap fibers," in *ECOC 2016; 42nd European Conference on Optical Communication*, 2016, pp. 1–3.

[85] G. T. Jasion, D. J. Richardson, and F. Poletti, "Novel Antiresonant Hollow Core Fiber Design with Ultralow Leakage Loss Using Transverse Power Flow Analysis," in *Optical Fiber Communication Conference (OFC) 2019*, ser. OSA Technical Digest, San Diego, California: Optical Society of America, 2019, Th3E.2. DOI: 10.1364/OFC.2019.Th3E.2.

[86] S. Février, B. Beaudou, and P. Viale, "Understanding origin of loss in large pitch hollow-core photonic crystal fibers and their design simplification," *Optics Express*, vol. 18, no. 5, pp. 5142–5150, 2010. DOI: 10.1364/OE.18.005142.

[87] L. Vincetti and V. Setti, "Extra loss due to Fano resonances in inhibited coupling fibers based on a lattice of tubes," *Optics Express*, vol. 20, no. 13, p. 14 350, 2012, ISSN: 1094-4087. DOI: 10.1364/OE.20.014350.

[88] W. Belardi and J. C. Knight, "Hollow antiresonant fibers with reduced attenuation," *Optics Letters*, vol. 39, no. 7, pp. 1853–1856, 2014, ISSN: 0146-9592. DOI: 10.1364/OL.39.001853.

[89] A. Nespola, S. R. Sandoghchi, L. Hooper, M. Alonso, T. D. Bradley, H. Sakr, G. T. Jasion, E. N. Fokoua, S. Straullu, F. Garrisi, G. Bosco, A. Carena, A. M. R. Brusin, Y. Chen, J. R. Hayes, F. Forghieri, D. J. Richardson, F. Poletti, and P. Poggiolini, "Ultra-Long-Haul WDM Transmission in a Reduced Inter-Modal Interference NANF Hollow-Core Fiber," in *Optical Fiber Communication Conference (OFC) 2021*, D. K. J. X. C. C. R. C. C. and P. Li M.,

Eds., ser. OSA Technical Digest, Washington, DC: Optica Publishing Group, 2021, F3B.5. DOI: 10.1364/OFC.2021.F3B.5.

[90] X. Chen, X. Hu, L. Yang, J. Peng, H. Li, N. Dai, and J. Li, "Double negative curvature anti-resonance hollow core fiber," *Optics Express*, vol. 27, no. 14, pp. 19 548–19 554, 2019. DOI: 10.1364/OE.27.019548.

[91] S. Yan, S. Lou, W. Zhang, and Z. Lian, "Single-polarization single-mode double-ring hollow-core anti-resonant fiber," *Optics Express*, vol. 26, no. 24, pp. 31 160–31 171, 2018. DOI: 10.1364/OE.26.031160.

[92] K. S. R. Shaha, A. Khaleque, and I. Hasan, "Low loss double cladding nested hollow core antiresonant fiber," *OSA Continuum*, vol. 3, no. 9, pp. 2512–2524, 2020. DOI: 10.1364/OSAC.402524.

[93] Y. Wang, M. I. Hasan, M. R. A. Hassan, and W. Chang, "Effect of the second ring of antiresonant tubes in negative-curvature fibers," *Optics Express*, vol. 28, no. 2, pp. 1168–1176, 2020. DOI: 10.1364/OE.382516.

[94] F. Amrani, J. H. Osório, F. Delahaye, F. Giovanardi, L. Vincetti, B. Debord, F. Gérôme, and F. Benabid, "Low-loss single-mode hybrid-lattice hollow-core photonic-crystal fibre," *Light: Science & Applications*, vol. 10, no. 1, p. 7, 2021, ISSN: 2047-7538. DOI: 10.1038/s41377-020-00457-7.

[95] D. Bird, "Attenuation of model hollow-core, anti-resonant fibres," *Optics Express*, vol. 25, no. 19, p. 23 215, 2017, ISSN: 1094-4087. DOI: 10.1364/OE.25.023215.

[96] A. W. Snyder and W. R. Young, "Modes of optical waveguides," *Journal of the Optical Society of America*, vol. 68, no. 3, pp. 297–309, 1978. DOI: 10.1364/JOSA.68.000297.

[97] N. A. Issa and L. Poladian, "Vector wave expansion method for leaky modes of microstructured optical fibers," *Journal of Lightwave Technology*, vol. 21, no. 4, pp. 1005–1012, 2003, ISSN: 07338724. DOI: 10.1109/JLT.2003.810091.

[98] J. W. Nicholson, A. D. Yablon, S. Ramachandran, and S. Ghalmi, "Spatially and spectrally resolved imaging of modal content in large-mode-area fibers," *Optics Express*, vol. 16, no. 10, pp. 7233–7243, 2008. DOI: 10.1364/OE.16.007233.

[99] P. R. McIsaac, "Symmetry-Induced Modal Characteristics of Uniform Waveguides," *IEEE Transactions on Microwave Theory and Techniques*, vol. 23, no. 5, pp. 421–429, 1975. DOI: 10.1109/TMTT.1975.1128584.

[100] J. P. Berenger, "A perfectly matched layer for the absorption of electromagnetic waves," *Journal of Computational Physics*, vol. 114, no. 2, pp. 185–200, 1994, ISSN: 10902716. DOI: 10.1006/jcph.1994.1159.

[101] K. Saitoh and M. Koshiba, "Full-vectorial finite element beam propagation method with perfectly matched layers for anisotropic optical waveguides," *Journal of Lightwave Technology*, vol. 19, no. 3, pp. 405–413, 2001, ISSN: 0733-8724 VO - 19. DOI: 10.1109/50.918895.

[102] Y. O. Agha, F. Zolla, A. Nicolet, and S. Guenneau, "On the use of PML for the computation of leaky modes," *Compel*, vol. 27, no. 1, p. 95, 2008, ISSN: 0332-1649.

[103] M. Heiblum and J. Harris, "Analysis of curved optical waveguides by conformal transformation," *IEEE Journal of Quantum Electronics*, vol. 11, no. 2, pp. 75–83, 1975, ISSN: 1558-1713 VO - 11. DOI: 10.1109/JQE.1975.1068563.

[104] P. J. Roberts, F. Couny, H. Sabert, B. J. Mangan, T. A. Birks, J. C. Knight, and P. S. J. Russell, "Loss in solid-core photonic crystal fibers due to interface roughness scattering," *Optics Express*, vol. 13, no. 20, pp. 7779–7793, 2005. DOI: 10.1364/OPEX.13.007779.

[105] E. N. Fokoua, F. Poletti, and D. J. Richardson, "Analysis of light scattering from surface roughness in hollow-core photonic bandgap fibers," *Optics Express*, vol. 20, no. 19, pp. 20 980–20 991, 2012. DOI: 10.1364/OE.20.020980.

[106] E. N. Fokoua, S. R. Sandoghchi, Y. Chen, N. V. Wheeler, N. K. Baddela, J. R. Hayes, M. N. Petrovich, D. J. Richardson, and F. Poletti, "Accurate loss and surface mode modeling in fabricated hollow-core photonic bandgap fibers," in *OFC 2014*, 2014, pp. 1–3. DOI: 10.1364/OFC.2014.M2F.4.

[107] W. Shere, G. T. Jasion, E. Numkam Fokoua, and F. Poletti, "Understanding the impact of cladding modes in multi-mode hollow-core anti-resonant fibres," *Optical Fiber Technology*, vol. 71, p. 102 919, 2022, ISSN: 1068-5200. DOI: 10.1016/j.yofte.2022.102919.

[108] D. C. Allan, N. F. Borrelli, M. T. Gallagher, D. Müller, C. M. Smith, N. Venkataraman, J. A. West, P. Zhang, and K. W. Koch, "Surface modes and loss in air-core photonic bandgap fibers," in *Proc.SPIE*, vol. 5000, Jul. 2003.

[109] J. A. West, C. M. Smith, N. F. Borrelli, D. C. Allan, and K. W. Koch, "Surface modes in air-core photonic band-gap fibers," *Optics Express*, vol. 12, no. 8, pp. 1485–1496, 2004. DOI: 10.1364/OPEX.12.001485.

[110] L. Vincetti, "Empirical formulas for calculating loss in hollow core tube lattice fibers," *Optics Express*, vol. 24, no. 10, pp. 10 313–10 325, 2016. DOI: 10.1364/OE.24.010313.

[111] L. Vincetti and L. Rosa, "A simple analytical model for confinement loss estimation in hollow-core Tube Lattice Fibers," *Optics Express*, vol. 27, no. 4, pp. 5230–5237, 2019. DOI: 10.1364/OE.27.005230.

[112] Y. Y. Wang, N. V. Wheeler, F. Couny, P. J. Roberts, and F. Benabid, "Low loss broadband transmission in hypocycloid-core Kagome hollow-core photonic crystal fiber," *Optics Letters*, vol. 36, no. 5, p. 669, 2011, ISSN: 0146-9592. DOI: 10.1364/OL.36.000669.

[113] F. Poletti, J. R. Hayes, and D. J. Richardson, "Optimising the Performances of Hollow Antiresonant Fibres," in *37th European Conference and Exposition on Optical Communications*, ser. OSA Technical Digest (CD), Geneva: Optical Society of America, 2011, Mo.2.LeCervin.2. DOI: 10.1364/ECOC.2011.Mo.2.LeCervin.2.

[114] F. Yu, W. J. Wadsworth, and J. C. Knight, "Low loss silica hollow core fibers for 3–4 μm spectral region," *Optics Express*, vol. 20, no. 10, pp. 11 153–11 158, 2012. DOI: 10.1364/OE.20.011153.

[115] M. Zeisberger and M. A. Schmidt, "Analytic model for the complex effective index of the leaky modes of tube-type anti-resonant hollow core fibers," *Scientific Reports*, vol. 7, no. 1, p. 11 761, 2017, ISSN: 2045-2322. DOI: 10.1038/s41598-017-12234-5.

[116] A. Deng, I. Hasan, Y. Wang, and W. Chang, "Analyzing mode index mismatch and field overlap for light guidance in negative-curvature fibers," *Optics Express*, vol. 28, no. 19, pp. 27 974–27 988, 2020. DOI: 10.1364/OE.400267.

[117] T. W. Kelly, P. Horak, I. A. Davidson, M. Partridge, G. T. Jasion, S. Rikimi, A. Taranta, D. J. Richardson, F. Poletti, and N. V. Wheeler, "Gas-induced differential refractive index enhanced guidance in hollow-core optical fibers," *Optica*, vol. 8, no. 6, pp. 916–920, 2021. DOI: 10.1364/OPTICA.424224.

[118] *Detail Specification for 850-nm Laser-Optimized, 50-micron Core Diameter/125-micron Cladding Diameter Class Graded-Index Multimode Optical Fibers Suitable for Manufacturing OM4 Cabled Optical Fiber*, TIA-492AAAD, 2009.

[119] W. Shere, G. T. Jasion, E. N. Fokoua, and F. Poletti, "Low Loss, Large Bandwidth Antiresonant Hollow-Core Fiber Design for Short-Reach Links," in *Optical Fiber Communication Conference (OFC) 2020*, ser. OSA Technical Digest, San Diego, California: Optical Society of America, 2020, W4D.3. DOI: 10.1364/OFC.2020.W4D.3.

[120] N. N. Ledentsov, O. Y. Makarov, V. A. Shchukin, V. P. Kalosha, N. Ledentsov, L. Chrochos, M. B. Sanayeh, and J. P. Turkiewicz, "High Speed VCSEL Technology and Applications," *Journal of Lightwave Technology*, vol. 40, no. 6, pp. 1749–1763, 2022, ISSN: 1558-2213. DOI: 10.1109/JLT.2022.3149372.

[121] F. Koyama, "Recent Advances of VCSEL Photonics," *Journal of Lightwave Technology*, vol. 24, no. 12, pp. 4502–4513, 2006.

[122] M. Vervaeke, C. Debaes, B. Volckaerts, and H. Thienpont, "Optomechanical Monte Carlo tolerancing study of a packaged free-space intra-MCM optical interconnect system," *IEEE Journal on Selected Topics in Quantum Electronics*, vol. 12, no. 5, pp. 988–995, 2006, ISSN: 1077260X. DOI: 10.1109/JSTQE.2006.882622.

[123] D. Wiedenmann, R. King, C. Jung, R. Jäger, R. Michalzik, P. Schnitzer, M. Kicherer, and K. J. Ebeling, "Design and analysis of single-mode oxidized VCSEL's for high-speed optical interconnects," *IEEE Journal on Selected Topics in Quantum Electronics*, vol. 5, no. 3, pp. 503–511, 1999, ISSN: 1077260X. DOI: 10.1109/2944.788412.

[124] F. Koyama, S. Kinoshita, and K. Iga, "Room temperature cw operation of GaAs vertical cavity surface emitting laser," *IEICE Transactions (1976-1990)*, vol. 71, no. 11, pp. 1089–1090, 1988.

[125] R. Michalzik, *VCSELs: fundamentals, technology and applications of vertical-cavity surface-emitting lasers*. Springer, 2012, vol. 166, ISBN: 3642249868.

[126] R. Michalzik and K. J. Ebeling, "Generalized BV Diagrams for Higher Order Transverse Modes in Planar Vertical-Cavity Laser Diodes," *IEEE Journal of Quantum Electronics*, vol. 31, no. 8, pp. 1371–1379, 1995.

[127] N. Suzuki, H. Hatakeyama, K. Fukatsu, T. Anan, K. Yashiki, and M. Tsuji, "25-Gbps Operation of 1.1-um-Range InGaAs VCSELs for High-Speed Optical Interconnections," in *Optical Fiber Communication Conference and Exposition and The National Fiber Optic Engineers Conference*, ser. Technical Digest (CD), Anaheim, California: Optical Society of America, 2006, OFA4.

[128] K. H. Hahn, T. M. R., H. Y. M., and W. S. Y., "Large Area Multitransverse-Mode VCSELs for Modal Noise Reduction in Multimode Fibre Systems," *Electronics*, vol. 29, no. 16, pp. 1482–1483, 1993, ISSN: 00135194. DOI: 10.1049/el:19930990.

[129] J. Heinrich, E. Zeeb, and K. J. Ebeling, "Transverse modes under external feedback and fiber coupling efficiencies of VCSEL's," *IEEE Photonics Technology Letters*, vol. 10, no. 10, pp. 1365–1367, 1998, ISSN: 10411135. DOI: 10.1109/68.720262.

[130] X. Yang, G. Zhao, M. Li, X. Liu, Y. Zhang, and D. Deppe, "50% power conversion efficiency on a non-oxide VCSEL," in *2014 Conference on Lasers and Electro-Optics (CLEO) - Laser Science to Photonic Applications*, 2014, pp. 1–2. DOI: 10.1364/CLEO_SI.2014.SF1G.2.

[131] P. Pepeljugoski, D. Kuchta, Y. Kwark, P. Pleunis, and G. Kuyt, "15.6-Gb/s transmission over 1 km of next generation multimode fiber," *IEEE Photonics Technology Letters*, vol. 14, no. 5, pp. 717–719, 2002, ISSN: 1041-1135.

[132] E. N. Fokoua, M. N. Petrovich, T. Bradley, F. Poletti, D. J. Richardson, and R. Slavík, "How to make the propagation time through an optical fiber fully insensitive to temperature variations," *Optica*, vol. 4, no. 6, pp. 659–668, 2017. DOI: 10.1364/OPTICA.4.000659.

[133] X. Zhang, W. Song, Z. Dong, J. Yao, S. Wan, Y. Hou, and P. Wang, "Low loss nested hollow-core anti-resonant fiber at 2 µm spectral range," *Optics Letters*, vol. 47, no. 3, pp. 589–592, 2022. DOI: 10.1364/OL.447418.

[134] R. F. Ando, A. Hartung, B. Jang, and M. A. Schmidt, "Approximate model for analyzing band structures of single-ring hollow-core anti-resonant fibers," *Optics Express*, vol. 27, no. 7, pp. 10 009–10 021, 2019. DOI: 10.1364/OE.27.010009.

[135] A. Ge, F. Meng, Y. Li, B. Liu, and M. Hu, "Higher-Order Mode Suppression in Antiresonant Nodeless Hollow-Core Fibers," *Micromachines*, vol. 10, no. 2, p. 128, Feb. 2019, ISSN: 2072-666X. DOI: 10.3390/mi10020128.

[136] S. A. Mousavi, S. R. Sandoghchi, D. J. Richardson, and F. Poletti, "Broadband high birefringence and polarizing hollow core antiresonant fibers," *Optics Express*, vol. 24, no. 20, pp. 22 943–22 958, 2016. DOI: 10.1364/OE.24.022943.

[137] M. S. Habib, O. Bang, and M. Bache, "Low-loss hollow-core silica fibers with adjacent nested anti-resonant tubes," *Optics Express*, vol. 23, no. 13, pp. 17 394–17 406, 2015. DOI: 10.1364/OE.23.017394.

[138] P. Pepeljugoski, S. E. Golowich, A. J. Ritger, P. Kolesar, and A. Risteski, "Modeling and simulation of next-generation multimode fiber links," *Journal of Lightwave Technology*, vol. 21, no. 5, pp. 1242–1255, 2003, ISSN: 07338724. DOI: 10.1109/JLT.2003.811320.

[139] E. Haglund, A. Haglund, P. Westbergh, J. S. Gustavsson, B. Kogel, and A. Larsson, "25 Gbit/s transmission over 500 m multimode fibre using 850 nm VCSEL with integrated mode filter," *Electronics Letters*, vol. 48, no. 9, pp. 517–519, 2012, ISSN: 0013-5194. DOI: 10.1049/el.2012.0529.

[140] W. Shere, E. N. Fokoua, G. T. Jasion, and F. Poletti, "Designing multi-mode anti-resonant hollow-core fibers for industrial laser power delivery," *Optics Express*, vol. 30, no. 22, pp. 40 425–40 440, 2022. DOI: 10.1364/OE.473681.

[141] X. Xi, "Helically Twisted Solid-Core Photonic Crystal Fibers," Ph.D. dissertation, University of Erlangen-Nuremberg, 2015.

[142] M. C. Günendi, N. N. Edavalath, R. Beravat, G. K. L. Wong, M. H. Frosz, P. Uebel, and P. S. J. Russell, "Twist-tuning of higher-order mode suppression in single-ring hollow-core photonic crystal fibers," in *2016 Conference on Lasers and Electro-Optics (CLEO)*, 2016, pp. 1–2.

[143] P. Roth, Y. Chen, M. C. Günendi, R. Beravat, N. N. Edavalath, M. H. Frosz, G. Ahmed, G. K. L. Wong, and P. S. J. Russell, "Strong circular dichroism for the HE11 mode in twisted single-ring hollow-core photonic crystal fiber," *Optica*, vol. 5, no. 10, pp. 1315–1321, 2018. DOI: 10.1364/OPTICA.5.001315.

[144] P. S. Russell, R. Beravat, and G. K. L. Wong, "Helically twisted photonic crystal fibres," *Philosophical Transactions of the Royal Society A: Mathematical, Physical and Engineering Sciences*, vol. 375, no. 2087, p. 20 150 440, Feb. 2017. DOI: 10.1098/rsta.2015.0440.

[145] A. James Lowery and J. Armstrong, "Orthogonal-frequency-division multiplexing for dispersion compensation of long-haul optical systems," *Optics Express*, vol. 14, no. 6, pp. 2079–2084, 2006. DOI: 10.1364/OE.14.002079.

[146] H.-Y. Kao, C.-T. Tsai, S.-F. Leong, C.-Y. Peng, Y.-C. Chi, J. J. Huang, H.-C. Kuo, T.-T. Shih, J.-J. Jou, W.-H. Cheng, C.-H. Wu, and G.-R. Lin, "Comparison of single-/few-/multi-mode 850 nm VCSELs for optical OFDM transmission," *Optics Express*, vol. 25, no. 14, pp. 16 347–16 363, 2017. DOI: 10.1364/OE.25.016347.

[147] D. J. Richardson, J. Nilsson, and W. A. Clarkson, "High power fiber lasers: current status and future perspectives [Invited]," *Journal of the Optical Society of America B*, vol. 27, no. 11, B63–B92, 2010. DOI: 10.1364/JOSAB.27.000B63.

[148] J. W. Dawson, M. J. Messerly, R. J. Beach, M. Y. Shverdin, E. A. Stappaerts, A. K. Sridharan, P. H. Pax, J. E. Heebner, C. W. Siders, and C. P. J. Barty, "Analysis of the scalability of diffraction-limited fiber lasers and amplifiers to high average power," *Optics Express*, vol. 16, no. 17, pp. 13 240–13 266, 2008. DOI: 10.1364/OE.16.013240.

[149] C. Rohrer, C. A. Codemard, G. Kleem, T. Graf, and M. A. Ahmed, "Preserving Nearly Diffraction-Limited Beam Quality Over Several Hundred Meters of Transmission Through Highly Multimode Fibers," *Journal of Lightwave Technology*, vol. 37, no. 17, pp. 4260–4267, Jun. 2019, ISSN: 0733-8724. DOI: 10.1109/JLT.2019.2922776.

[150] T. Okuda, Y. Fujiya, S. Goya, and A. Inoue, "Beam transmission technology by photonic crystal fiber to realizes high-precision and high-efficiency laser processing technology," *Mitsubishi Heavy Ind. Tech. Rev*, vol. 57, pp. 1–5, 2020.

[151] *IPG Photonics YLS*. [Online]. Available: https://www.ipgphotonics.com/en/products/lasers/high-power-cw-fiber-lasers/1-micron/yls-1-120-kw (visited on 07/04/2022).

[152] S. A. Mousavi, H. C. H. Mulvad, N. V. Wheeler, P. Horak, J. Hayes, Y. Chen, T. D. Bradley, S.-u. Alam, S. R. Sandoghchi, E. N. Fokoua, D. J. Richardson, and F. Poletti, "Nonlinear dynamic of picosecond pulse propagation in atmospheric air-filled hollow core fibers," *Optics Express*, vol. 26, no. 7, pp. 8866–8882, 2018. DOI: 10.1364/OE.26.008866.

[153] L. F. Michaille, D. M. Taylor, C. R. H. Bennett, T. J. Shepherd, C. Jacobsen, and T. P. Hansen, "Damage threshold and bending properties of photonic crystal and photonic band-gap optical fibers," in *Proc.SPIE*, vol. 5618, Nov. 2004. DOI: 10.1117/12.583481.

[154] P. Jaworski, F. Yu, R. R. J. Maier, W. J. Wadsworth, J. C. Knight, J. D. Shephard, and D. P. Hand, "Picosecond and nanosecond pulse delivery through a hollow-core Negative Curvature Fiber for micro-machining applications," *Optics Express*, vol. 21, no. 19, pp. 22 742–22 753, 2013. DOI: 10.1364/OE.21.022742.

[155] S. Eilzer and B. Wedel, *Hollow Core Optical Fibers for Industrial Ultra Short Pulse Laser Beam Delivery Applications*, 2018. DOI: 10.3390/fib6040080.

[156] U. Brauch, C. Röcker, T. Graf, and M. Abdou Ahmed, "High-power, high-brightness solid-state laser architectures and their characteristics," *Applied Physics B: Lasers and Optics*, vol. 128, no. 3, pp. 1–32, 2022, ISSN: 09462171. DOI: 10.1007/s00340-021-07736-0.

[157] V. Kuhn, T. Gottwald, C. Stolzenburg, S.-S. Schad, A. Killi, and T. Ryba, "Latest advances in high brightness disk lasers," *Solid State Lasers XXIV: Technology and Devices*, vol. 9342, pp. 216–222, Feb. 2015. DOI: 10.1117/12.2079876.

[158] S. Nagel, B. Metzger, T. Gottwald, V. Kuhn, A. Killi, and S. S. Schad, "Thin disk laser operating in fundamental mode up to a power of 4kW," *2019 Conference on Lasers and Electro-Optics Europe and European Quantum Electronics Conference, CLEO/Europe-EQEC 2019*, Jun. 2019. DOI: 10.1109/CLEOE-EQEC.2019.8872516.

[159] A. Diebold, C. J. Saraceno, C. R. Phillips, F. Saltarelli, I. J. Graumann, and U. Keller, "Gas-lens effect in kW-class thin-disk lasers," *Optics Express*, vol. 26, no. 10, pp. 12 648–12 659, May 2018. DOI: 10.1364/OE.26.012648.

[160] R. Fleischhaker, R. Gebs, A. Budnicki, M. Wolf, J. Kleinbauer, and D. H. Sutter, "Compact gigawatt-class sub-picosecond Yb:YAG thin-disk regenerative chirped-pulse amplifier with high average power at up to 800 kHz," *2013 Conference on Lasers and Electro-Optics Europe and International Quantum Electronics Conference, CLEO/Europe-IQEC 2013*, 2013. DOI: 10.1109/CLEOE-IQEC.2013.6801054.

[161] D. Sutter, F. Krausz, M. Ueffing, R. Lange, T. Metzger, T. Nubbemeyer, T. Pleyer, V. Pervak, and Z. Major, "Direct regenerative amplification of femtosecond pulses to the multimillijoule level," *Optics Letters, Vol. 41, Issue 16, pp. 3840-3843*, vol. 41, no. 16, pp. 3840–3843, Aug. 2016, ISSN: 1539-4794. DOI: 10.1364/OL.41.003840.

[162] O. H. Heckl, J. Kleinbauer, D. Bauer, S. Weiler, T. Metzger, and D. H. Sutter, "Ultrafast thin-disk lasers," *Springer Series in Optical Sciences*, vol. 195, pp. 93–115, Jan. 2016, ISSN: 15561534.

[163] C. Herkommer, P. Krötz, R. Jung, S. Klingebiel, C. Wandt, R. Bessing, P. Walch, T. Produit, K. Michel, D. Bauer, R. Kienberger, and T. Metzger, "Ultrafast thin-disk multipass amplifier with 720 mJ operating at kilohertz repetition rate for applications in atmospheric research," *Optics Express, Vol. 28, Issue 20, pp. 30164-30173*, vol. 28, no. 20, pp. 30 164–30 173, Sep. 2020, ISSN: 1094-4087. DOI: 10.1364/OE.404185.

[164] A. Loescher, C. Röcker, M. A. Ahmed, and T. Graf, "Azimuthally polarized picosecond vector beam with 1.7 kW of average output power," *Optics Letters, Vol. 46, Issue 14, pp. 3492-3495*, vol. 46, no. 14, pp. 3492–3495, Jul. 2021, ISSN: 1539-4794. DOI: 10.1364/OL.431995.

[165] T. Dietz, M. Jenne, D. Bauer, M. Scharun, D. Sutter, and A. Killi, "Ultrafast thin-disk multi-pass amplifier system providing 1.9 kW of average output power and pulse energies in the 10 mJ range at 1 ps of pulse duration for glass-cleaving applications," *Optics Express, Vol. 28, Issue 8, pp. 11415-11423*, vol. 28, no. 8, pp. 11 415–11 423, Apr. 2020, ISSN: 1094-4087. DOI: 10.1364/OE.383926.

[166] H. D. Hoffmann, J. Weitenberg, P. Russbueldt, R. Poprawe, and T. Mans, "Compact diode-pumped 1.1 kW Yb:YAG Innoslab femtosecond amplifier," *Optics Letters, Vol. 35, Issue 24, pp. 4169-4171*, vol. 35, no. 24, pp. 4169–4171, Dec. 2010, ISSN: 1539-4794. DOI: 10.1364/OL.35.004169.

[167] P. Russbueldt, D. Hoffmann, M. Höfer, J. Löhring, J. Luttmann, A. Meissner, J. Weitenberg, M. Traub, T. Sartorius, D. Esser, R. Wester, P. Loosen, and R. Poprawe, "Innoslab Amplifiers," *IEEE Journal of Selected Topics in Quantum Electronics*, vol. 21, no. 1, pp. 447–463, Jan. 2015, ISSN: 15584542. DOI: 10.1109/JSTQE.2014.2333234.

[168] B. E. Schmidt, A. Hage, T. Mans, F. Legare, and H. J. Worner, "Highly stable, 54mJ Yb-InnoSlab laser platform at 0.5kW average power," *Optics Express, Vol. 25, Issue 15, pp. 17549-17555*, vol. 25, no. 15, pp. 17 549–17 555, Jul. 2017, ISSN: 1094-4087. DOI: 10.1364/OE.25.017549.

[169] *TRUMPF — TruDisk*. [Online]. Available: https://www.trumpf.com/en%7B%5C_%7DINT/products/laser/disk-lasers/trudisk/ (visited on 07/04/2022).

[170] *IPG Photonics YLS-SM*. [Online]. Available: https://www.ipgphotonics.com/en/products/lasers/high-power-cw-fiber-lasers/1-micron/yls-sm-1-10-kw (visited on 07/04/2022).

[171] *TRUMPF — TruPulse*. [Online]. Available: https://www.trumpf.com/en%7B%5C_%7DGB/products/laser/pulsed-lasers/trupulse/ (visited on 07/04/2022).

[172] A. E. Siegman, "Defining, measuring, and optimizing laser beam quality," in *Proc.SPIE*, vol. 1868, Aug. 1993.

[173] V. Zuba, H. C. H. Mulvad, R. Slavík, H. Sakr, F. Poletti, D. J. Richardson, and E. N. Fokoua, "Experimental Investigation into Optimum Laser Coupling Efficiency into Hollow-Core NANFs," in *Conference on Lasers and Electro-Optics*, ser. Technical Digest Series, San Jose, California: Optica Publishing Group, 2022, SW4K.1.

[174] A. E. Siegman, "New developments in laser resonators," in *Proc.SPIE*, vol. 1224, Jun. 1990. DOI: 10.1117/12.18425.

[175] *IPG Photonics YLPN 1-10 mJ, 100-300 W*. [Online]. Available: https://www.ipgphotonics.com/en/products/lasers/nanosecond-fiber-lasers/1-06-micron/ylpn-1-2-mj-100-300-w (visited on 07/07/2022).

[176] *TRUMPF — TruMicro Series 2000*. [Online]. Available: https://www.trumpf.com/en%7B%5C_%7DGB/products/laser/short-and-ultrashort-pulse-lasers/trumicro-series-2000/ (visited on 07/07/2022).

[177] F. Rainer, L. J. Atherton, J. H. Campbell, F. P. D. Marco, M. R. Kozlowski, A. J. Morgan, and M. C. Staggs, "Four-harmonic database of laser-damage testing," in *Proc.SPIE*, vol. 1624, Jul. 1992. DOI: 10.1117/12.60128.

[178] M. S. Zediker, "High power fiber lasers in geothermal, oil and gas," in *Proc.SPIE*, vol. 8961, Mar. 2014. DOI: 10.1117/12.2042339.

[179] P. A. Hilton and A. Khan, "Underwater cutting using a 1 μm laser source," *Journal of Laser Applications*, vol. 27, no. 3, p. 032 013, Jun. 2015, ISSN: 1042-346X. DOI: 10.2351/1.4922384.

[180] J. Hodgkinson and R. P. Tatam, "Optical gas sensing: a review," *Measurement Science and Technology*, vol. 24, no. 1, p. 012 004, 2012, ISSN: 0957-0233. DOI: 10.1088/0957-0233/24/1/012004.

[181] D. Pagnoux, S. Fevrier, P. Leproux, M. C. P. Huy, A. Pryamikov, P. Viale, V. Tombelaine, V. Couderc, P. Roy, J. L. Auguste, J.-M. Blondy, G. Laffont, V. Dewinter-Marty, P. Ferdinand, B. Dussardier, and W. Blanc, "Microstructured fibers for sensing applications," in *Proc.SPIE*, vol. 5855, May 2005. DOI: 10.1117/12.623251.

[182] X.-l. Liu, W. Ding, Y.-y. Wang, S.-f. Gao, L. Cao, X. Feng, and P. Wang, "Characterization of a liquid-filled nodeless anti-resonant fiber for biochemical sensing," *Optics Letters*, vol. 42, no. 4, pp. 863–866, 2017. DOI: 10.1364/OL.42.000863.

[183] C. Yao, Q. Wang, Y. Lin, W. Jin, L. Xiao, S. Gao, Y. Wang, P. Wang, and W. Ren, "Photothermal CO detection in a hollow-core negative curvature fiber," *Optics Letters*, vol. 44, no. 16, pp. 4048–4051, 2019. DOI: 10.1364/OL.44.004048.

[184] N. V. Wheeler, M. G. Pappa, T. D. Bradley, Y. Chen, W. Brooks, J. Storey, M. Foster, D. J. Richardson, and M. N. Petrovich, "Spontaneous Raman scattering in hollow core photonic crystal fibres," in *2017 IEEE SENSORS*, 2017, pp. 1–3. DOI: 10.1109/ICSENS.2017.8233880.

[185] M. A. Farahani and T. Gogolla, "Spontaneous Raman Scattering in Optical Fibers with Modulated Probe Light for Distributed Temperature Raman Remote Sensing," *Journal of Lightwave Technology*, vol. 17, no. 8, p. 1379, 1999.

[186] M. P. Buric, K. P. Chen, J. Falk, and S. D. Woodruff, "Improved sensitivity gas detection by spontaneous Raman scattering," *Applied Optics*, vol. 48, no. 22, pp. 4424–4429, 2009. DOI: 10.1364/AO.48.004424.

[187] S. Hanf, R. Keiner, D. Yan, J. Popp, and T. Frosch, "Fiber-Enhanced Raman Multigas Spectroscopy: A Versatile Tool for Environmental Gas Sensing and Breath Analysis," *Analytical Chemistry*, vol. 86, no. 11, pp. 5278–5285, Jun. 2014, ISSN: 0003-2700. DOI: 10.1021/ac404162w.

[188] Y. L. Hoo, W. Jin, C. Shi, H. L. Ho, D. N. Wang, and S. C. Ruan, "Design and modeling of a photonic crystal fiber gas sensor," *Applied Optics*, vol. 42, no. 18, pp. 3509–3515, 2003. DOI: 10.1364/AO.42.003509.

[189] E. Numkam Fokoua, V. Michaud-Belleau, J. Genest, R. Slavík, and F. Poletti, "Theoretical analysis of backscattering in hollow-core antiresonant fibers," *APL Photonics*, vol. 6, no. 9, p. 96 106, Sep. 2021. DOI: 10.1063/5.0057999.

[190] G. W. Milton, M. Briane, and J. R. Willis, "On cloaking for elasticity and physical equations with a transformation invariant form," *New Journal of Physics*, vol. 8, no. 10, p. 248, 2006, ISSN: 1367-2630.

[191] A. Nicolet, F. Zolla, Y. O. Agha, and S. Guenneau, "Geometrical transformations and equivalent materials in computational electromagnetism," *COMPEL - The International Journal for Computation and Mathematics in Electrical and Electronic Engineering*, vol. 27, no. 4, pp. 806–819, 2008, ISSN: 03321649. DOI: 10.1108/03321640810878216.

[192] W. Shere, G. T. Jasion, E. N. Fokoua, and F. Poletti, "Design Rules for Multi-Mode Anti-Resonant Hollow-Core Fibres," in *2021 Optical Fiber Communications Conference and Exhibition (OFC)*, 2021, pp. 1–3.

List of Publications

W. Shere, G. T. Jasion, E. N. Fokoua, and F. Poletti, "Low Loss, Large Bandwidth Antiresonant Hollow-Core Fiber Design for Short-Reach Links," in *Optical Fiber Communication Conference (OFC) 2020*, ser. OSA Technical Digest, San Diego, California: Optical Society of America, 2020, W4D.3. DOI: 10.1364/OFC.2020.W4D.3

W. Shere, G. T. Jasion, E. N. Fokoua, and F. Poletti, "Design Rules for Multi-Mode Anti-Resonant Hollow-Core Fibres," in *2021 Optical Fiber Communications Conference and Exhibition (OFC)*, 2021, pp. 1–3

W. Shere, G. T. Jasion, E. Numkam Fokoua, and F. Poletti, "Understanding the impact of cladding modes in multi-mode hollow-core anti-resonant fibres," *Optical Fiber Technology*, vol. 71, p. 102 919, 2022, ISSN: 1068-5200. DOI: 10.1016/j.yofte.2022.102919

W. Shere, E. N. Fokoua, G. T. Jasion, and F. Poletti, "Designing multi-mode anti-resonant hollow-core fibers for industrial laser power delivery," *Optics Express*, vol. 30, no. 22, pp. 40 425–40 440, 2022. DOI: 10.1364/OE.473681

H. Sakr, T. D. Bradley, G. T. Jasion, E. N. Fokoua, S. R. Sandoghchi, I. A. Davidson, A. Taranta, G. Guerra, W. Shere, Y. Chen, J. R. Hayes, D. J. Richardson, and F. Poletti, "Hollow Core NANFs with Five Nested Tubes and Record Low Loss at 850, 1060, 1300 and 1625nm," in *2021 Optical Fiber Communications Conference and Exhibition (OFC)*, 2021, pp. 1–3